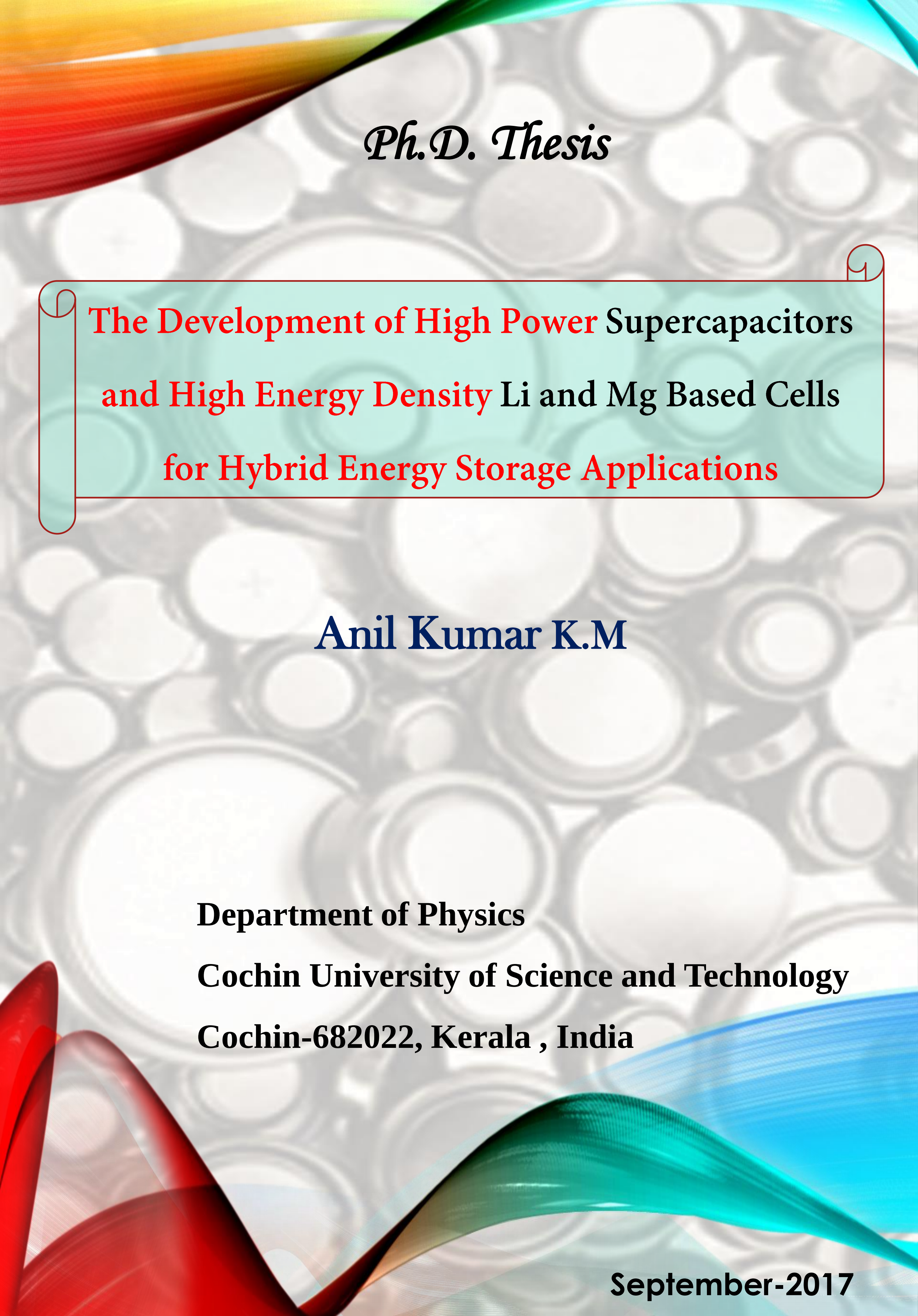

Ph.D. Thesis

The Development of High Power Supercapacitors and High Energy Density Li and Mg Based Cells for Hybrid Energy Storage Applications

Anil Kumar K.M

Department of Physics
Cochin University of Science and Technology
Cochin-682022, Kerala , India

September-2017

The Development of High Power Supercapacitors and High Energy Density Li and Mg Based Cells for Hybrid Energy Storage Applications

Thesis submitted to
Cochin University of Science and Technology
in partial fulfillment of the requirements
for the award of the degree of

DOCTOR OF PHILOSOPHY

By

ANIL KUMAR .K.M

DEPARTMENT OF PHYSICS
COCHIN UNIVERSITY OF SCIENCE AND TECHNOLOGY
COCHIN -682022
September 2017

The Development of High Power Supercapacitors and High Energy Density Li and Mg Based Cells for Hybrid Energy Storage Applications

Ph.D. thesis in the field of Material Science

Author:
Anil Kumar .K. M
Division for Research in Advanced Materials
Department of Physics
Cochin University of Science and Technology
Kochi-682022, Kerala, India
Email: anilkochi@gmail.com

Supervisor:
Dr. S. Jayalekshmi
Professor (Retd),
Division for Research in Advanced Materials
Department of Physics
Cochin University of Science and Technology
Kochi-682022, Kerala, India
Email: jayalekshmi@cusat.ac.in

September 2017

Department of Physics
Cochin University of Science and Technology
Cochin -682022

Dr. S. Jayalekshmi
Professor

Certificate

Certified that the work presented in this thesis entitled " **The Development of High Power Supercapacitors and High Energy Density Li and Mg Based Cells for Energy Storage Applications** " is based on the authentic record of research carried out by Mr Anil Kumar K M, under my guidance at the Department of Physics , Cochin University of Science and Technology and has not been included in any other thesis submitted by the audience during the pre-synopsis seminar and recommendations by doctoral committee of the candidate have been incorporated in the thesis.

Prof. S. Jayalekshmi
(Supervising Guide)

Cochin -22
12-07-2017

Declaration

I hereby declare that the present work entitled "**The Development of High Power Supercapacitors and High Energy Density Li and Mg Based Cells for Hybrid Energy Storage Applications"** is based on the original work done by me under the guidance of Dr. S. Jayalekshmi , Professor (Retd) , Department of Physics , Cochin University of Science and Technology , and has not been included in any other thesis submitted previously for the award of any other degree.

Anil Kumar .K.M

Kochi-22
14/09/2017

Dedicated

To

My Beloved
Teachers

“The single greatest cause of happiness is *gratitude*.”

— Auliq-Ice

It is more a pleasure than merely the observance of a custom to acknowledge the help and assistance I have received from the following persons at various stages of my research. I am deeply indebted to my supervising teacher Dr. S Jayalekshmi, formerly Professor and Head of the Department of Physics, Cochin University of Science and Technology, Kochi, for her excellent and inspiring guidance. She has combined motivation and control, and affection and sternness in the right measure to keep my research on proper course and steer it to its destination.

I am extremely thankful to Prof. Junaid Bushiri , Head of the Department of Physics , CUSAT and the former Heads of the Department for providing the necessary facilities for carrying out the research work. I have been privileged throughout the period of my research work to have the advice and help of Dr M.K Jayaraj, Professor, Department of Physics CUSAT. I express my deep sense of gratitude to him for the timely help and support extended, all through my research career. I also had the opportunity to interact with Dr B Pradeep, Dr M R Anantharaman , Dr.C Sudha Kartha and Dr K P Vijayakumar, former professors of the Department of Physics, CUSAT during the years of my research work. I take this opportunity to thank them all for the timely assistance extended to me.

I express my sincere thanks to the administrative and library staff of the Department of Physics, CUSAT, for their constant encouragement and help during my tenure as a research scholar in the Department. The Teacher Fellowship under the FDP, provided by the University Grants Commission has been quite useful for the satisfactory completion of the research work. I sincerely thank the University Grants Commission authorities for granting me the fellowship under the FDP.

I express my sincere thanks to Dr C Gouri and Dr. Bibin John, LFCD Division, VSSC Thiruvanthapuram for providing hands on training on the assembling of the electrochemical cells and for extending all the support for the satisfactory completion of the research project on Li ion cells. The affection, consideration and the co-operation shown by the staff of the Department of Physics, especially Mrs. Jyothi.G and the office staff of the M.S.M College, Kayamkulam are gratefully acknowledged.

I express my deep sense of gratitude to Dr V S Pradeep, DST-INSPIRE faculty, Department of Physics, CUSAT and Dr Sreekanth J Varma, Assistant Professor, SD College, Alapuzha, who have helped me in many ways, sometimes making available to me the most useful informations, at times suggesting the right idea or hinting the things that eluded my memory, and always ready to engage themselves in discussions that were immensely helpful in fine-tuning my arguments. My heart swells with gratitude when I remember the help and assistance I received from them.

I am thankful to Dr. Govind R, Assistant Professor, Department of English, M.S.M College, Kayamkulam, for the help in the thesis writing.

I am extremely grateful to my most beloved teachers, Late, Dr K Raveendranath, former Head, Department of Physics, Aqunias College, Edakochi and Professor S. Rajendran, former Head of the Department of Physics, The Cochin College, Kochi and all the other teachers for instilling in me the spirit of academic pursuit and for giving me invaluable moral and material support throughout my academic carrier.

I express my sincere gratitude to Mr. Manoj M , Mr Abhilash A , Mr Joseph John , Mrs Jinisha B , Mrs Sabira K , Mrs Saheeda , Dr Anand P.B , Renjini R Mohan and other alumni from the Division for Research in Advanced Materials (DREAM lab) laboratory of the Department of Physics, CUSAT for their help, love and support.

I take this opportunity to express my gratitude to all my friends and well-wishers from CUSAT and MSM College who have stood by me and showered their affection and support all through my research career.

Words are inadequate to express my indebtedness to my beloved parents and my father and mother in laws, for their support, affection and blessings all through my academic and research career. The patience, care and the affection of my wife Nikhila and the ever freshening ambience of the presence of my sons have served as the energy resource for my strides through the hectic days of academic and research activities .I do not know how to express my *appreciation for everything they have done for me and continue to do, in the most affectionate way.*

I thank God, the Almighty, for sustaining me in this endeavour and showering all the blessings for the fulfilment of my dreams.

Anil Kumar K M

Preface

As the world is the marching through the 21st century, the energy demands of humanity shall no longer be sufficiently satisfied by conventional fuels. Along with energy generation, the efficient storage of the harvested energy is also mandatory and this area is challengingly capturing the visionary power of energy researchers. Conventional energy technologies based on fossil fuels and hydroelectric and nuclear resources are subjected to the twin problems of exhaustiveness and environmental degradation. Presently available renewable technologies of energy harvesting, based on the photo-voltaic panels and the wind turbines, enable the generation of pollution free and clean energy. However, the discontinuous nature of energy generation prevents them from becoming primary energy reapers. The emerging energy storage technologies can offset the intermittency problems of renewable energy sources by storing the generated energy and making it accessible upon demand.

The electrochemical power sources, devoid of the deficits of both the conventional and the non-conventional energy technologies, have assumed the central stage of modern research in the energy scenario. They mainly consist of rechargeable cells, fuel cells and super capacitors and have already possessed a considerable level of sophistication in their design strategies.

The efficiency of any energy delivery system is fundamentally dependent on its energy density and the power density. One of the operational draw backs in the currently available electrochemical energy systems is that the energy density and the power density are inversely proportional. In order to optimize the performance of the electrochemical energy storage systems there has to be a greater harmony between these two parameters. The electrochemical cell has high energy density and low power density while it is vice versa in a supercapacitor. The thesis entitled "**The Development of High Power Supercapacitors and High Energy Density Li And Mg Based Cells for Hybrid Energy Storage Applications"** is a comprehensive report of the experiments conducted on the lithium and magnesium based cells and the carbon and the transition metal oxides based super capacitors in order to attain higher harmony between the energy density and the power density.

The thesis begins with an "Introduction" to the basics of the electrochemical energy storage systems and evolves into providing a complete view of the specific types of systems investigated in the present work. The second chapter titled as the "Relevant experimental techniques" is intended to provide an overview of the various experimental techniques employed for the analysis and the characterization of the synthesized materials and the assembled devices.

The chapters three to seven are highlighted as the core chapters, as they dwell upon the studies conducted for identifying the most suitable electrode and the electrolyte materials for the energy storage systems based on the Li and Mg ion cells and high power supercapacitors The third chapter deals with the studies on the impact of using the "acid washed, steam activated carbon" instead of merely the steam activated carbon on improving the energy-power ratio of the carbon based supercapacitors. The study provides authentic results regarding the electrochemical and the structural properties of the carbon based electrical double layer (EDL) supercapacitors.

The fourth chapter portrays a comprehensive account of the structural and the electrochemical studies conducted on the nanocomposite material comprising of Mn_3O_4 nanorods and the reduced graphene oxide (rGO), used in hybrid supercapacitors. In the novel approach used for growing the Mn_3O_4/rGO nanocomposite, the two component materials are separately synthesized and physically mixed in order to attain greater control over the ratio of composition of the two nanostructured materials.

The studies conducted to enhance the specific capacity and the efficiency of the lithium sulfur (Li-S) cells, by rectifying two of the proven deficiencies of very low electrical conductivity of the sulfur cathode which affects the energy density and the formation of polysulfides which impairs the cycle life of the cells, form the focal theme of the fifth chapter. The investigations involve the structural alteration of the sulfur electrode by coating it with a thin layer of the highly conducting polymer, PEDOT-PSS using the hydrothermal method, to rectify the limitations of the sulfur cathode.

Chapter six gives a detailed description of the identification of the highly prospective solid polymer electrolyte (SPE), based on the polymer blend of polyethylene oxide (PEO) and polyvinyl pyrrolidone (PVP), complexed with the Mg salt, $Mg(NO_3)_2$,suitable for designing the all solid state Mg ion cells. The SPE membranes obtained using the simple solution casting technique are found to have quite impressive electrochemical properties, anticipated for high quality solid electrolytes.

The practical realization of the lithium ion full cells using the olivine type and nanostructured $LiFePO_4$ as the cathode and the HF washed, steam activated, coconut shell derived carbon as the anode, comprises the prime theme of chapter seven. The impact of the structural alteration of the anode by substituting the conventionally used graphite with the acid washed, steam activated carbon, and of the conventional $LiFePO_4$ cathode material by coating it with carbon, to make it nanostructured, has been studied. The rate capability of the assembled Li ion full cells is found to increase, compared to that of the conventional full cells, without compromising the environment friendly features of the electrode materials used.

The concluding chapter provides a reassessment of the experiments conducted, the results obtained and the inferences drawn, both in letters and in spirit. The relevance of the present investigations and the scope for further research in the field of the energy storage devices, based on the conclusions arrived at from the present studies, have been assessed from the perspectives of the materials used and the procedures adopted.

Journal Papers

1. **Anilkumar K. M**, Manoj. M, Jinisha. B, Pradeep V S, S. Jayalekshmi, Mn_3O_4/reduced graphene oxide nanocomposite electrodes with tailored morphology for high power supercapacitor applications, Electrochim. Acta. 236 (2017) 424–433. doi:10.1016/j.electacta.2017.03.167.
2. **Anilkumar K. M** , B. Jinisha, M. Manoj, S. Jayalekshmi, Poly(ethylene oxide) (PEO) - Poly(vinyl pyrrolidone) (PVP) blend polymer based solid electrolyte membranes for developing solid state magnesium ion cells, Eur. Polym. J. (2017). doi:10.1016/j.eurpolymj.2017.02.004.
3. **Anilkumar K.M**, B. Jinisha, M. Manoj, V.S. Pradeep, S. Jayalekshmi, Layered sulfur/PEDOT:PSS nano composite electrodes for lithium sulfur cell applications, Appl. Surf. Sci. 442 (2018) 556–564. doi:10.1016/j.apsusc.2018.02.178.
4. **Anilkumar K.M.**, C.M. Ashraf, B. Jinisha, M. Manoj, V.S. Pradeep, S. Jayalekshmi, Acid Washed, Steam Activated, Coconut Shell Derived Carbon for High Power Supercapacitor Applications, J. Electrochem. Soc. 165 (2018) A900–A909. doi:10.1149/2.0491805jes.
5. Jinisha. B, **Anilkumar K. M**, Manoj . M, Pradeep V.S, S. jayalekshmi , Development of a novel type of solid polymer electrolyte for solid state lithium battery applications based on lithium enriched poly (ethylene oxide) (PEO)/poly (vinyl pyrrolidone) (PVP) blend polymer, Electrochim. Acta. 235 (2017) 210–222. doi:10.1016/j.electacta.2017.03.118.

6. M. Manoj, **Anilkumar .K.M**, B. Jinisha, S. Jayalekshmi, Polyaniline–Graphene Oxide based ordered nanocomposite electrodes for high-performance supercapacitor applications, J. Mater. Sci. Mater. Electron. 0 (2017) 1–8. doi:10.1007/s10854-017-7292-9.
7. B. Jinisha, **Anilkumar .K.M**, M. Manoj, A. Abhilash, V.S. Pradeep, S. Jayalekshmi, Poly (ethylene oxide) (PEO)-based, sodium ion-conducting, solid polymer electrolyte films, dispersed with Al2O3 filler, for applications in sodium ion cells, Ionics (Kiel). (2017). doi:10.1007/s11581-017-2332-2.
8. J. John, M. Manoj, **Anilkumar .K.M**, V.S. Pradeep, S. Jayalekshmi, Lithium-enriched polypyrrole as a prospective cathode material for Li-ion cells, Ionics (Kiel). (2018) 1–10. doi:10.1007/s11581-017-2398-x.
9. P.B. Anand, K. Hasna, **Anilkumar K. M**, S. Jayalekshmi, On the structural and optical properties of gold–polyaniline nanocomposite synthesized via a novel route, (n.d.). doi:10.1002/pi.4262.
10. A.M. Sajimol, P.B. Anand, **Anilkumar K. M**, S. Jayalekshmi, Exceptionally good, transparent and flexible FeS2/poly(vinyl pyrrolidone) and FeS2/poly(vinyl alcohol) nanocomposite thin films with excellent UV-shielding properties, Polym. Int. 2013). doi:10.1002/pi.4348.
11. V. Sreevalsa, P. Jeeju, M. Sajimol Augustine, **Anilkumar K. M**, S. Jayalekshmi, L-Histidine-modified biocompatible zinc oxide nanocrystals, J. Exp. Nanosci. 8 (2013) 7–8. doi:10.1080/17458080.2011.624553.

12. M. Rajive Tomy, **Anilkumar K. M**, P.B.B. Anand, S. Jayalekshmi, Effect of annealing on structural and electrical properties of the Li–Mn–O thin films, prepared by high frequency RF magnetron sputtering, J. Phys. Chem. Solids. 72 (2011) 1251–1255. doi:10.1016/j.jpcs.2011.07.018.
13. M. Rajive Tomy, , **Anilkumar K. M**, P.B. Anand, S. Jayalekshmi, Effect of annealing on the electrochemical properties of the Li-Mn-O thin films, prepared by high frequency RF magnetron sputtering Journal of Physics and Chemistry of Solids,Volume 73, Issue 4, April 2012, Pages 559-563
14. Rajive Tomy M, **Anil Kumar K M** and S Jayalekshmi, A Cost effective, fully automated electrochemical Characterization setup for thin film LI-ion battery research, Journal of Instrument Society of India, Vol 41, No. 2, June 2011

Conference proceedings

1. A novel method for realizing high capacity $LiFePO_4$ -based Lithium-ion cells

   Anil Kumar K.M, Rajive Tomy, Bibin John, Priya Carol, Jayalekshmi S, Gouri C, Prathapachandra KurupM.R (ISRS 2010 at IIT Chennai on Dec 20-22 2010)
2. "Fully automated charge –discharge cycling anf cyclic voltametry measurements setup using Keithley 2400 and LabVIEW for Lithium-ion battery research ", Rajive Tomy, **Anil Kumar. K.M**, S. Jayalekshmi, VI-Manthra 2009 held on 06 November 9, 2009 at Chennai (**Placed among top five papers**)
3. "Electronic bandstructure of Olivine Lithium Nickel Phosphate from reflectance spectrum and its miodification upon multiwalled carbon nanotube addition, K.Ravindranath, **Anil Kumar. K.M**, Rajive Tomy, S. Jayalekshmi, Proc. Cochin Nano 2009, held at Cochin during 3rd to 7th of January 2009.
4. "Flexible Solid Electrolyte Sheets for Lithium ion cells" **Anil Kumar K M**, Jinisha B,, Manoj M , S Jayalekshmi at the international conference on energy harvesting storage and conversion (ICEEE-2015) Conducted by Department of Physics , Cochin Univesristty of Science & Technology(CUSAT). Kochi

5. “Will Mg-ion cells serve as substitute for Li-ion cells?” **Anil Kumar K M**, Jinisha B,, Manoj M , S Jayalekshmi at the international conference on Contemporary Advances of Science & Technoligy (IC-CAST 2015) Conducted by Department of Physics , Banaras Hindu University,Varanasi ,India
6. “MWNT/GO/rGO/Graphene- Ni-doped Mn_3O_4 Composite Electrode material for Supercapacitors applications” **Anil Kumar K M**, Jinisha B,, Manoj M , S Jayalekshmi at the National conference on Carbon Materials (NCCM 2015) Conducted by NPL , New Delhi ,India
7. Lithium enriched solid polymer blend electrolytes based on poly (vinyl pyrrolidone) for energy storage application, Jinisha B, **Anil Kumar K M**, Manoj M , S Jayalekshmi, National Conference on Carbon Materials, *NCCM 2015*,IIC, New Delhi, India.
8. Lithium enriched solid polymer blend electrolytes based on poly (vinyl pyrrolidone) using different lithium salts for energy storage applications, Jinisha B, **Anil Kumar K M**, Manoj M , S Jayalekshmi, International Conference on Materials for the Millennium (*MATCON 2016*) Dept. of Applied Chemistry, Cochin University of Science and Technology, Cochin 22, Kerala.
9. Studies on a prospective polymer blend electrolyte material for developing pollution free, solid state Li-ion cells, *28th Kerala Science Congress*, Jinisha B, **Anil Kumar K M**, S Jayalekshmi Calicut University Campus, Thenhippalam, Malappuram. **(Best poster award)**

10. Polyethylene oxide (PEO) / polyvinyl alcohol (PVA) complexed with lithium perchlorate ($LiClO_4$) as a prospective material for making solid polymer electrolyte films, Jinisha B, **Anil Kumar K M,** Manoj M , S Jayalekshmi International Conference on Smart Engineering Materials ICSEM-2016, RV college of Engineering, Bangalore.
11. On the prospects of developing high voltage lithium ion cells using solid polymer electrolyte films, Jinisha B, **Anil Kumar K M**, Manoj M , S Jayalekshmi, International Conference on Advanced Materials (SCICON-2016) 19-21 December, Amritha University, Coimbatore.
12. Fe_2O_3/Graphene oxide based anode materials with solid polymer electrolytes for Li-ion storage applications, Jinisha B, V.S. Pradeep, **Anilkumar K M**, Manoj M, S. Jayalekshmi International Conference on Advances in Functional Materials(IC-AFM) January 6-8, 2017, Anna University, Chennai.

CONTENTS

Chapter 1: Introduction

Chapter 2: Relevant Experimental Techniques

Chapter 3: Acid Washed, Steam Activated, Coconut Shell Derived Carbon for High Power Supercapacitor Applications

Chapter 4: Manganese Oxide/Reduced Graphene Oxide Nanocomposite Electrodes with Tailored Morphology for High Power Supercapacitor Applications

Chapter 5: Realizing Lithium Sulfur Cells Using Layered, Sulfur / Polymer Nano Composite Electrodes

Chapter 6: Poly(Ethylene Oxide) (PEO) - Poly(Vinyl Pyrrolidone) (PVP) Blend Polymer Based Solid Electrolyte Membranes for Developing Solid State Magnesium Ion Cells

Chapter 7: Realizing Li Ion Full Cells Using $LiFePO_4$ and Activated Carbon as Electrodes

Chapter 8: Summary and Scope for Further Studies

CHAPTER 1

Introduction

Abstract:

The work presented in the thesis can be pictured as the incessant exploration in search of the materials and the design strategies to accomplish the practical realization of the energy storage systems, based on rechargeable cells and high power supercapacitors. The first chapter of the thesis, titled as the "Introduction" starts with the recent concerns regarding the need for developing pollution free and renewable types of energy harvesting and the associated energy storage systems and evolves into the detailed anatomy of the electrochemical energy storage systems, investigated in the present work.. The objectives of the present investigations and the motivation behind the work are also highlighted as the integral parts of this chapter.

1.1 Introduction

The efforts towards the development of efficient, sustainable and pollution free energy resources have intensified during the past decades to meet the fast growing global demands of maintaining an ever increasing world population [1,2]. A schematic representation of the present energy utilization is shown in figure 1.

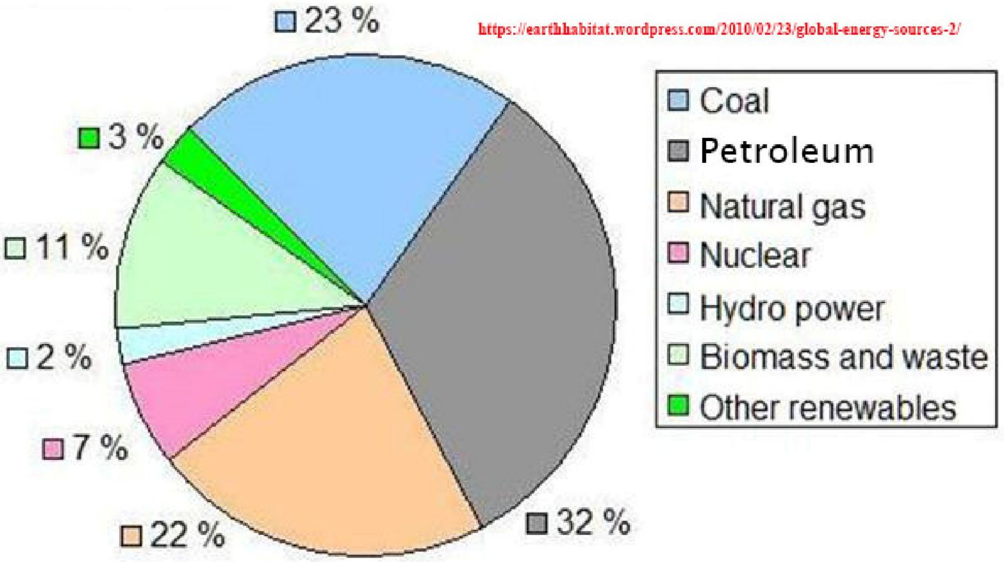

https://earthhabitat.wordpress.com/2010/02/23/global-energy-sources-2/

Figure 1: ***Schematic representation of fuel utilization***

The excessive dependence on fossil fuel combustion, which is the conventional means of power generation, is clearly illustrated in the given figure 2. The extreme use of the fossil fuel combustion has resulted in a two-fold catastrophe. The first is the faster-than-normal rate of depletion of the reserves of this cheap but non-renewable source of energy in the isolated pockets of its saturation, and the second is the looming danger of the global warming and the associated environmental hazards related to the ozone depletion, variations in climatic patterns and the emission of greenhouse gases, especially carbon dioxide, as a byproduct of the fossil fuel combustion [3].

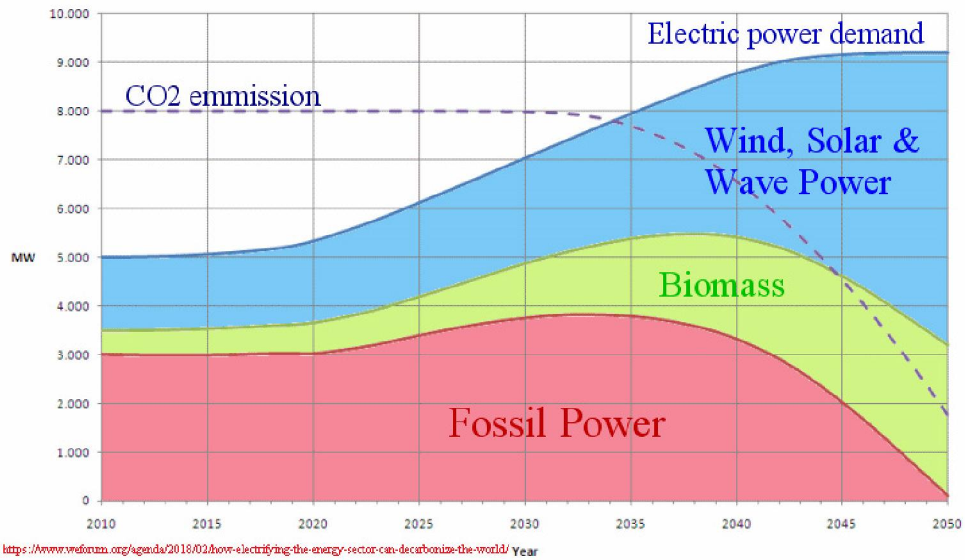

https://www.weforum.org/agenda/2018/02/how-electrifying-the-energy-sector-can-decarbonize-the-world/

Figure 2: Projected power consumption in the future.

The growing environmental consciousness awakened by various international covenants continues to prompt nations to reduce the levels of greenhouse gas emission, and opt to harvest and deliver cleaner energy from alternate sources involving solar and wind based technologies [4]. The ultimate and the unlimited source of energy for powering our planet is the sun and the other feasible source of sustainable energy is the wind. During the past decade, significant advancements have occurred in the development of sophisticated photovoltaic panels and wind turbines to harvest the solar energy and the wind energy for generating electricity [5,6]. The scope of tapping energy from these sources is limited because of various constraints. Wind mills are located in remote and vast open locations and solar energy is available only during the day time. These factors impose limitations on all the three important components of energy delivery, vis-à-vis generation, storage and transmission[7].

Energy storage is one of the key components for devising sustainable energy systems [8]. Current sustainable technologies of energy harvesting, based on photo-voltaic panels and wind turbines, facilitate the generation of pollution free and clean energy. However, their intermittent nature of power generation prevents them from becoming primary energy exporters [9]. Emerging energy storage technologies have the potential to offset the intermittency problems of the renewable energy sources by storing the generated intermittent energy and making it accessible upon demand [10]. In addition to energy grid applications, energy storage systems also have the potential to transform the technology in the automotive systems. Functioning energy storage devices can replace the automotive systems of current transportation technologies from the chemical fuel-based systems into the electricity-based systems. The electric car is a prime example of how energy storage technologies can transform the transportation system into a more sustainable model [11]. Portable electronic devices, which have become ubiquitous in modern society, are also heavily reliant on energy storage technologies. A rapidly developing market for portable electronic devices and hybrid electrical vehicles has led to an urgent demand for established energy storage systems in the modern society [12].

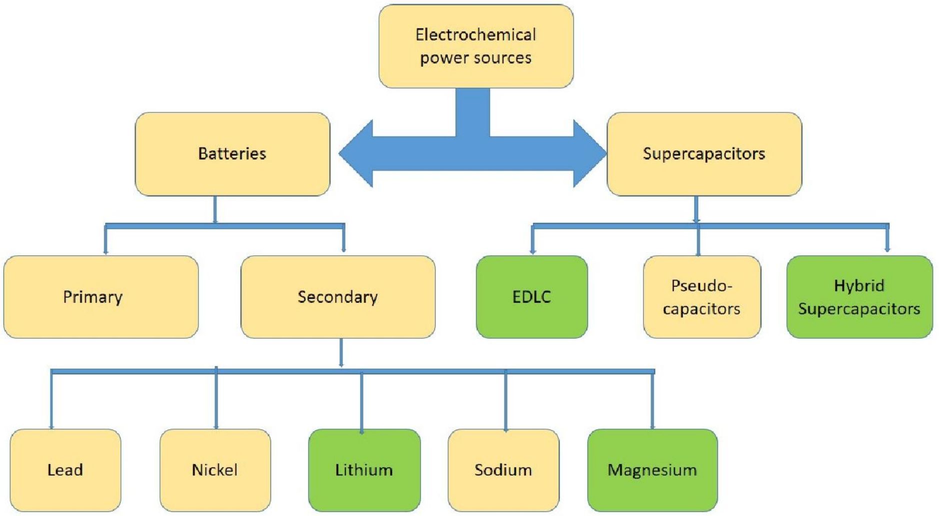

Figure 3: Classification of electrochemical energy storage systems

Electrochemical energy storage systems include the primary (single use) and secondary (rechargeable) cells and the supercapacitors. The electrochemical cells directly convert the chemical energy generated by the exothermal redox reactions into electrical energy. Supercapacitors exchange electrical energy (charge–discharge cycling) via electrostatic, capacitive interactions. The classification diagram is shown in figure 3 [13,14].

In general, the performance efficiency of the electrochemical energy storage systems is evaluated according to their specific power and specific energy [15]. The energy content of the system is to be measured in terms of the energy density (or specific energy) and the power density (or specific power). The energy density is expressed in Watt-hours per litre (Wh L^{-1}) or in Watt-hours per kilogram (Wh kg^{-1}) and the power density in Watts per litre (WL^{-1}) or in Watts per kilogram (W kg^{-1}). These two important parameters turn out, in most of the currently available technologies, to be inversely proportional to each other for several reasons [6]. Optimization of the energy – power proportion is hence the most important goal of any developmental research in the energy storage device technology.

In the realm of electrochemical cells, the intrinsic nature of the redox reactions dictates the general limitations of the energy density and the power density. However, beyond that, engineering aspects are also essential for determining the energy — power ratio of the cells. For the generation and storage of high power, the electrodes have to be as thin as possible, which in effect means that there should be relatively high percentage of the non-reactive parts in the electrodes, indicating the presence of lesser quantity of the active material ,compared to the mass of the current collector. In supercapacitors, the electrostatic interactions involve only small amounts of charge exchange per volume or weight of the electrodes, but these interactions are very fast. Hence, supercapacitors (electric double-layer capacitors – EDLC) exhibit very high power density but relatively low energy density [16,17].

1.2 Basics of the electrochemical cell

Conventionally, the electrochemical cell is an energy conversion system that works on the principle of converting chemical energy into electrical energy through redox reactions. The schematic representation of an ideal electrochemical cell is shown in figure 4.The electrochemical cell is constituted by an anode made of a material (metal or graphite) that can undergo oxidation, a cathode made of a material that can undergo reduction and an electrolyte which facilities redox reactions [18].

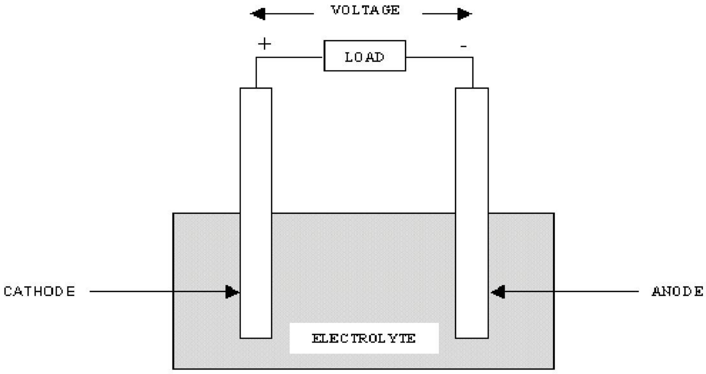

Figure 4: Schematic representation of an ideal electrochemical cell

The potential difference maintained between the anode and the cathode facilities the oxidation of the anode material, whereby electrons are expelled from the anode and the anode atoms are converted into positively charged ions. As the anions travel through the electrolyte to the cathode, the electrons are channelized to the cathode through an external circuit.

The difference between the cathode potential (E_c) and the anode potential (E_a), usually referred to as the cell voltage V, is given by

$$V = E_c - E_a \qquad (1)$$

The values of E_c and E_a of particular materials to be used in a cell are determined against the potential of the standard hydrogen electrode (SHE). The actual potential of an electrochemical cell is always less than the voltage calculated on the basis of equation (1), since, the movement of electrons through the circuit always involves a certain loss of energy due to the internal resistance.

The quantum of energy stored in the cell, referred to as the cell capacity is calculated on the basis of the equation Q = It, where I stands for the current in Amperes (A) and t, for time in seconds (s). The cell capacity is expressed in Ampere second.

Considerable research has gone into the development and sophistication of the battery technology from the time of its inception. In the earliest stage, electrochemical cells were meant only for a limited span of single use, after which they had to be discarded. Such cells are called primary cells and the Dry cells are typical examples. Later on, secondary cells, characterized by the potential to be recharged, were developed. The Ni-Cd cells, lead acid cells and the lithium, sodium and magnesium based cells come under this category. Of these, the lithium based cells are the most preferred ones owing to the beneficial qualities of the lithium metal. Lithium is the lightest and the most electro positive metal, having the high electrode potential of 3.04 volts versus the standard hydrogen electrode[19]. Contemporary rechargeable battery technology relies heavily on lithium based cells. Recently, researchers in this area are found to give significant attention towards the development of sodium and magnesium based cells due to the ubiquitous nature of these metals on earth [20,21].

1.3 Working of the Li-ion cells

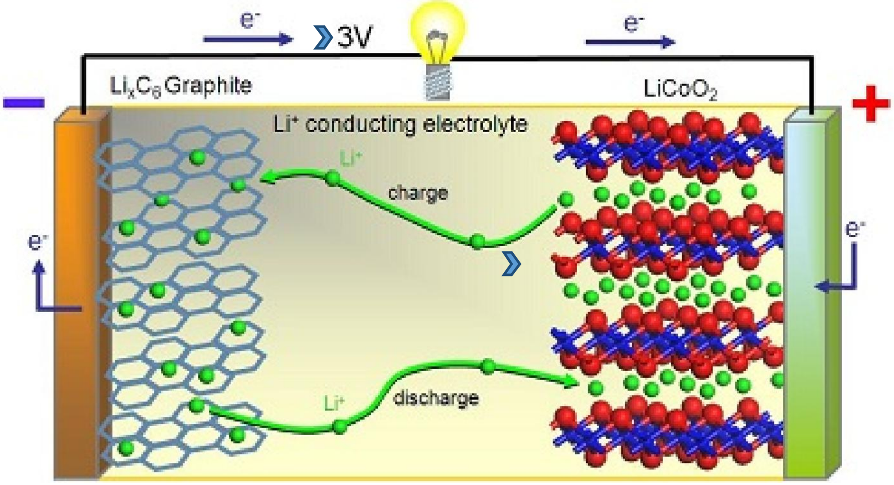

Figure 5: Schematic representation of working of lithium ion cell

In a typical lithium ion cell, the cathode is made of a lithium metal oxide and the anode, of an insertion compound like graphite [22]. The working principle of the Li ion cell is sketched in figure 5. The high electrode potential of the lithium ions facilitates their perennial shuttling between the electrodes through the electrolyte. During the charging process, the lithium ions get deintercalated from the cathode into the electrolyte, culminating in the deposition of an equivalent number of lithium ions from the electrolyte into the anode [23]. Assuming the cathode material to be the lithium cobalt oxide and the anode to be the graphite, the charging and the discharging processes of the Li ion cell can be expressed as

Charging process:

$6C + x\,Li^{+} + x\,e^{-} \rightarrow Li_{x}C_{6}$ (Anode)

$Li_{1-x}CoO_{2} + x\,Li^{+} + x\,e^{-} \rightarrow LiCoO_{2}$ (Cathode)

Discharging process:

$Li_{x}C_{6} \rightarrow 6C + x\,Li^{+} + x\,e^{-}$ (Anode)

$LiCoO_{2} \rightarrow Li_{1-x}CoO_{2} + x\,Li^{+} + x\,e^{-}$ (Cathode)

During the discharge of the cell, the lithium ions are released from the anode into the electrolyte and the ions move towards the cathode through the electrolyte and get intercalated into the cathode. The cathode and the anode are separated from each other using poly propylene or poly ethylene membrane immersed in the electrolyte. The separator facilities the to and fro movement of the lithium ions between the anode and the cathode and also precludes the direct contact between the electrodes, effectively avoiding internal short circuiting. During the charging and the discharging processes, the permanent structural matrix of the electrodes ideally remains intact because the reactions taking place inside the cell are topotactic. The core structural matrix of the electrodes is not involved in any chemical interaction. However, in the long run, physical damage may occur to the electrodes due to the intercalation and the de-intercalation of the ions. [24].

In order to study the optimal performance of the cathode and the anode in a lithium ion cell , the performance of the cathode is evaluated using elementary lithium as the anode , and vice versa. Such a cell, using elementary lithium as the anode or the cathode is called a half cell.

1.4 Working of the lithium-sulfur (Li-S) cells

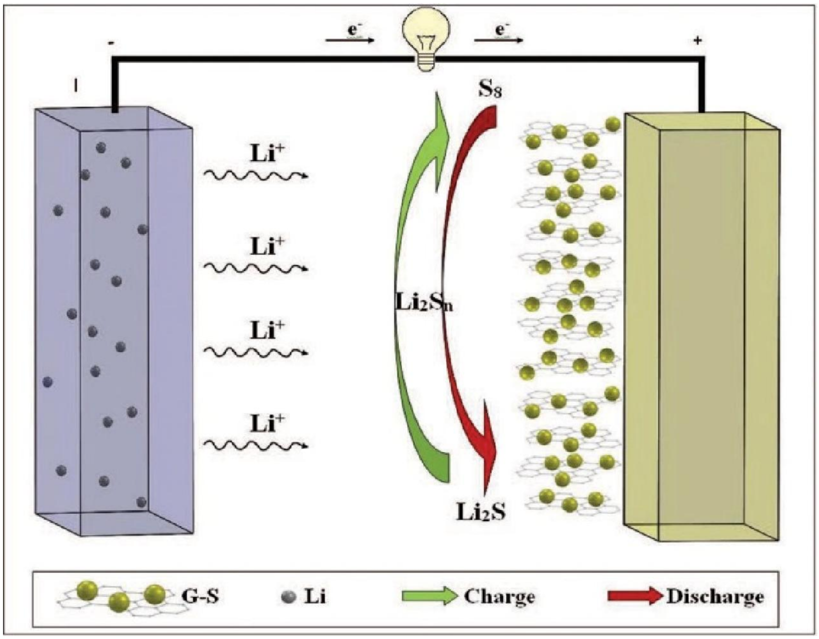

Figure 6: Schematic representation of the working of the lithium sulfur cell.

Most recent research for the improvement of the currently available models of the lithium ion cells involves the quest for more efficient electrode and electrolyte materials. For the anode material, the desirable qualities are the high specific capacity and good safety standards, and for the cathode material, the high specific energy, good rate capability and durability are the preferred traits. [25,26]. One of the most significant advances made in this direction is the use of sulfur as a more efficient alternative for the cathode material of lithium cells. The theoretical specific capacity of sulfur with respect to lithium metal is as high as 1675 mAh g^{-1}[27].

The available configurations of the lithium sulfur cells make use of a sulfur composite (graphite-sulfur composite, G-S) as the cathode, lithium metal as the anode and the electrolyte based on polymers or organic liquids. The lithium sulfur redox reaction in the lithium sulfur cell can be represented using the following equations [26,28,29]

Step I : Reaction of elemental sulfur with lithium

$$S_8 + 2\,Li^+ + 2\,e^- \rightarrow Li_2S_8$$

Step II : Reaction between dissolved Li_2S_8 and lithium

$$Li_2S_8 + 2\,Li^+ + 2\,e^- \rightarrow 2\,Li_2S_4$$

Step III : Transition from dissolved Li_2S_4 to insoluble Li_2S_2 or Li_2S

$$Li_2S_4 + 2\,Li^+ + 2\,e^- \rightarrow 2\,Li_2S_2$$

$$Li_2S_4 + 6\,Li^+ + 6\,e^- \rightarrow 4\,Li_2S$$

Step IV: The equilibrium reaction of insoluble Li_2S_2 and Li_2S

$$Li_2S_2 + 2\,Li^+ + 2\,e^- \rightarrow 2\,Li_2S$$

Under ideal conditions, the lithium-sulfur cells offer a theoretical specific capacity of 1675 mAh g^{-1} and a specific energy density of 2600 Wh Kg^{-1} and these values are almost five times those of lithium ion cells. Apart from these, the natural abundance of sulfur, its low level of toxic impact and the low cost are the other attractive features, which make the Li-S technology, a competent alternative to the Li ion concept.

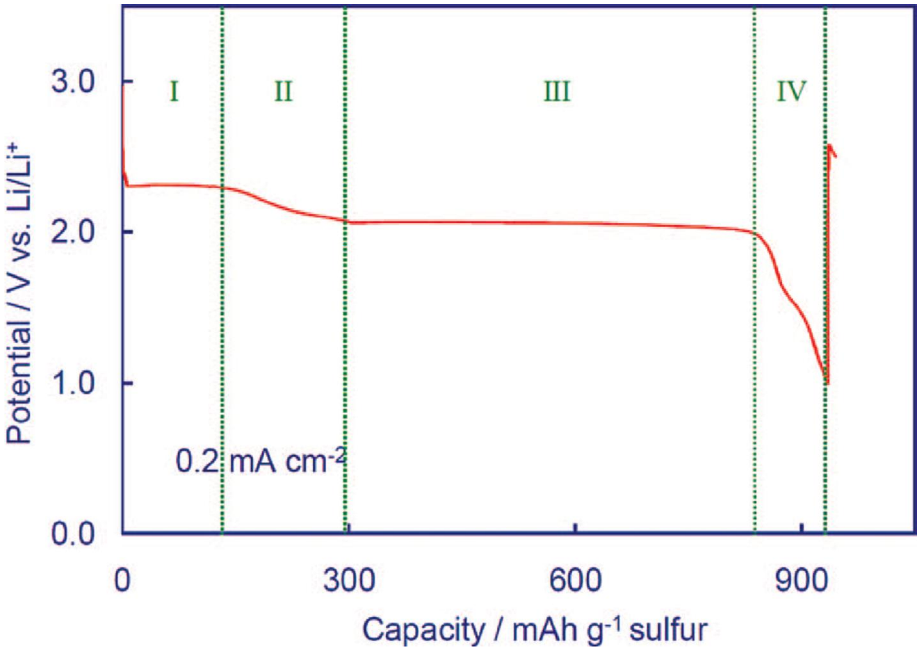

Figure 7:* *The progressive stages of the discharge process of the Li-S cell

The progressive stages of the discharge process in the Li-S cell can be represented as shown in figure 7. The discharge process in the Li-S cell, compared to the intercalation – de-intercalation model of the lithium ion cell, is a multistage electrochemical process, which effectively enhances the specific capacity of the cell.

The electrochemical process of discharge in Li-S cells involves a primary step of forming long chain poly sulfides and a secondary stage, in which the long chain poly sulfides are reduced to shorter poly sulfide chains. The discharge process is complete with the formation of lithium sulfide (Li_2S) [30].

Energy storage systems are constituted mainly by the electrochemical cells and the supercapacitors. The combination of a number of rechargeable cells forms the rechargeable batteries. A harmonizing link between the battery and the supercapacitor is envisaged to be the most optimal energy delivery mechanism for the future. This hybrid mechanism has the potential to optimize the performance of a device by balancing the two mutually exclusive aspects of the energy density of the battery and the power density of the supercapacitor. The supercapacitors are mainly grouped as the electrochemical double layer capacitors (EDLCs), the pseudo capacitors and the hybrid capacitors [16,31,32]. The classification and the description of the electrode materials used in the different types are illustrated in figure 8.

Of these, the EDLCs are non-faradic devices which do not involve any chemical interaction between the electrodes. The pseudo capacitors are faradic devices where redox reactions facilitate the movement of ions between the electrodes. The hybrid capacitors are the combinations of the above two types [31,33].

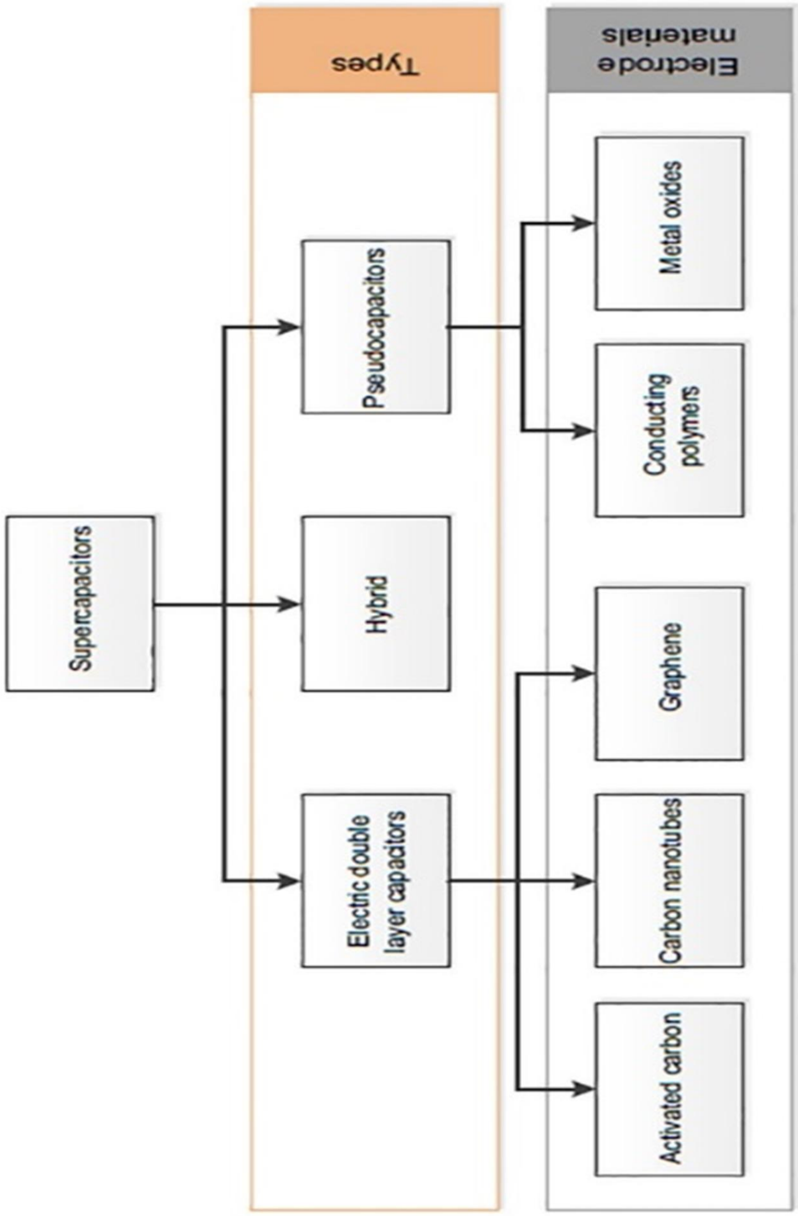

Figure 8: Classification of supercapacitors

1.5 Working of the EDLCs

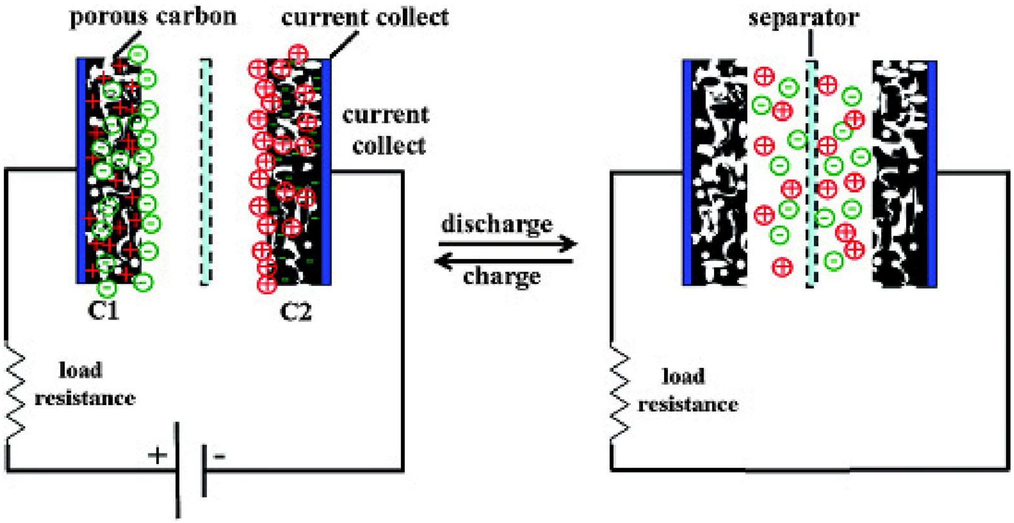

Figure 9: Schematic representation of the working of the EDL capacitor

The EDLCs function on the principle of polarization and the accumulation of the charges on the electrodes and this mechanism is expected to offer quite high power density. The basic working principle of EDLCs is depicted in figure 9. Reversibility of the process is one of the prime advantages of the EDLCs, by which the cycles of charge storage and discharge can be repeated as many as 10^6 times. Another advantage is that there is no electrolytic degradation during the charge- discharge process, as there is no transfer of charges between the electrode and the electrolyte [17,34]. The operation of EDLCs is based on the process of physical adsorption of the charges on the surfaces of the electrodes. Hence it is mandatory to have high surface area for the electrodes to achieve the desired performance efficiency for the supercapacitors. The most suitable materials for EDLCs are the activated carbon, carbon nanotubes and graphene, all of which can have the required extent of higher surface area.

The charging (red colour) and the discharging (blue colour) processes in an EDLC have to be represented separately for the positive and the negative electrodes [35]. If the two electrodes are expressed as E_1 and E_2 , the anion as A^- , the cation as C^+ and the electrode – electrolyte interface by the symbol, // , the electrochemical processes can be expressed as follows.

At the positive electrode,

$$E_1 + A^- \longrightarrow E_1^+ // A^- + e^-$$

$$E_1^+ // A^- + e^- \longrightarrow E_1 + A^-$$

At the negative electrode,

$$E_2 + C^+ + e^- \longrightarrow E_2^- // C^+$$

$$E_2^- // C^+ \longrightarrow E_2 + C^+ + e^-$$

And the overall charge-discharge process can be expressed as,

$$E_1 + E_2 + A^- + C^+ \longrightarrow E_1^+ // A^- + E_2^- // C^+$$

$$E_1^+ // A^- + E_2^- // C^+ \longrightarrow E_1 + E_2 + A^- + C^+$$

1.6 Working of the pseudo capacitor

A pseudo capacitor is so named because it resembles an electrochemical cell, more than a supercapacitor. The Faradic charge transfer in a pseudo capacitor takes place through redox reactions involving the electrodes and the electrolyte [36]. The electrodes in a pseudo capacitor are built of conducting polymers and various metal oxides including RuO_2, MnO_2, and Mn_3O_4 [37,38]. The advantage of the pseudo capacitor over the , EDLC is the possibility of obtaining higher capacitance and energy density. However, it has a lower power density than the EDLC, because the redox reactions at the electrodes take place at a much lower rate than the physical adsorption of charges at the electrodes, happening in the EDLC.

1.7 Hybrid Supercapacitors

As the name indicates, a hybrid supercapacitor makes use of both the redox reactions and the physical adsorption of charges through the selection and combination of suitable materials for constructing the electrodes. In the available models of the hybrid supercapacitors, either the faradic or the non-faradic capacitance mechanisms is seen to dominate [10]. Since hybrid supercapacitors offer a viable model for energy delivery in the years ahead, the recent efforts are directed towards identifying suitable electrode materials capable of combining the high energy density and the specific capacitance of the pseudo capacitors and the high power density and the long cycle life of the EDLCs.

1.8 Terminology used in electrochemical technology

The international union of pure and applied chemistry (IUPAC) has introduced a set of terms to denote the key aspects of electrochemical technology. These include

1. Charge capacity (**Q**)

   It is the total amount of charge available from an electrochemical cell. The unit of charge capacity is mAh or C

2. Specific charge (**q**)

   The specific charge is the charge obtained in one discharge cycle from unit mass of the active material of the cell. The unit of specific charge capacity is mAh g^{-1} or Ah Kg^{-1} or C Kg^{-1}

3. Gravimetric energy density (**W_g**)

   It is the total electrical energy obtained from unit mass of the active material of the cell. The unit of gravimetric energy density is **Wh Kg^{-1}**

4. Volumetric energy density (**W_v**)

   The total electrical energy obtained from unit volume of the active material of the cell is termed as the volumetric energy density and its unit is **Wh L^{-1}**

5. Gravimetric power density (**P_g**)

   It is the power provided by unit mass of the active material of the cell. The unit of gravimetric power density is **W Kg^{-1}**

6. Volumetric power density **(P_v)**

The power supplied by unit volume of the active material of the cell is termed as the volumetric power density and its unit is **W L^{-1}**

7. Columbic efficiency (Φ)

It is the ratio of the energy output on discharge to the input energy upon charging of a rechargeable cell and is expressed in **%.**

8. C rate

The C rate denotes the duration of one full charge or discharge of a cell. It is expressed in **h^{-1}**.

9. Open circuit voltage (**OCV**)

The voltage V_{oc} between the terminals of the cell, when they are not connected to any external load (an "open circuit") and there is no current flow, is termed as the open circuit voltage of the device.

10. Closed circuit voltage (**CCV**)

It is the closed circuit voltage under an external load**.**

11. Load

Anything that draws current from the cell is called as the load.

12. Specific capacitance

It is the ability of a cell to store electric charge for a unit mass of the active material and is expressed in **F/g**

13. Equivalent series resistance (ESR)

    The ESR is the sum of the resistance generated intrinsically by the electrode and the electrolyte materials and the extrinsic resistances such as the mass transfer resistance of the ions and the contact resistance between the current collector and the active materials [39]. It is expressed in ohms.

14. Cycle life

    It indicates the number of charge discharge cycles possible for an electrochemical device during its entire life span, without much loss of the charge storage capacity.

15. Self-discharge rate

    It indicates the rate of discharge in the idle state of any electrochemical device. For any device, the self-discharge has to be minimized for the efficient working of the device.

1.9 Objectives of the present work

The present investigations are mainly focused on identifying the suitable electrode and the electrolyte materials for realizing high power supercapacitors and the Li ion, Mg ion and the Li-S cells with high energy density and good cycling stability. The objectives of the present work can be summarized and listed as follows.

- Assess the suitability of the steam activated, coconut shell derived carbon (CSC) and its three variants obtained by acid washing of the CSC, for high power supercapacitor applications, employing in depth structural and electrochemical characterization.

- Grow manganese oxide (Mn_3O_4), in the form of nanorods, using hydrothermal method, obtain its nanocomposite with reduced graphene oxide (rGO) and study the application prospects of this nanocomposite as the electrode material for developing high power supercapacitors.
- Assemble the lithium-sulfur (Li-S) cells of high discharge capacity, excellent cycling stability and good rate capability, by addressing the challenges related to the lack of electronic conductivity of sulfur in the required range, large volume expansion of sulfur during lithium intake and the formation of soluble polysulphides, during the cycling process. In the present work, the above tasks are expected to be accomplished by using the composite of sulfur with the conducting polymer, PEDOT: PSS, obtained by the hydrothermal technique, as the electrode material.
- Evaluate the suitability of the polymer blend of poly(ethylene oxide) (PEO) and poly(vinyl pyrrolidone) (PVP), complexed with the magnesium salt, $Mg(NO_3)_2$, as the solid electrolyte membrane for applications in all solid state magnesium ion cells.
- Realize the lithium ion full cells using nanostructured $LiFePO_4$ as the cathode active material, the pre-lithiated, coconut shell derived, steam activated and HF washed carbon as the anode material and $LiPF_6$ as the electrolyte.

1.10 References

[1] C. Chae, H.J. Noh, J.K. Lee, B. Scrosati, Y.K. Sun, A high-energy li-ion battery using a silicon-based anode and a nano-structured layered composite cathode, Adv. Funct. Mater. 24 (2014) 3036–3042. doi:10.1002/adfm.201303766.

[2] M.J. Bierman, S. Jin, P.T. Anastas, Energy & Environmental Science, (2009). doi:10.1039/b912095e.

[3] M. Barghamadi, A. Kapoor, C. Wen, A Review on Li-S Batteries as a High Efficiency Rechargeable Lithium Battery, J. Electrochem. Soc. 160 (2013) 1256–1263. doi:10.1149/2.096308jes.

[4] A. Aktas, K. Erhan, E. Ozdemir, S. Ozdemir, Development of a Hybrid Energy Storage System Composed Battery and Ultracapacitor Supplied from Photovoltaic Power Source for 3- phase 4-wire Smart Micro Grid Structure, (n.d.).

[5] A. Jain, V. Aravindan, S. Jayaraman, P.S. Kumar, shells as high energy density cathode, (2013) 1–6. doi:10.1038/srep03002.

[6] A. González, E. Goikolea, J.A. Barrena, R. Mysyk, Review on supercapacitors: Technologies and materials, Renew. Sustain. Energy Rev. 58 (2016) 1189–1206. doi:10.1016/j.rser.2015.12.249.

[7] R. Verrelli, R. Brescia, A. Scarpellini, L. Manna, B. Scrosati, J. Hassoun, A lithium ion battery exploiting a composite Fe2O3 anode

and a high voltage Li1.35Ni0.48Fe0.1Mn1.72O4 cathode, RSC Adv. 4 (2014) 61855–61862. doi:10.1039/C4RA12598C.

[8] Y. V Pant, T.X. Nghiem, R. Mangharam, Peak Power Control of Battery and Super-capacitor Energy Systems in Electric Vehicles, (2014).

[9] M.E. Glavin, P.K.W. Chan, S. Armstrong, W.G. Hurley, I. Fellow, A Stand-alone Photovoltaic Supercapacitor Battery Hybrid Energy Storage System A Stand-alone Photovoltaic Supercapacitor Battery Hybrid Energy Storage System, (2008) 1688–1695. doi:10.1109/EPEPEMC.2008.4635510.

[10] N. Delhi, Batteries and Supercapacitors for Energy Storage and Delivery Needs of India, (2014) 0–39.

[11] M.J. Loveridge, M.J. Lain, I.D. Johnson, A. Roberts, S.D. Beattie, R. Dashwood, J.A. Darr, R. Bhagat, Towards High Capacity Li-ion Batteries Based on Silicon- Graphene Composite Anodes and Sub-micron V-doped LiFePO 4 Cathodes, Nat. Publ. Gr. (2016). doi:10.1038/srep37787.

[12] F. Koushanfar, A. Mirhoseini, Hybrid heterogeneous energy supply networks, Proc. - IEEE Int. Symp. Circuits Syst. (2011) 2489–2492. doi:10.1109/ISCAS.2011.5938109.

[13] D.T.H. Jr, N.P. Balsara, Polymer Electrolytes, Annu. Rev. Mater Res. 43 (2013) 503–525. doi:10.1146/annurev-matsci-071312-121705.

[14] M. Winter, R.J. Brodd, What Are Batteries, Fuel Cells, and Supercapacitors?, Chem. Rev. 104 (2004) 4245–4270. doi:10.1021/cr020730k.

[15] J. Jaguemont, L. Boulon, Y. Dub??, A comprehensive review of lithium-ion batteries used in hybrid and electric vehicles at cold temperatures, Appl. Energy. 164 (2016) 99–114. doi:10.1016/j.apenergy.2015.11.034.

[16] P. Sharma, T.S. Bhatti, A review on electrochemical double-layer capacitors, Energy Convers. Manag. 51 (2010) 2901–2912. doi:10.1016/j.enconman.2010.06.031.

[17] J. Huang, B.G. Sumpter, V. Meunier, Theoretical model for nanoporous carbon supercapacitors, Angew. Chemie - Int. Ed. 47 (2008) 520–524. doi:10.1002/anie.200703864.

[18] P.L. Taberna, P. Simon, J.F. Fauvarque, Electrochemical Characteristics and Impedance Spectroscopy Studies of Carbon-Carbon Supercapacitors, J. Electrochem. Soc. 150 (2003) A292. doi:10.1149/1.1543948.

[19] Z. Zhang, S.S. Zhang, Rechargeable Batteries, 2015. doi:10.1007/978-3-319-15458-9.

[20] D. Aurbach, G.S. Suresh, E. Levi, A. Mitelman, O. Mizrahi, O. Chusid, M. Brunelli, Progress in rechargeable magnesium battery technology, Adv. Mater. 19 (2007) 4260–4267. doi:10.1002/adma.200701495.

[21] I. Hasa, J. Hassoun, Y.-K. Sun, B. Scrosati, Sodium-Ion Battery based on an Electrochemically Converted NaFePO $_4$ Cathode and Nanostructured Tin-Carbon Anode, ChemPhysChem. 15 (2014) 2152–2155. doi:10.1002/cphc.201400088.

[22] M.Y. Ho, P.S. Khiew, D. Isa, T.K. Tan, a Review of Metal Oxide Composite Electrode Materials for, 9 (2014) 1–25. doi:10.1142/S1793292014300023.

[23] T. Osaka, Z. Ogumi, Nanoscale Technology for Advanced Lithium Batteries, 2014. doi:10.1007/978-1-4614-8675-6.

[24] J. Chen, Recent Progress in Advanced Materials for Lithium Ion Batteries, Materials (Basel). 6 (2013) 156–183. doi:10.3390/ma6010156.

[25] M. Wild, L. O'Neill, T. Zhang, R. Purkayastha, G. Minton, M. Marinescu, G.J. Offer, Lithium sulfur batteries, a mechanistic review, Energy Environ. Sci. 8 (2015) 3477–3494. doi:10.1039/C5EE01388G.

[26] W. Kang, N. Deng, J. Ju, Q. Li, D. Wu, X. Ma, L. Li, M. Naebe, B. Cheng, A review of recent developments in rechargeable lithium-sulfur batteries, Nanoscale. 1 (2016) 16541–16588. doi:10.1039/C6NR04923K.

[27] A. Manthiram, Y. Fu, Y.-S. Su, Challenges and Prospects of Lithium–Sulfur Batteries, Acc. Chem. Res. 46 (2013) 1125–1134. doi:10.1021/ar300179v.

[28] Q. Pang, X. Liang, C.Y. Kwok, L.F. Nazar, Advances in lithium–sulfur batteries based on multifunctional cathodes and electrolytes, Nat. Energy. 1 (2016) 16132. doi:10.1038/nenergy.2016.132.

[29] A. Manthiram, Y. Fu, S. Chung, C. Zu, Y. Su, Rechargeable Lithium − Sulfur Batteries, Chem. Rev. 114 (2014) 11751–87. doi:10.1021/cr500062v.

[30] A.F. Hofmann, D.N. Fronczek, W.G. Bessler, Mechanistic modeling of polysul fi de shuttle and capacity loss in lithium e sulfur batteries, J. Power Sources. 259 (2014) 300–310. doi:10.1016/j.jpowsour.2014.02.082.

[31] M. Mastragostino, F. Soavi, C. Arbizzani, Electrochemical Supercapacitors, Adv. Lithium-Ion Batter. (2002) 481–505. doi:10.1007/0-306-47508-1_17.

[32] M. Guerrero, E. Romero, F. Barrero, M. Milanés, E. González, Supercapacitors: Alternative Energy Storage Systems, Prz. Elektrotechniczny Electr. Rev. Page. (2009) 188–195.

[33] A. Burke, Ultracapacitors: why, how, and where is the technology, J. Power Sources. 91 (2000) 37–50. doi:10.1016/S0378-7753(00)00485-7.

[34] P. Simon, A. Burke, Nanostructured carbons: Double-layer capacitance and more, Electrochem. Soc. Interface. 17 (2008) 38–43.

[35] G. Wang, L. Zhang, J. Zhang, A review of electrode materials for

electrochemical supercapacitors, Chem. Soc. Rev. 41 (2012) 797–828. doi:Doi 10.1039/C1cs15060j.

[36] P. Simon, Y. Gogotsi, Materials for electrochemical capacitors, Nat. Mater. 7 (2008) 845–854. doi:10.1038/nmat2297.

[37] K. Wang, X. Ma, Z. Zhang, M. Zheng, Z. Geng, Z. Wang, Indirect Transformation of Coordination-Polymer Particles into Magnetic Carbon-Coated Mn_3O_4 (Mn_3O_4@C) Nanowires for Supercapacitor Electrodes with Good Cycling Performance, Chem. - A Eur. J. 19 (2013) 7084–7089. doi:10.1002/chem.201300188.

[38] Anilkumar .K. M, Manoj. M, Jinisha. B, Pradeep V S, S. Jayalekshmi, Mn 3 O 4 /reduced graphene oxide nanocomposite electrodes with tailored morphology for high power supercapacitor applications, Electrochim. Acta. 236 (2017) 424–433. doi:10.1016/j.electacta.2017.03.167.

[39] B. Dyatkin, O. Gogotsi, B. Malinovskiy, Y. Zozulya, P. Simon, Y. Gogotsi, High capacitance of coarse-grained carbide derived carbon electrodes, J. Power Sources. 306 (2016) 32–41. doi:10.1016/j.jpowsour.2015.11.099.

*References for figures

Figure 1: https://earthhabitat.wordpress.com/2010/02/23/global-energy-sources-2/

Figure 2: https://www.weforum.org/agenda/2018/02/how-electrifying-the-energy-sector-can-decarbonize-the-world/

CHAPTER 2

Relevant Experimental Techniques

Abstract:

Various experimental techniques are used for the characterization of the materials and the devices under investigation, in the present work. This chapter depicts a brief account of the working principle of some of the specific analytical tools used. Characterization techniques, particularly relevant to the present investigations, which include the BET analysis, the PIXE analysis, electron microscopy techniques, cyclic voltammetry, galvanostatic charge discharge test and the electrochemical impedance spectroscopy are briefly described, in this section. Subsequently, the details of the electrode preparation and the assembling of the rechargeable cells and the supercapacitors are also included as an important part of this chapter.

2.1 Techniques used for the characterization of the nanostructured materials, investigated

2.1.1 Field emission scanning electron microscopy (FESEM)

Electron microscopy is a powerful technique, extensively used to analyze the structural and the morphological characteristics of materials, with much higher magnifications and resolutions than optical microscopy. In this technique, a beam of electrons is used to generate an image of the material under study. Using electron microscopes, it is possible to get finer details of low dimensional materials with high resolution and hence they find profound applications in the characterization of nanostructured materials. The field emission scanning electron microscopy (FESEM) and the transmission electron microscopy (TEM) techniques are used for the structural and the morphological analysis of the nanostructured materials, investigated in the present work.

Scanning electron microscopy is a high precision imaging technology, in which a beam of electrons, accelerated by a voltage of 1 to 30 KV is directed to hit the material. As the accelerated electrons interact with the material, secondary electrons, back scattered electrons and auger electrons are released, which can be collected in order to gain information on the surface morphology of the material. [1,2]. Field emission scanning electron microscopy (FESEM) is a higher version of the scanning electron microscopy, in which the electrons are liberated by a field emission source and the material under study is scanned by electrons according to a zig-zag pattern. The FESEM can be utilized to obtain the minute topographical and elemental information of the surface of the material at very high magnifications around 300,000 times. Compared to the conventional scanning electron microscope, the field emission microscope provides quite clear images with practically much less distortion. Since the spatial resolution of this technique is very high, it can be used to observe and study low dimensional structures as small as one nanometer.

In the FESEM technique, the electrons liberated from the field emission source are accelerated in a high electrical field gradient. Within a high vacuum column, evacuated to a pressure down to around 10^{-8} Torr, these primary electrons are focused and deflected by electronic lenses to produce a very narrow scan beam. This electron beam is directed to hit the sample material, which results in the emission of secondary electrons from each spot on the sample surface. The surface details of the sample material can be related to the angle of emission and the velocity of the secondary electrons. The secondary electrons are collected by a detector to generate an electronic signal, which is amplified and transformed to a video scan-image that can be seen on a monitor. The field emission scanning electron microscope is schematically illustrated in figure 1

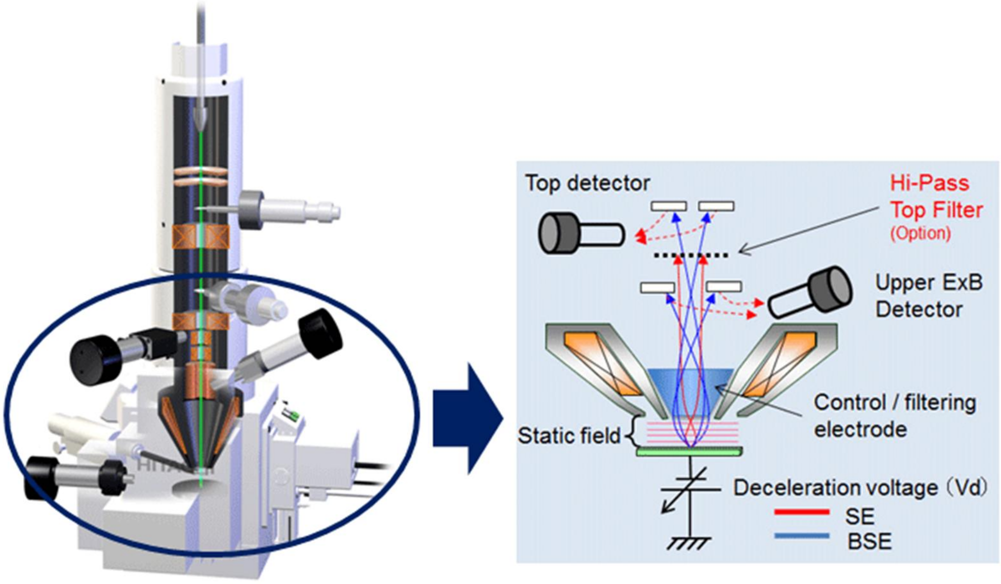

Figure 1: The FESEM

2.1.2 Transmission electron microscopy (TEM)

The transmission electron microscopy is one of the most accurate imaging technologies used in the characterization of nanostructured materials. A beam of electrons is thermionically generated, electromagnetically accelerated and focused on the specimen under study. The electrons penetrating the material can be focused and magnified by magnetic lenses, leading to the formation of a projection image of the material of the desired size. This enlarged image is directed to a fluorescent screen or a layer of photographic film or a CCD camera to gain a clear vision [3,4]. This technique is quite useful to gather information on the morphologic, topographical, compositional and crystallographic details of the materials under investigation.

Figure 2: The HR-TEM

The transmission electron microscope provides high resolution images, offering the most powerful magnification over 1 million times or even more. To obtain high quality TEM images, the materials under investigation have to be made thin enough for electrons to pass through them effectively. The lighter parts of the TEM image represent the areas through which a larger number of electrons can be transmitted, and the darker ones, the dense areas of the material. During the transmission of the electrons through the sample material, the speed of the electrons can be correlated to the electron wavelength. The faster the electrons move, the shorter the wavelength and the higher the quality and the better the details of the images obtained. These differences give valuable information on the structure, texture, shape and size of the material under study. The TEM images open the doors to view the materials on a molecular level, making it possible to analyze the size, shape and the crystallographic details of the particles constituting them. Viewing the TEM images provides the wonderful opportunity to explore the nano-dimensional world in incredible depth and resolution. The photograph of the transmission electron microscope is given in figure 2

2.1.3 The BET surface area analysis

The ratio of surface area to volume, which is not very significant in bulk materials, assumes high significance in the study of nanostructured materials. In nano materials, the increase in the surface area of the particles is responsible for many intriguing properties which are absent in the bulk analogue. It is very important to gauge the surface area of the nano particles in order to calibrate it for various applications. One of the best methods to determine the surface area of the particles at the atomic level is based on gas adsorption. The method is helpful in calculating what is today referred to as the BET surface area, named after the scientists who formulated the equation for the computation of this value [5,6].

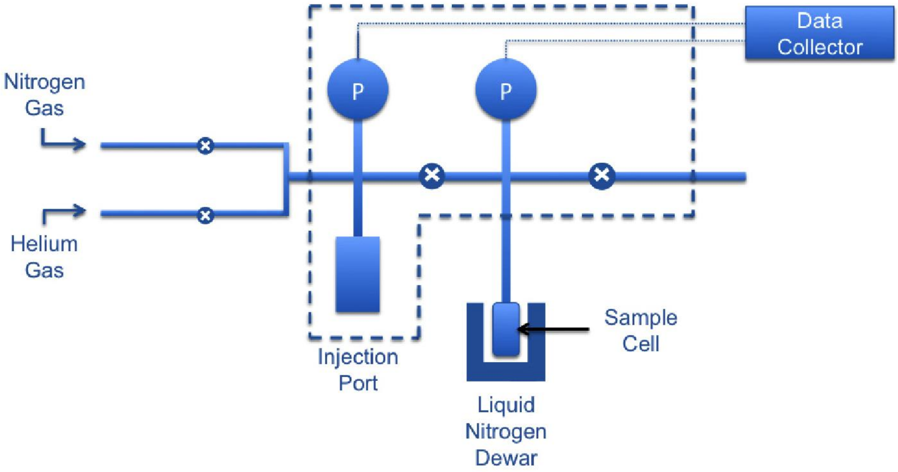

Figure 3: Schematic representation of the BET surface area analysis

The schematic experimental setup for studying the gas adsorption on the surface of the nanostructured material under study and conducting the BET surface area measurements are shown in figure 3. While determining the total surface area of the nano particles, surface irregularities and pore interiors also have to be taken into consideration. Generally it is very difficult to determine the area of surface irregularities and the interior area of the pores, using ordinary spectrometry. In the method of the BET surface area analysis, the total surface area of the nano particles is calculated by measuring the level of adsorption of an inert gas. This method is of very great utility in characterizing nano materials, because the rate of adsorption is not only merely a function of the surface area but of the allied parameters like the temperature, gas pressure and the strength of the interaction between the adsorbent gas and the nano particles, as well.

The BET equation which takes into consideration all these different parameters is given by

$$\frac{1}{X\left[\left\{\frac{P_o}{P}\right\}-1\right]}=\frac{1}{X_m}+\frac{C-1}{X_m C}\left(\frac{P}{P_o}\right)$$

where X is the weight of the inert gas adsorbed at a given relative pressure (P/P_o), X_m is the monolayer capacity, equivalent to the volume of gas adsorbed at the standard temperature and pressure (STP), and C is a constant. The STP corresponds to the temperature of 273 K and the pressure of 1 atmosphere.

The BET theory makes use of the principle of gas adsorption where gaseous molecules physically attach themselves to the surface of a solid without undergoing any chemical reaction. In BET surface area analysis, nitrogen gas is usually employed as the adsorbent and the experiment is carried out under regulated conditions of pressure. The gas is passed into the port holding the material under study and the pressure is increased step by step and the rate of gas adsorption is recorded at every step. The adsorption process stops when the gas pressure reaches a saturation point. Accurately gauged pressure transducers are used to record the pressure changes, resulting from the adsorption process. After reaching the saturation pressure, the material is removed and heated in order to detach the adsorbed gas from the surface of the material for calculations using BET equations.[5,6].

2.1.4 Proton induced X-ray emission (PIXE) analysis

This technique, short titled as PIXE is a highly reliable one in the characterization of multiple elements present in the material under investigation. Protons can generate X- rays from a wide variety of materials, including high atomic number materials present as trace elements in lower atomic number host matrices. Proton induced X- rays can be used to analyze host materials containing many elements simultaneously at ppm levels [7]. The working principle of PIXE is depicted in figure 4 and the schematic diagram is shown in figure 5.

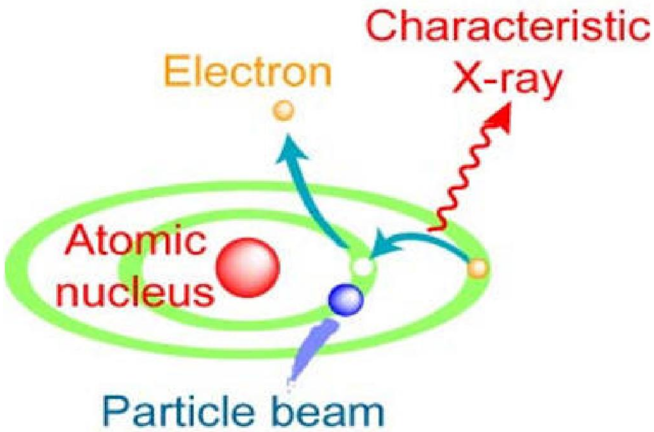

Figure 4: Working principle of PIXE; characteristic X-rays

The PIXE analysis is a two stage process, in which, the primary process involves the identification of the different atomic species present in the material. In the subsequent stage, the amount of the particular elements present in the sample is determined from the intensity of the characteristic X-rays emitted. As the target material is bombarded with a stream of protons, the electrons in the K, L, M ,…. shells of the material get excited to higher energy levels. When these electrons get de-excited to their previous positions they have to shed the excess energy which results in the emission of X-rays. The energy levels of the X-rays emitted are determined by the nature of the elements present in the target material [8]

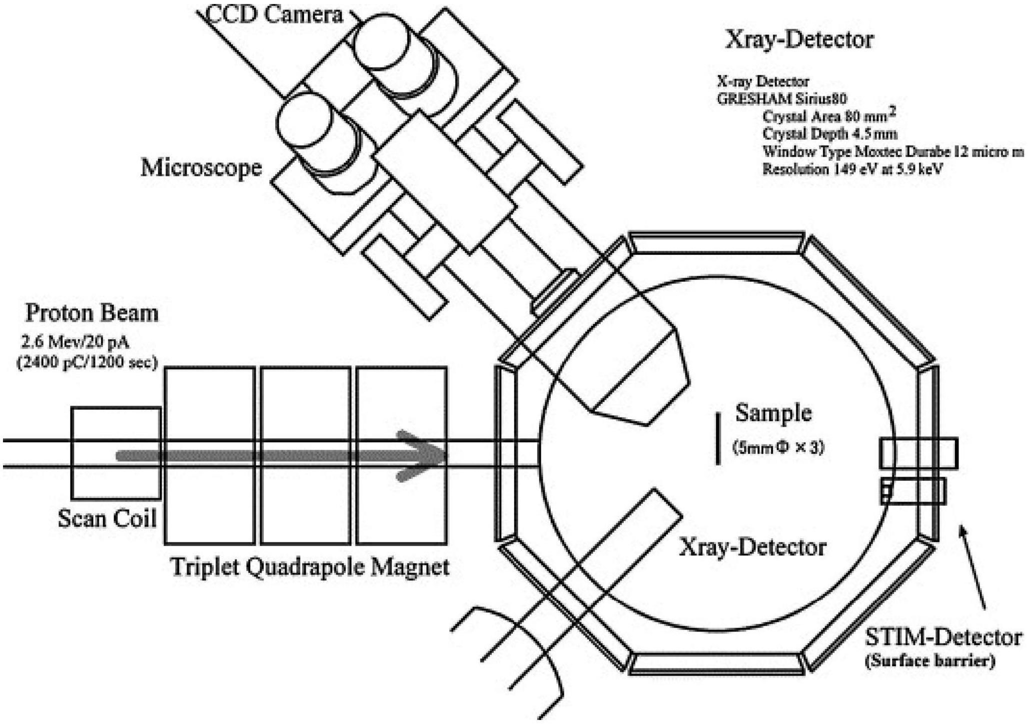

Figure 5: Instrument for PIXE analysis

2.2: Electrochemical characterization

2.2.1 Cyclic voltammetry (CV) studies

The cyclic voltammetry technique is used to analyze the rate of current generation against a range of the applied voltage using the material under investigation as the working electrode, the standard hydrogen electrode (SHE) or the standard calomel electrode (SCE) as the reference electrode and the metals like gold or platinum (inert metals), or lithium or magnesium, depending on the type of the devices used, as the counter electrode. The circuit diagram of a simple cyclic voltammetry setup is shown in figure 6.

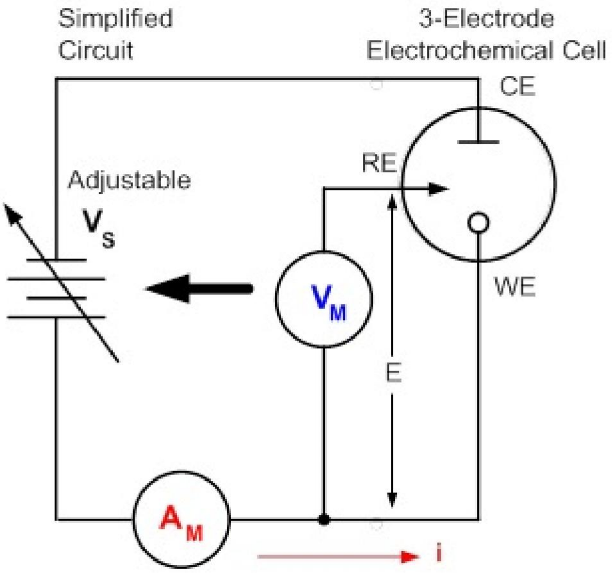

Figure 6: The circuit diagram of the CV setup

The cyclic voltammetry (CV) experiment using the three electrode configuration can be altered to a two electrode method in which the counter electrode can also function as the reference electrode. The three electrode method is useful to investigate the electrochemical characteristics of the materials under study, while the two electrode technique provides information on the overall electrochemical performance of the assembled devices. [9].

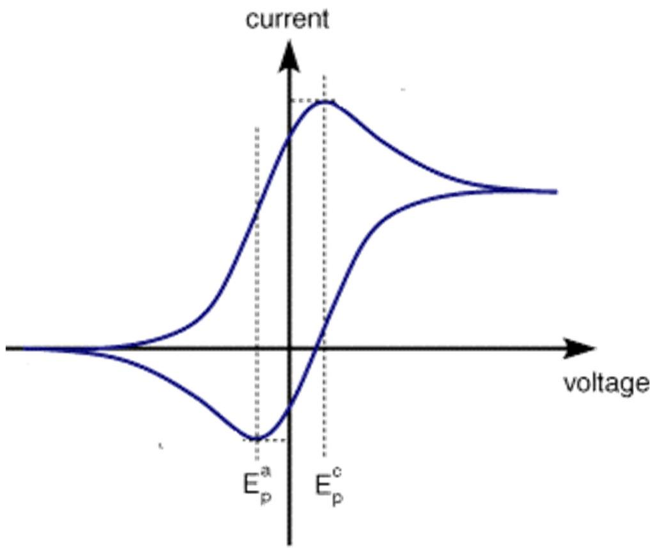

Figure 7: The cyclic voltammetry curve.

A typical CV curve is shown in figure 7. In the CV technique, the voltages at which the maximum oxidation and reduction take place can be accurately determined. At the beginning of the experiment, a small voltage E_1 is maintained between the electrodes. The voltage is gradually swept up or down depending on the properties of the electrode material, at a pre-determined rate to the maximum value E_2 , admissible by the material. During the oxidation cycle, the potential difference at which the maximum number of ions are released is recorded as E_a. During the reverse cycle or the reduction cycle, the potential difference at which maximum reduction occurs is recorded as E_c .The difference between the E_a and the E_c values denotes the operational range of the three electrode electrochemical cell.

The voltammogram obtained during the application of the same procedure to a supercapacitor represents the specific potential at which the capacitor is optimally functional. In the case of the supercapacitor the area of the closed loop obtained on the voltammogram represents its capacitance.

2.2.2 The Galvanostatic charge discharge test (GCD)

The commercial viability of the rechargeable cells or the supercapacitors depends on various parameters such as the internal capacity, number of usable cycles and the shelf life. During the charge discharge cycling test of the device, a steady current is applied between the electrodes to verify the upper and the lower potential limits set for the device. [10].

The gradual increase in the potential difference between the electrodes recorded against the progress of time is graphically sketched with potential difference along the Y axis and time along the X axis. Thus charge discharge cycling test can be appropriately termed as chronopotentiometry carried out under actual working conditions of the device. The method is most useful in determining the capacity, rate capability, and number of usable cycles and the shelf life of the devices. [9]. In the present work the eight channel battery analyzer (MTI corporation), shown in figure 8 is used for the GCD test.

Figure 8: The eight channel GCD set up (MTI Corporation)

2.2.3 Electrochemical impedance spectroscopy (EIS)

In this technique, a small amplitude (~10 mV_{pp}) ac signal is passed through the electrochemical cell in order to study the system properties. The parameters such as the internal resistance, equivalent series resistance, charge transfer resistance and the dielectric relaxation time can be accurately determined, using this technique. Since the current passed is of a very small amplitude and of sinusoidal character, the system is not disturbed drastically and hence the parameters can be encountered in a quasi-equilibrium state.

The excitation of the electrochemical system in response to the applied ac signal can be expressed using the equation $Et = E_o \sin(\omega t)$

Where E_t is the potential at time t, E_0 is the maximum amplitude of the signal, and ω is the radial frequency. The relationship between the radial frequency ω, expressed in radians/second and the frequency f, expressed in hertz is:

The response of the system in the form of ac current can be represented

$$\omega = 2\pi f$$

using the equation $It = I_o \sin(\omega t+\Phi)$

Where I_t, the response signal is shifted in phase Φ and has a different amplitude than I_o.

The impedance of the system which is the ratio between the ac excitation and the ac response can be calculated using Ohm's law

$$Z = \frac{E_t}{I_t} = Z_o(cos\theta + j\ sin\theta)$$

When the right hand side of the above equation is expanded, $Z_o \cos\theta$, the real part of the impedance and $Z_o \sin\theta$, the imaginary part are obtained. Representing the real part on the X axis and the imaginary part on the Y axis, one gets the Nyquist plot, which gives information on a wide variety of parameters with respect to the functioning of the cell. An inherent weakness of the Nyquist plot is that it fails to record the frequency at which a specific impedance is exhibited by the system. This drawback is rectified in the bode plot, in which the real part on the X axis is replaced with logarithmic frequency [11,12]. In the present work the Bio-Logic SP300 Unit, shown in figure 9 is used for the EIS characterization.

Figure 9: Bio-Logic SP300

2.3 The glove box

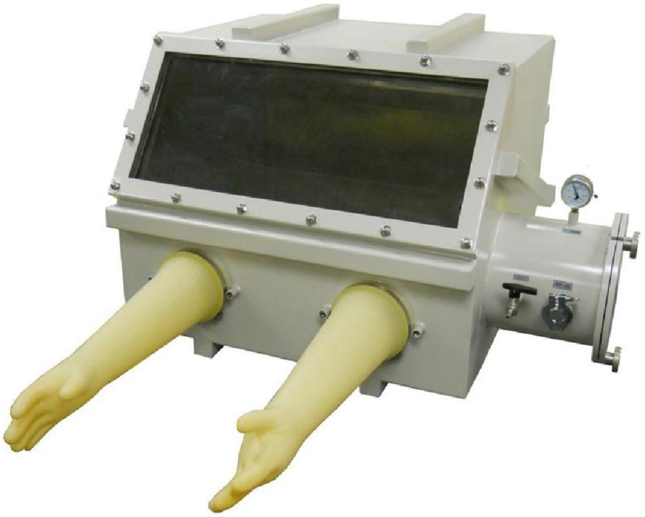

Figure 10: The Glove Box (MTI Corporation)

The electrochemical cell assembly is essentially carried out in a glove box in order to isolate the components as well as the procedures from air and moisture. The glove box (figure 10) is generally purged with argon gas which provides an inert atmosphere inside. To prevent any kind of interaction between the argon gas and the cell components, the gas is circulated over a catalyst [13].

The progression of the activities related to the electrochemical cell assembly can be broadly categorized as (a) Preparation of the electrodes (b) Assembling of the cells and (c) Testing of the cells. The electrochemical cells assembled and tested in the present work include the lithium ion, the magnesium ion and the lithium sulfur cells.

2.4 Electrode preparation

1. The binding material comprising of 10 % of poly vinylidene fluoride (PVDF) in N-methyl 2-pyrrolidone (NMP) is made.
2. The slurry consisting of 80% of the active material, 10% of conductive carbon and 10% of the binding material is made by grinding the components in an agate mortar.
3. The slurry is coated on a thin aluminum foil to make the cathode and on a copper foil to make the anode, meticulously ensuring that the coating is free from the presence of air bubbles.
4. The coated foils are dried in vacuum at 80-120 ºC for about 12 hours.
5. The dried, coated metal foils are punched into discs of 10-16 mm in diameter.
6. The electrode discs are weighed and wrapped before transferring into the glove box.
7. The actual weight of the cathode active material is determined by subtracting the weight of the un-coated metal foil of the same dimension as that of the coated discs.

2.5 The cell assembly stages

1. The cell guard membranes made of poly propylene are punched into discs of diameter 19 mm to be used as separators in the cell.
2. All the prepared and purchased components are transferred into the glove box.
3. One of the cathode material coated, metal foil discs is placed inside the coin cell case and the separator is placed over it. The other electrode, anode, either in the form of a metal foil or like the material coated copper foil, is placed over the separator, after adding two or three drops of the liquid electrolyte, kept inside the glove box.
4. The vacant space within the coin cell case is filled with the spacer and spring and finally the coin cell case is capped.
5. The closed coin cell case is crimped using a crimping machine and the cell is ready for testing

Cell testing involves the following procedures

1. Connect the coin cell to a multimeter to detect the presence of the open circuit voltage (OCV)
2. Once the OCV is ensured the cell can be connected to a computer interfaced battery tester.
3. The functional parameters of the assembled cell can be measured and the cell performance assessed, using various electrochemical characterization tests which include the cyclic voltammetry (CV), the galvanostatic

charge-discharge test (GCD), and the electrochemical impedance spectroscopy (EIS).

2.6 References

[1] J.I. Goldstein, D.E. Newbury, P. Echlin, D.C. Joy, C. Fiori, E. Lifshin, Scanning Electron Microscopy and X-Ray Microanalysis, Springer US, Boston, MA, 1981. doi:10.1007/978-1-4613-3273-2.

[2] D. McMullan, Scanning electron microscopy 1928-1965, Scanning. 17 (2006) 175–185. doi:10.1002/sca.4950170309.

[3] B.D.A. Levin, E. Padgett, C.-C. Chen, M.C. Scott, R. Xu, W. Theis, Y. Jiang, Y. Yang, C. Ophus, H. Zhang, D.-H. Ha, D. Wang, Y. Yu, H.D. Abruña, R.D. Robinson, P. Ercius, L.F. Kourkoutis, J. Miao, D.A. Muller, R. Hovden, Nanomaterial datasets to advance tomography in scanning transmission electron microscopy, Sci. Data. 3 (2016) 160041. doi:10.1038/sdata.2016.41.

[4] D.B. Williams, C.B. Carter, The Transmission Electron Microscope, in: Transm. Electron Microsc., Springer US, Boston, MA, 2009: pp. 3–22. doi:10.1007/978-0-387-76501-3_1.

[5] N. Hwang, a. R. Barron, BET Surface Area Analysis of Nanoparticles, 1 (2011) 1–11.

[6] Adeeco, BET Surface Area Analysis, 1 (2011) 1–11.

[7] I.M. Govil, Proton Induced X-ray Emission - A tool for non-destructive trace element analysis, Science (80-.). 80 (2001) 1542-.

[8] vol. 46(1975) pp. 319. W.Rueter, A.Lurio, E.Cardone and J.F.Ziegler, J. of Applied Physics, Elemental Analysis Inc. | Proton Induced X-ray Emission, (n.d.). http://www.elementalanalysis.com/pixe.html (accessed May 22, 2017).

[9] D.K. Gosser Jr., Cyclic voltammetry: simulation and analysis of reaction mechanisms, (1993) 154.

[10] L.A. Dominey, Lithium Batteries,1995.doi:10.1007/978-3-319-191089.

[11] M.E. Orazem, B. Tribollet, Electrochemical Impedance Spectroscopy, 2008. doi:10.1002/9780470381588.

[12] A. Lasia, Electrochemical Impedance Spectroscopy and its Applications, 2014. doi:10.1007/978-1-4614-8933-7.

[13] Benchtop Vacuum Glove Box (31" x 26" x 28") with Airlock and vacuum Flange & Gauge - EQ-VGB-3, (n.d.). http://www.mtixtl.com/BenchtopStainlessSteelVacuumGloveBox-EQ-VGB-3.aspx

*References for figures

Figure 1 : https://www.zeiss.com/microscopy/int/products/scanning-electron-microscopes/geminisem.html

Figure 2: https://www.jeolusa.com/PRODUCTS/Transmission-Electron-Microscopes-TEM/200-kV/JEM-2100Plus

Figure 3: https://www.researchgate.net/figure/Figure-B-2-5-Schematic-of-BET-surface-analyzer_316673131

Figure 4 : http://www.scienceinschool.org/content/analysing-art-louvre

Figure 5: https://www.sciencedirect.com/science/article/pii/S0168583X03010024

Figure 6: https://www.tek.com/blog/performing-cyclic-voltammetry

Figure 7: https://www.ceb.cam.ac.uk/research/groups/rg-eme/teaching- notes/linear-sweep-and-cyclic-voltametry-the-principles

Figure 8: http://www.mtixtl.com/8ChannelsBatteryAnalyzer-BST8-3.aspx

Figure 9: http://entekelectronic.com/bio-logic/multi-potansiyostat/vsp-300/

Figure 10:http://www.mtixtl.com/BenchtopStainlessSteelVacuumGloveBox-EQ-VGB-3.aspx

CHAPTER 3

Acid Washed, Steam Activated, Coconut Shell Derived Carbon for High Power Supercapacitor Applications

Abstract:

The studies carried out to assess the suitability of the steam activated, coconut shell derived carbon (CSC) and its three variants obtained by acid washing of the CSC, for high power supercapacitor applications, form the focal theme of the present chapter. The structural features of the activated carbon samples are found to improve, after washing with the acids. Out of the three acid washing procedures, washing with hydrofluoric acid (HF) is found to yield activated carbon samples with maximum purity, structural order and the required surface morphology with the optimum ratio of the micropores to mesopores, suitable to facilitate fast ion diffusion and transport. The supercapacitor test cells assembled, using the HF washed, activated carbon as the symmetric electrodes are found to show quite impressive performance characteristics with outstanding cycling stability and excellent retention of the initial capacitance over 5000 cycles.

Anilkumar K M,et al. Acid Washed, Steam Activated, Coconut Shell Derived Carbon for High Power Supercapacitor Applications, J. Electrochem. Soc. 165 (2018) A900–A909. doi:10.1149/2.0491805jes.

3.1 Introduction

Energy harvesting from renewable and inexhaustible natural resources like sun, wind and tide has intensified during the past few decades to meet the alarmingly escalating energy demands of the modern human society These energy resources are more than enough to meet the world's energy requirements and are also more controllable, compared to nuclear energy [1]. The real challenges are not concerned with the scarcity of energy resources, but related to those of efficient energy supply, storage and delivery [2,3]. The criteria of energy storage include the amount and efficiency of storage with respect to the incident energy, its shelf life in the stored device and the time and volume needed for the storage. Energy storage is mandatory because the energy needed for various purposes should be easily accessible, in spite of the variable nature of the utility. Electrical energy is proven to be the most efficient mode of stored energy in this respect. The most competent and controllable mode to store and transmit energy with less loss is also via the electrical energy[4] . Beyond all these, the reactions involving the electrical energy, like the electrochemical reactions in the conversion of the chemical energy into the electrical energy, are considered to be the only one hundred percent 'green reactions' possible today [5]. Among the various types of electrical energy storage devices, the high power density, electrical double layer (EDL capacitors) also known as the supercapacitors and the high energy density batteries are being subjected to extensive research and development processes [6,7]. The EDL capacitors that store energy in non-faradic mode, are efficient in energy delivery in terms of power [8].

The supercapacitors store energy based on the electrostatic interactions of high surface area electrodes. Thereby, their energy density is low and the power density is very high. Also, in terms of their energy storage mechanisms based on the electrostatic interactions, they can demonstrate very long cycle life, with excellent capacity retention and very rapid charging capability[9]. Random porous carbon materials derived from carbon-rich organic precursors are the most widely used electrode materials for electrical double layer capacitors (EDLCs). Large surface area, relatively good electrical properties and moderate cost are the favoring factors of porous carbon materials. Their characteristic features depend to a large extent on the precursors used. Among the raw materials investigated for assembling supercapacitors, based on activated carbon, the coconut shell based carbon materials are most preferred [10,11].

In coconut shell based, porous, activated carbon materials, the limitations on the ordered motion of the crystallites result in the creation of randomly oriented graphene layers, which in turn give rise to an amorphous structure[12]. In activated carbons, the major contribution to the surface area is from the internal surface area of the pores, constituted by the micropores and the mesopores [13]. For the storage of electrical energy using non-faradic processes, similar hierarchical porous nature of the electrodes is preferred. The carbon structures can be tailored to any specific needs in terms of morphology, crystal structure, porosity and surface functionality by means of a wide range of well- established techniques, which include, mild oxidation, chemical activation, template techniques and mechanical, chemical and thermal processes.[14]. Activation of carbon materials can be accomplished by physical or chemical methods[15,16]. Generally, after activation, the carbon materials may contain residual impurities [10]. Developing highly pure, activated, porous carbon materials, free from impurities is beneficial for the improvisation of the performance and stability of the EDL supercapacitors.

The use of pure materials reduces the possibility of formation of dendrites by the reductive deposition of alkali metals or heavy metals, which can cause short circuits. Also, it helps to maintain good shelf life by minimizing the possibilities of self-discharge. [17]. In the presence of impurities, which may act as catalysts, decomposition of the electrolytes through redox reactions can also take place [18],which emphasizes the need for achieving maximum purity for the activated carbon materials.

The focal theme of the present work is to identify the most efficient washing methods to minimize the presence of impurities and obtain cost effective and high quality, activated carbon materials for applications as electrodes in electrostatic supercapacitors, using steam activated carbon, derived from coconut shell.

3.2 Experimental details

3.2.1 Materials and methods

Granular carbon, obtained from coconut shell and steam activated, (CSC) with high specific surface area was acquired from local suppliers and the chemicals, HNO_3 (AR), HCl (AR) and HF(AR) were purchased from Alpha Chemicals, India.

The procedures adopted for making carbon samples with the required structural and morphological characteristics for applications as electrodes in supercapacitors are detailed below. The purchased, coconut shell derived, steam activated carbon (CSC) sample of mass about 20 g was washed well with NaOH solution, a number of times and the washing was continued using distilled and de-ionized water. The thoroughly washed sample was dried overnight at 110 ºC and the resultant carbon sample was named as AC1. In the next step, three batches of 2 g AC1 sample were taken in two borosil round bottom (RB) flasks and one round bottom, high density polyethylene (HDPE) vessel. Freshly prepared, 10 ml solutions of a) 10 vol% aquaregia b) 0.5 M HNO_3 and c) 1.2 M HF in de-ionized water were added into the RB flasks and HDPE vessel respectively [19,20]. The mixtures of AC1 in aquaregia and HNO_3 were heated to their corresponding boiling temperatures and the mixture of AC1 in HF was kept at room temperature. All the mixtures were stirred vigorously for 3-6 hours. Water levels in all the vessels were maintained by adding de-ionized water at regular intervals. Upon cooling, the washed solutions in the

RB flasks and HDPE vessel were decanted and the vessels were refilled with the respective fresh, acid solutions as mentioned earlier and the washing process was repeated twice. Afterwards, the samples were washed with excess de-ionized water until a neutral pH around 6 – 7 was obtained. The samples were then dried in an oven at 110 ° C overnight and were named as AC2 for the aquaregia washed, AC3 for the HNO_3 washed and AC4 for the HF washed ones respectively.

The working electrodes using these carbon samples AC1,AC2, AC3 and AC4 for electrochemical analysis were prepared by mixing 80 wt% of the carbon sample (A1,A2,A3 or A4), 10 wt% of the conducting carbon and 10 wt% of poly(vinylidene fluoride) (PVDF), in the presence of N-methyl pyrrolidinone (NMP), to make a slurry. It was coated on aluminum sheet by spray-coating method and dried at 120 ° C under vacuum overnight. The two-electrode supercapacitor test cells with symmetrical electrodes made of the AC1,AC2,AC3 and AC4 carbon samples, with 2 mg cm^{-2} mass were assembled in a Swagelok type cell using 1M tetraethylammonium tetrafluoroborate in acetonitrile as the organic electrolyte.

3.2.2 Characterization procedures

The elemental analysis of the activated carbon samples, AC1, AC2, AC3 and AC4 was carried out using the Proton Induced X-ray Emission (PIXE) method, from Elemental Analysis Inc., USA. The Raman spectroscopic studies were carried out with the Jobin-Yvon Labram spectrometer using an argon laser

(514.5 nm) in the frequency range of 1000-2000 cm^{-1}.The BET specific surface area (SSA) measurements were done using the Micromeritics Tristar II 3020 surface area analyzer. For this, the samples were degassed at 90 °C for 1 hour and then at 300 °C for 16 hours. The isotherms were plotted by varying the relative nitrogen pressure in between 0. 001 and 0.99. The pore size distribution curve was obtained using the desorption branch of each of the isotherms. The electrochemical characterization was carried out using the Bio-Logic SP300 work station. The cyclic voltammetry (CV) and the galvanostatic charge-discharge (GCD) studies were carried out over the potential range from 0 to 2.5 V, for the assembled, supercapacitor test cells at various scan rates in the range of 10 mV s^{-1} to 100 mV s^{-1} and at different current densities, in the range of 1 A g^{-1} to 10 A g^{-1}. The electrochemical impedance spectroscopic (EIS) studies of the cells were carried out from 200 KHz to 50 mHz, using an ac signal amplitude of 10 mV_{pp}.

3.3 Results and Discussion

3.3.1 Structural characterization

3.3.1.1 Proton induced X-ray emission (PIXE) based elemental analysis

The elemental analysis data of the AC1, AC2, AC3 and AC4 samples, based on the PIXE studies is given in Table 1. The PIXE is an X-ray spectrographic technique, which is used for the non-destructive and

Table 1. ***Elemental analysis data of the optimized samples***

(BDL = below detection limit)

Elements	**Concentration in ppm**			
	AC1	**AC2**	**AC3**	**AC4**
Aluminum (Al)	70	BDL	BDL	BDL
Calcium (Ca)	340	49	16	15
Chlorine (Cl)	89	9000	34	38
Iron (Fe)	57	22	92	6.3
Magnesium (Mg)	300	BDL	BDL	BDL
Phosphorus (P)	117	BDL	BDL	BDL
Potassium (K)	270	37	10	13
Silicon (Si)	390	BDL	BDL	BDL
Sodium (Na)	260	BDL	BDL	BDL
Sulfur (S)	1040	221	322	265

simultaneous elemental analysis of solid, liquid or aerosol samples[21-23]. From the elemental analysis of the AC1 sample, it is found that the major contaminants are S, Si, Ca, Mg, K, Na, P, Cl, Al and Fe. Washing procedures were designed, focused on the removal of contaminants to obtain carbon samples with maximum purity. The elemental analysis of the AC2 sample shows that, aquaregia washing is effective in reducing the elemental contaminations of S, Si, Ca, Mg, K, Na, P, and Fe. However washing with aquaregia results in the increase in the concentration of chlorine from 89 ppm to 9000 ppm. This is most possibly due to the presence of HCl in aquaregia. For the AC3 sample, the analysis shows that, except for the elements S and Fe, the concentrations of all the other elements are reduced to the minimum levels. The HF washing was done on the AC1 sample to obtain the AC4 sample, expecting to minimize the inorganic contaminants to below the detection limit. [21,22]. Elemental analysis of the AC4 sample confirms the effectiveness of HF washing in reducing the concentrations of the contaminants to the minimum levels. The sulfur content is found to be 265ppm in AC4 sample which is an agreeable value for EDLC electrodes [23].

The possibility of formation of undesired, insoluble salts of the contaminant elements, present at the surfaces of the carbon samples may lead to distortion of the textural properties of the pores and surfaces of the samples. To suppress the formation of the insoluble salts, all the samples were washed thoroughly with de-ionized water after the acid treatment

3.3.1.2 Raman spectroscopy studies

The Raman spectra of the carbon samples AC1, AC2, AC3 and AC4 are presented in figure 1. The peak positions, intensity ratios and the lattice parameter details are given in Table 2. The spectra show intense peaks around 1340 cm^{-1} and 1590 cm^{-1} corresponding to the D and G modes of vibrations, respectively. The D band represents the singly degenerate A_{1g} mode which becomes active only in the presence of disorder and its intensity is connected to the vibrations of the 6 fold aromatic rings.

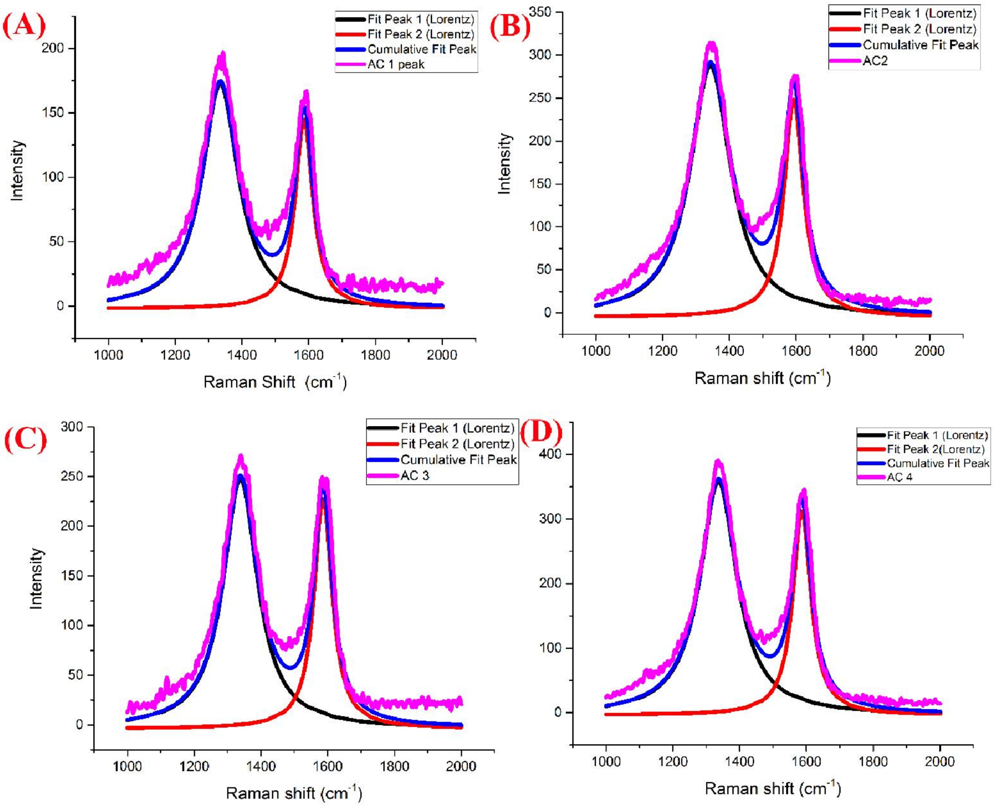

Figure 1: Raman spectra of the activated carbon samples

The G band represents the E_{2g} mode, arising from the sp^2 carbon bond stretching vibrations**.** The presence of the D and G peaks with relative intensity can also be attributed to the presence of polycyclic aromatic rings of increasing crystallite size with lower band gaps having lower frequency breathing modes. It is also an indication of the retention of the carbon skeletal structure of the polycyclic lignocellulose present in the coconut shell [24]. The G peak position around 1590 cm^{-1} indicates that all the four samples are in the amorphous state much closer to the nano-crystalline graphite which fits to the stage 2 of the 3 stage model proposed by Ferrari [25]. High values of I_D and I_G provide evidence for the higher cluster ordering within the amorphous structure. The higher I_D and I_G values of the samples AC2 and AC4 establish the increase in the structural order, as I_D is proportional to the cluster area and I_G portraits the increase in the percentage of sp^2 carbon [24,25].

Table 2 : ***Raman spectroscopic data of the carbon samples***

Samples	**D-peak position (cm^{-1})**	**G-peak position (cm^{-1})**	**FWHM D-peak (cm^{-1})**	**FWHM G-peak (cm^{-1})**	**D-peak Height I_D**	**G-peak Height I_G**	**I_D/I_G ratio**	**L_a (nm)**
AC1	1335	1586	132	65	174	146	1.19	14.14
AC2	1344	1593	148	70	292	253	1.15	14.63
AC3	1339	1587	125	66	251	232	1.08	15.58
AC4	1337	1587	134	66	362	316	1.14	14.76

As per reports, the I_D to I_G ratio depends strongly on the excitation laser energy used in the Raman experiment[26]. The lattice parameter (L_a) values are calculated using the equation given below, proposed by Cancado et al. by considering the strong influence of the excitation energy on the I_D/I_G value

$$L_a\ (nm) = (2.4 \times 10^{-10})\ \lambda_l^4 \times (I_D/I_G)^{-1} \ldots\ldots\ldots\ldots\ldots\ldots\ldots..(1)$$

where λ_l is the laser wavelength in nanometer units [27]. The L_a values of the samples are found to be within the 14 -16 nm range. Higher L_a value of the AC3 sample compared to the other samples can be attributed to the effect of iron contaminant present in the AC3 sample.

3.3.1.3 BET Surface Area analysis

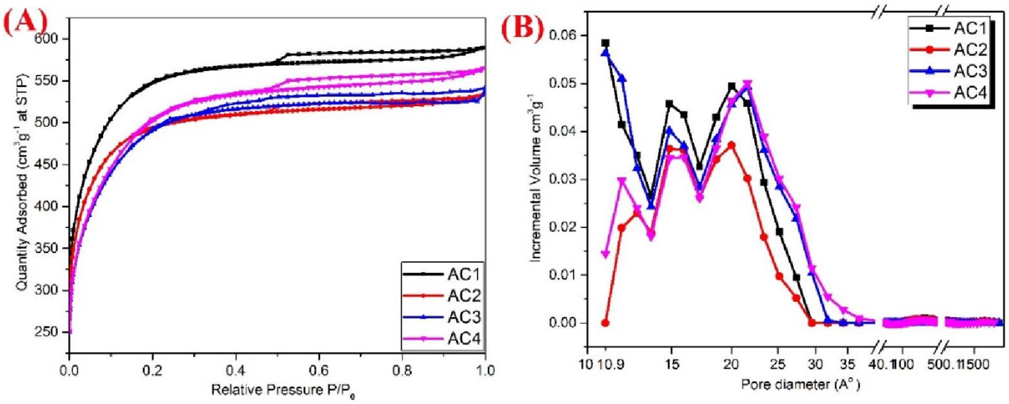

Figure 2 : (A) Adsorption/desorption isotherms and (B) The pore size distribution (the data for plotting is taken from the desorption branches of the isotherms) of the samples.

The BET N_2 adsorption/desorption isotherms of the individual samples and the pore size distribution curves are presented in figures 2A and 2B respectively. The adsorption/desorption isotherms of all the four samples follow similar trend, suggesting that the carbon microstructure is not much affected by adopting different washing procedures. But, they do have some effects in altering the surface area and the pore size of the carbon samples. All the four samples exhibit the type I + IV isotherm, indicating their hierarchical porous nature consisting of micropores and mesopores [28]. Type I isotherms are the characteristic ones for the micro-porous solids [29] and type IV isotherms represent those for meso-porous solids[30] . The absence of a well-defined saturation plateau in the isotherms, indicates the presence of a considerable fraction of macropores also. The microstructure of the carbon samples hence consists of a hierarchical porosity, which spans from the micropores to mesopores and to macropores [31]. The major contribution from the type I isotherms suggests that in all the samples, there is dominance of the micropores.

The contribution of micropores in percentage is given in Appendix A. The increase in the microporous nature of the AC2 sample can be attributed to the pore blocking due to the presence of the comparatively larger sized chlorine impurity either in elemental or in ionic form [10] . These impurities will block the major portion of the available mesopores which results in the conversion of the mesopores into micropores. The presence of the hysteresis loop and the marginal nature of the type IV isotherms clearly indicate the equally comparable importance of the mesopores present. The adsorption - desorption isotherms of all the four samples show a hysteresis of type H4[32]. The H4 hysteresis loops have characteristic desorption shoulders and lower closure points in the region below 0.45 P/P_o. The lowering of the closure points in the case of the AC3 and the AC4 samples indicates the formation of new mesopores from the existing micropores after the washing procedures. The pore shape estimated from the H4 hysteresis loop, in general, is found to be in slit form [33]. The sample AC3 shows slightly enlarged hysteresis loop, compared to the other samples, which is in accordance with the earlier reports that the number of larger pores gets increased with the nitric acid treatment [28]. The surface area of the washed samples is found to be comparatively lesser than that of the non- washed samples, mainly due to the pore collapse which results in the pore blocking effect due to the attrition and the increase in pore diameter from the widening and merging of existing pores due to wall breakage [34] with a corresponding decrease in the surface area. This indicates that the attrition of the connection that interlinks two sites causes a decrease in surface area with micropores combining to form new mesopores. It can be interpreted that no new pores are assumed to be formed due to this process because of the observed decrease in surface area [35].

The specific surface area, S_{BET} of the samples investigated, can be calculated using the BET equation with an accuracy of ± 10 m^2 /g [36]. The total pore volume is obtained from the pore volume data using the equation given below

$$V = V_a \times D \ldots\ldots\ldots\ldots\ldots\ldots\ldots (2)$$

$$\text{Average pore size} = (4 \times V)/ S_{BET} \ldots\ldots\ldots\ldots\ldots\ldots\ldots (3)$$

where V_a is the volume adsorbed at $P/P_0 = 0.99$, D the density conversion factor (0.0015468 for nitrogen as the adsorbate gas). Barrett–Joyner–Halenda (BJH) method is used to obtain the pore size distribution data. Average pore size of the studied samples is calculated using the equation given above, assuming the pores to be cylindrical [37,38].

In the AC2 and AC4 samples, there is not much contribution to the surface area from micropores of size below 1 nm, but in samples AC1 and AC3, the contribution from micropores is comparatively higher and is 58% and 42% respectively, including that from the pores below 1 nm size.

Pore size distribution is obtained from the desorption branches of the isotherms and is shown in figure 2(B). From the analysis, it is found that the surface area contribution of the AC2 sample is mainly from the micropores. The average pore size of the AC2 sample is similar to that of AC1, but the observed comparative reduction in the surface area of AC2 indicates that even though the merging of existing pores has occurred due to pore wall breakage, there is the pore blocking effect of the excess chlorine contaminant present and is evident from the pore distribution graphs. In the case of the AC3 and AC4 samples, the surface area of the micropores decreases compared to the situation in the AC1 and AC2 samples. This is because, on washing with HNO_3 and HF, the walls between the micropores may break to form mesopores and macropores.

3.3.2 Electrochemical Analysis

3.3.2.1 Electrochemical impedance spectroscopic (EIS) analysis

Electrochemical impedance spectroscopy is a powerful tool to understand the electrochemical performance of the supercapacitor test cells. The Nyquist plots of the two electrode supercapacitors, assembled using the four different carbon samples as electrodes are shown in figure 3(A). For any typical plot, the real part represents the resistive characteristics and the imaginary part, the capacitive characteristics of the device. The semi-circular portion generally observed at high frequencies originates due to the contributions from the bulk and interfacial resistances and the steep line observed at low frequencies is the signature of the capacitive properties. These steep lines have finite slopes, representing the diffusive resistivity of the electrolyte within the micropores and mesopores of the electrodes [39]. All these characteristics are observed for the experimental plots of the present work, shown in figure 3(B).

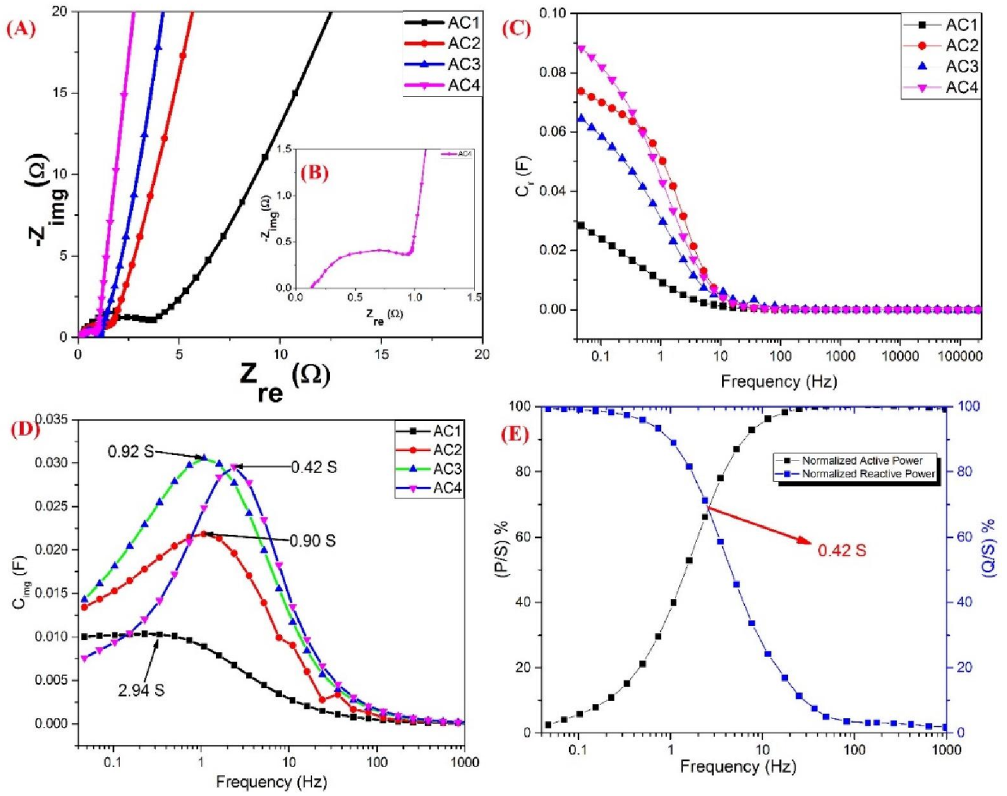

Figure 3 : (A) Nyquist plots of the assembled two electrode supercapacitors in the frequency range, 200 KHz to 50 mHz , (B) Magnified Nyquist plot for the AC4 sample, Plots of the (C) real part and the (D) imaginary part of the capacitance vs frequency and (E) Plots of the normalized reactive power and the active power vs frequency.

The X axis intercept at the high frequency region gives the equivalent series resistance (ESR) which consists of the bulk resistance of the active material and the contact resistance between the active material and the current collector. The charge transfer resistance (R_{CT}) was calculated by extrapolating the semi-circular portion of the Nyquist plot**.**

Table 4 : The ESR , R_{CT} and τ_0 data of the carbon samples

Samples	**ESR (Ω)**	**R_{CT}(Ω)**	**Relaxation Time (s)**
AC1	0.213	4.8	2.94
AC2	0.161	2.49	0.9
AC3	0.190	1.43	0.92
AC4	0.137	1.12	0.42

The very low values of the ESR and R_{CT} of the AC4 sample may be attributed to the extra purity attained after HF washing and consequently the electrolyte can occupy maximum pores as evident from the BET analysis. The higher extent of π electron conjugation in AC4 may enhance the electron mobility and lower the resistive parameters. The higher ordering of the aromatic rings within the pore surfaces as evident from the Raman studies of the AC4 sample and the presence of more mesopores than micropores of size above 1 nm can also lower the ESR and R_{CT}. The ESR of the AC2 sample is lower compared to that of the AC1 and AC3 samples, but R_{CT} is higher compared to that of the AC3 sample. This can be attributed to the excess contamination of chlorine in elemental or ionic form, which is evident from the PIXE analysis and the higher contribution of surface area from the micropores of size above 1nm, as a consequence of the contamination. The vertical nature of the straight lines at low frequencies increases from the sample AC2 to AC3 and to AC4 and this phenomenon is a consequence of the increase in pore size to the mesoporous range, which facilitates a smooth diffusion of the electrolyte within the carbon structure.

The electrochemical behavior of the supercapacitor test cells assembled using the four carbon samples can be analyzed by the complex bode plot using the following equations.

$$C'(\omega) = \frac{-Z''(\omega)}{\omega|Z(\omega)|^2} \quad \dots\dots\dots\dots\dots\dots (4)$$

$$C''(\omega) = \frac{-Z'(\omega)}{\omega|Z(\omega)|^2} \quad \dots\dots\dots\dots\dots\dots (5)$$

where C’(ω) is the real part , which represents the capacitance of the test cell, C’’(ω), the imaginary part, which is related to the energy dissipation during the charge storage process [40] , Z’(ω) and Z’’(ω) , the real and imaginary parts of the complex impedance and ω= 2πf , where f is the scanning frequency. The variation of C’(ω) with frequency is shown in figure 3 (C) and for all the samples the capacitance increases upon decreasing the frequency. The capacitance varies in such a way that, the sample AC1 has the lowest value and the sample AC4,the highest value.

The plots of C''(ω) versus frequency are shown in figure 3 (D) and the C''(ω) values are calculated using equation 5. The imaginary capacitance achieves a maximum value at a particular frequency called as the peak frequency (f_o) and decreases thereafter with the increase in frequency. The peak frequency defines the time constant called as the dielectric relaxation time, τ_o and its values are shown in Table 4. The relaxation time is the minimum time required to discharge all of the stored charge with more than 50 % efficiency. The supercapacitor test cell based on the AC4 sample shows the minimum τ_o, compared to the ones based on the other samples, which indicates that a rapid charge storage / delivery is possible in the test cell assembled using the sample AC4. In the sample AC4, the presence of more number of mesopores compared to micropores facilitates smooth diffusion of ions and brings about the observed lowering of the relaxation time.

To characterize the AC4 sample based supercapacitor test cells in the electrical point of view, the complex power (S (ω)) is determined using the relation S(ω) = P (ω) + j Q (ω) where

$$P(\omega) = \omega\, C''(\omega)|\Delta V_{rms}|^2 \quad and \;\; Q(\omega) = -\,\omega\, C'(\omega)|\Delta V_{rms}|^2$$

and these terms are called active power and reactive power respectively [41]. The plots of the normalized active power and reactive power versus frequency are shown in Figure 3(E). The normalized active power represents the power dissipated in the test cell. All the power gets dissipated at higher frequencies because of the change over from the capacitive behavior to the resistive behaviour upon increasing the frequency. The normalized reactive power increases with decrease in frequency, because the reactive power is due to pure capacitance which dominates at lower frequencies.

3.3.2.2 Cyclic voltammetry studies

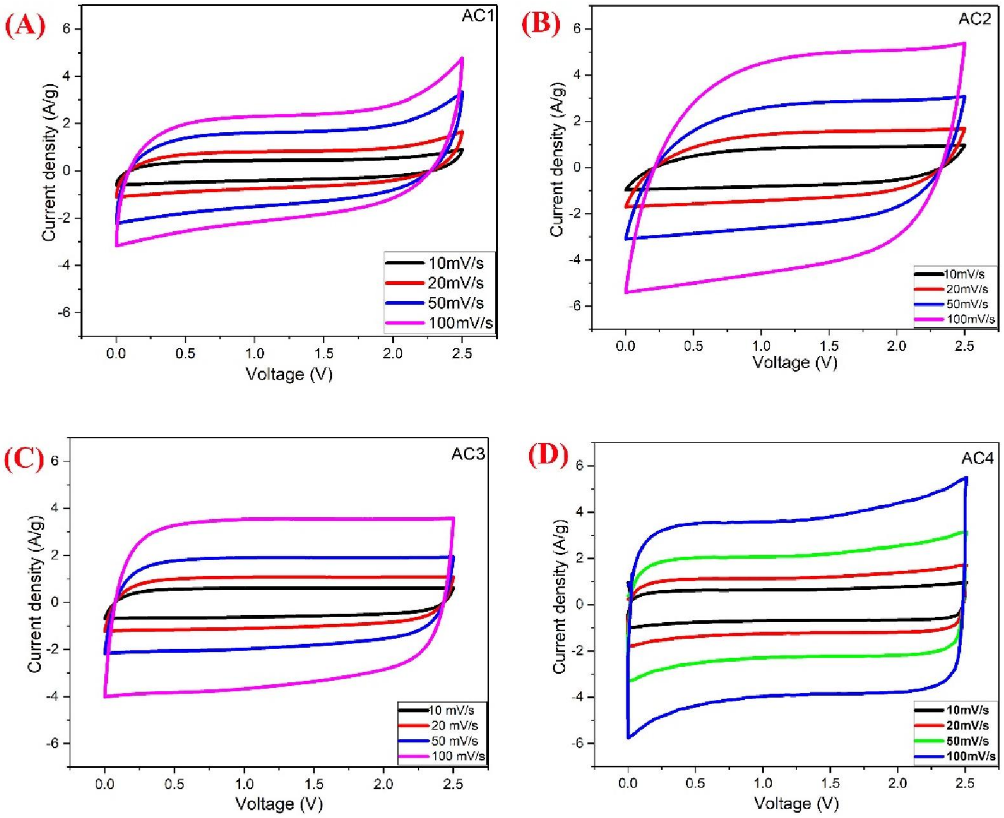

Figure 4: The cyclic voltammetry curves of the test cells based on (A) AC1 (B) AC2 (C) AC3 (D) AC4 samples at different scan rates.

The two electrode CV curves of AC1, AC2, AC3 and AC4 based supercapacitor test cells, recorded at various scan rates of 10 mVs^{-1}, 20 mVs^{-1}, 50 mVs^{-1} and 100 mVs^{-1} in the potential window of 0 to 2.5 V are shown in figure 4. The specific capacitance of the two electrode test cells was estimated from the CV curves using the equation given below. [42,43]

$$C = \frac{1}{m\vartheta\Delta V}\int_{v_0}^{v_1} IVdV \quad \dots\dots\dots\dots(6)$$

where, 'ϑ' stands for the scan rate, 'm', the mass of the active material of the single electrode, and 'ΔV', the potential window. The area under the current-potential curve is calculated using the Origin Lab software.

The specific capacitance of the single electrode is given by C_{sp}= 4C [30,44] and the capacitance values are given in Table 5. For all the four samples, a quasi-rectangular shape is observed for the CV curves, which is characteristic of a double layer capacitance behavior. The rectangular shape of the CV curve is found to get more pronounced as one moves from AC2 to AC3 and to AC4 based test cells. The CV curve of the AC4 sample based cell appears more rectangular in shape compared to those of the other cells mainly due to the lower ESR of the AC4 electrode, which is a consequence of the maximum purity of this sample [45] . The nearly flawless horizontal plateaus in the CV curves of the AC4 based cell indicate the possibility of ion diffusion at a faster rate with a much lower impact from ohmic resistance, compared to the situation in the other three test cells. [46].

Table 5 : ***Specific capacitance of the carbon samples at different scan rates***

Scan Rate mV s^{-1}	***Specific Capacitance (F g^{-1})***			
	AC1	**AC2**	**AC3**	**AC4**
10	102	175	147	182
20	94	154	129	163
50	75	112	92	121
100	53	98	85	104

The higher capacitance observed for the AC4 sample based cell can be related to the highest electrode purity obtained after washing with HF and the increase in the mesopores to micropores ratio[47] as evidenced from the BET analysis. Increase in the above ratio facilitates the easy penetration of the electrolyte ions in to the pores, with the mesopores functioning as channels for the electrolyte to access the inaccessible sites for the double layer formation. The higher capacitance observed for the AC4 electrode based cell can also be attributed to the better mobility of the electrolyte ions in the presence of larger pores [48]. For all the test cells studied, the specific capacitance values decrease with increase in scan rate due to the limited accessibility of the electrolyte ions to the internal pores of the electrodes, when scanned at higher rates.

3.3.2.3 Galvanostatic charge discharge analysis

From the CV analysis, the AC4 based cell is found to show the maximum capacitance and from the EIS measurements, the relaxation time is also observed to be minimum for this sample. Lower relaxation time corresponds to the possibility of achieving higher charge storage and delivery. Galvanostatic charge discharge (GCD) studies in the potential window ranging from 0 to 2.5 V, carried out on the two electrode test cells based on the AC1 and AC4 samples can be used to have an alternate measurement of the capacitance. The charge discharge profiles of the AC1 and AC4 electrodes based test cells at current density values varying from 1 A g^{-1} to 10 A g^{-1} are shown in figures 5(A) and 5(B) respectively with the inset plots representing the IR drop during the discharge.

The charge discharge curves of both the cells show symmetrical profiles during charging and discharging, which is typical of EDLC behavior. Higher potential drop is observed in the discharge curve of the AC1 based test cell due to the lower electronic conductivity of the AC1 electrode compared to AC4. The specific capacitance C of the carbon electrodes [49], and the energy density and the power density [50,51] of the AC1 and AC4 based supercapacitors are evaluated using the equations given below.

$$C = \frac{2\, i \times t}{m \times V} \qquad (7)$$

$$Energy\ Density\ (Wh\ Kg^{-1}) = \frac{CV^2}{8 \times 3.6} \qquad (8)$$

$$Power\ Density\ (W\ Kg^{-1}) = \frac{i\ \times V}{2\ \times m} \times 1000 \qquad (9)$$

where i is the discharge current, t, the discharge time after the potential drop, C, the specific capacitance of the electrode calculated from equation 7, V, the potential window in volts after the potential drop and m, the active mass of the material.

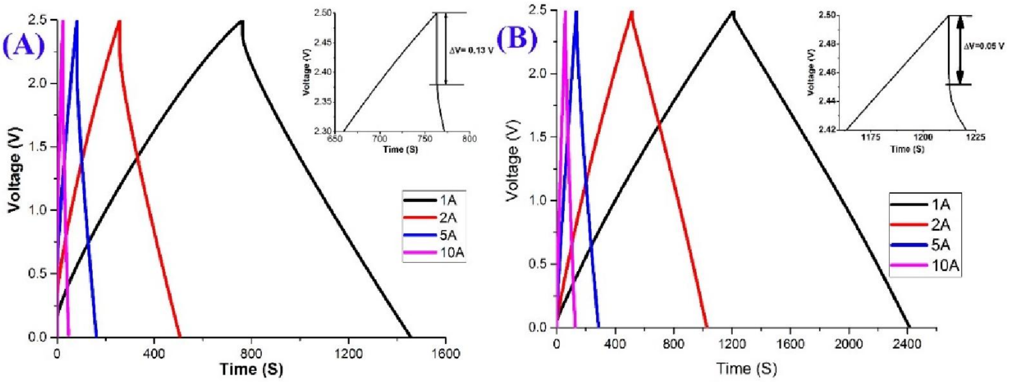

Figure 5 : The GCD plots of test cells based on (A) AC1 (B) AC4 samples at different current densities.

The specific capacitance values of the AC4 based cells are considerably higher than those of the AC1 based cells, and this result is in agreement with the ones obtained from the CV studies. The capacitance drop due to the internal resistance is very small in the AC4 based cell compared to that in the AC1 based cell which contributes towards the enhanced capacitance of the former. A comparison table of the specific capacitance, energy density, and power density of the AC1 and AC4 based test cells are given in Table 6. Compared with the AC1 based test cells, the AC4 based cells show an increased energy density of 35.2 Wh Kg^{-1} at a current density of 1 A g^{-1} and an enhanced power density of 3967 W Kg^{-1} at a current density of 10 A g^{-1}. The lowest relaxation time obtained for the AC4 based cells from the EIS analysis, can be one of the prime factors contributing towards the improved capacitance, power density and the energy density observed in the AC4 electrode based test cells.

Table 6 : ***Specific capacitance , Energy density and Power density of the AC1 and AC4 based test cells at different current densities***

Current density (A g^{-1})	AC1			AC4		
	Specific Capacitance (F g^{-1}	**Energy density (Wh kg^{-1})**	**Power density (W kg^{-1})**	**Specific Capacitance (F g^{-1})**	**Energy density (Wh kg^{-1})**	**Power density (W kg^{-1})**
1	98	21	395	162	35.2	408
2	75	16	723	139	30.2	813
5	64	14	1742	105	22.8	2025
10	55	12	3133	94	20.4	3967

To investigate the electrochemical stability of the AC1 and the AC4 based test cells, the galvanostatic charge discharge cycling was carried out for 5000 cycles from 0 to 2.5 V at a current density of 10 A g^{-1}. The results are shown in figure 6. It can be confirmed that the AC4 based cell shows a highly stable performance compared to the AC1 based cell. The percentage retention of specific capacitance of the two test cells for 5000 cycles is also shown in figure 6. The AC1 based cell shows a capacitance retention of 70 % after 5000 cycles. For the AC4 based cell, 96% of the capacitance is found to be retained after the completion of 5000 cycles. The improved performance of the AC4 based supercapacitor test cell can be ascribed to the optimum surface area, high electrical conductivity and high purity of the AC4 electrode, acquired through washing with HF, which result in low-resistant pathways and short, interconnected channels for easier ion diffusion and electron transport [52] .

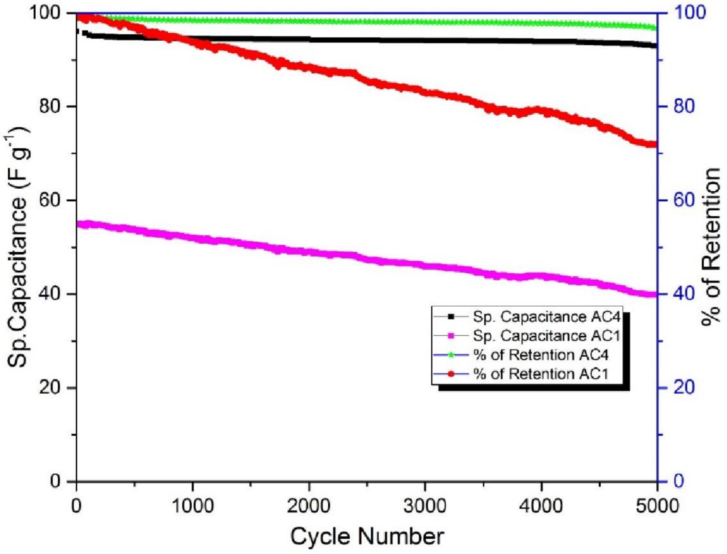

Figure 6: Capacitance retention (%) versus cycle number and the cyclic stability plot for the AC1 and the AC4 based test cells.

3.4 Conclusions

Despite the numerous reports on chemical activation and the performance studies of natural precursor derived carbons in electrochemical applications, the distinguished studies on employing various chemical washing processes on activated carbons, to improve the properties of the nonconducting, amorphous carbon materials, suitably for electrochemical applications are quite scanty. The present work highlights the attempts to develop activated carbon samples with the desired properties for applications as electrode materials for carbon based supercapacitors, by applying various washing processes on CSC (coconut shell derived steam activated carbon) using much lower amounts of chemicals. The present approach is quite different from the so called 'chemical activation' of carbon materials, in which huge amounts of chemicals are used for carbon activation processes, which raise a host of environmental issues. .

The choice of the coconut shell derived carbon, which is an easily available and renewable raw material, its activation process by deploying environmentally benign steam activation method and the subsequent washing procedures using lower amounts of chemicals, emphasize the eco-friendly nature of the processes adopted in the present work.. A detailed comparative study of the CSC and its three variants obtained by washing with aquaregia, HNO_3 and HF has been conducted, employing various characterization methods, with a combination of elemental, surface and structural analysis techniques. Electrochemical techniques are used for calculating the specific capacitance, energy density, power density, ESR and cycling stability and it has been established that the HF washing is the best washing process to obtain the activated carbon samples with the anticipated electrochemical characteristics suitable for applications as electrodes in supercapacitors. The present work portrays the detailed studies on the combinatorial effects of the elemental, surface and structural properties of activated carbon samples obtained using three different chemical washing processes, on their application prospects as electrode materials for EDL supercapacitors.

These effects can be summarized as i) the PIXE analysis demonstrating the maximum purity, ii) the Raman analysis confirming the improved structural ordering and iii) the BET surface analysis revealing the microstructure reformation, facilitating the easy movement of the electrolyte ions to the pores, of the carbon sample AC4, obtained by the HF washing process, in which all the advantageous characteristics are simultaneously achieved. For the AC4 based supercapacitor test cells, an electrode capacitance of 162 F/g with an energy density of 35.2 Wh kg^{-1} at a current density of 1 A g^{-1} and a power density of 3967 W kg^{-1} at 10 A g^{-1} along with excellent cycling stability have been achieved. The charge discharge studies show a 95 % retention of the initial capacitance even after 5000 cycles at a current density of 10 A g^{-1} and the EIS measurements give a much lower ESR for the AC4 based test cells. These results emphasize the high application prospects of the HF washed AC4 sample to be used as the electrode material for designing, high power double layer supercapacitors.

3.5 References:

[1] M. Guerrero, E. Romero, F. Barrero, M. Milanés, E. González,

Supercapacitors: Alternative Energy Storage Systems, Prz. Elektrotechniczny Electr. Rev. Page. (2009) 188–195.

[2] F. Koushanfar, A. Mirhoseini, Hybrid heterogeneous energy supply networks, Proc. - IEEE Int. Symp. Circuits Syst. (2011) 2489–2492. doi:10.1109/ISCAS.2011.5938109.

[3] M.E. Glavin, P.K.W. Chan, S. Armstrong, W.G. Hurley, I. Fellow, A Stand-alone Photovoltaic Supercapacitor Battery Hybrid Energy Storage System A Stand-alone Photovoltaic Supercapacitor Battery Hybrid Energy Storage System, (2008) 1688–1695. doi:10.1109/EPEPEMC.2008.4635510.

[4] J. Khan, U. Nasir, Voltage Stabilization of Hybrid Micro-Grid Using Super Capacitors, J. Power Energy Eng. 3 (2015) 1–9.

[5] L.M. Da Silva, M.H.P. Santana, J.F.C. Boodts, Electrochemistry and green chemical processes: Electrochemical ozone production, Quim. Nova. 26 (2003) 880–888. doi:10.1590/S0100-40422003000600017.

[6] F. Zhang, T. Zhang, X. Yang, L. Zhang, K. Leng, Y. Huang, Y. Chen, A high-performance supercapacitor-battery hybrid energy storage device based on graphene-enhanced electrode materials with ultrahigh energy density, Energy Environ. Sci. 6 (2013) 1623–1632. doi:10.1039/c3ee40509e.

[7] Y. V Pant, T.X. Nghiem, R. Mangharam, Peak Power Control of Battery and Super-capacitor Energy Systems in Electric Vehicles, (2014).

[8] A. Mirhoseini, F. Koushanfar, HypoEnergy. Hybrid supercapacitor-battery power-supply optimization for Energy efficiency, 2011 Des. Autom. Test Eur. (2011) 1–4. doi:10.1109/DATE.2011.5763298.

[9] V.B. Kumar, A. Borenstein, B. Markovsky, D. Aurbach, A. Gedanken, M. Talianker, Z. Porat, Activated Carbon Modified with Carbon Nanodots as Novel Electrode Material for Supercapacitors, J. Phys. Chem. C. 120 (2016) 13406–13413. doi:10.1021/acs.jpcc.6b04045.

[10] B. Viswanathan, P.I. Neel, T.K. Varadarajan, Methods of Activation and Specific Applications of Carbon Materials, 2009.

[11] L. Weinstein, R. Dash, Supercapacitor carbons, Mater. Today. 16 (2013) 356–357. doi:10.1016/j.mattod.2013.09.005.

[12] S. Editor, D.J. Lockwood, K.I. Ozoemena, Nanostructure Science and Technology Nanomaterials in Advanced Batteries and Supercapacitors, n.d.

[13] D. Das, D.P. Samal, M. Bc, Preparation of activated carbon from green coconut shell and its characterization, Chem. Eng. Process Technol. 6 (2015) 1415–1420. doi:10.4172/2157-7048.1000248.

[14] K.G. Roberts, B.A. Gloy, S. Joseph, N.R. Scott, J. Lehmann, Life Cycle Assessment of Biochar Systems: Estimating the Energetic, Economic, and Climate Change Potential, Environ. Sci. Technol. 44 (2010) 827–833. doi:10.1021/es902266r.

[15] K. Jurewicz, R. Pietrzak, P. Nowicki, H. Wachowska, Capacitance behaviour of brown coal based active carbon modified through chemical reaction with urea, Electrochim. Acta. 53 (2008) 5469–5475. doi:10.1016/j.electacta.2008.02.093.

[16] K. Wasiński, P. Nowicki, P. Półrolniczak, M. Walkowiak, R. Pietrzak, Processing Organic Waste Towards High Performance Carbon Electrodes for Electrochemical Capacitors, Int. J. Electrochem. Sci. 12 (2017) 128–143. doi:10.20964/2017.01.36.

[17] Y.K. Hideharu Iwasaki, Nozomu Sugo, Mitsunori Hitomi, Shushi Nishimura, Takeshi Fujino, Shigeki Oyama, Activated carbon, method for production thereof, polarizing electrode and electrical double layer capacitor, US Pat. (2003). https://www.google.com/patents/US7759289 (accessed March 31, 2017).

[18] I. Piñeiro-Prado, E.M. , David Salinas-Torres , Ramiro Ruiz-Rosas, Diego, Design of Activated Carbon / Activated Carbon, Front. Mater. 3 (2016) 1–12. doi:10.3389/fmats.2016.00016.

[19] Steven H. Vanderpool, Activated carbon catalysts and preparation of

linear polyethylene polyamines therewith, US Pat. US4584405 (1983).

[20] Yi Youngmi, Study on the degradation of carbon materials for electrocatalytic applications, Genehm. Diss. D (2014).

[21] J. Xu, Q. Gao, Y. Zhang, Y. Tan, W. Tian, L. Zhu, L. Jiang, Preparing two-dimensional microporous carbon from Pistachio nutshell with high areal capacitance as supercapacitor, (2014) 1–6. doi:10.1038/srep05545.

[22] E. Article, Chemical Science core – shell nanoarchitectures from a metal – and a conducting polymer †, Chem. Sci. 7 (2016) 5704–5713. doi:10.1039/C6SC01429A.

[23] C. Linda Zhong, San Diego, ULTRACAPACITOR ELECTRODE WITH CONTROLLED SULFUR CONTENT, US Pat. 2 (2010) US20100097741 A1.

[24] A.C. Ferrari, A Model to Interpret the Raman Spectra of Disordered, Amorphous and Nanostructured Carbons, MRS Proc. 675 (2001) W11.5.1. doi:10.1557/PROC-675-W11.5.1.

[25] A.C. Ferrari, J. Robertson, Interpretation of Raman spectra of disordered and amorphous carbon, Phys. Rev. B. 61 (2000) 14095–14107. doi:10.1103/PhysRevB.61.14095.

[26] T.P. Mernagh, R.P. Cooney, R.A. Johnson, Raman spectra of Graphon

carbon black, Carbon N. Y. 22 (1984) 39–42. doi:10.1016/0008-6223(84)90130-1.

[27] L.G. Cațado, K. Takai, T. Enoki, M. Endo, Y.A. Kim, H. Mizusaki, A. Jorio, L.N. Coelho, R. Magalhães-Paniago, M.A. Pimenta, General equation for the determination of the crystallite size la of nanographite by Raman spectroscopy, Appl. Phys. Lett. 88 (2006) 12–14. doi:10.1063/1.2196057.

[28] Y. Wang, T. Yokoi, S. Namba, T. Tatsumi, Effects of Dealumination and Desilication of Beta Zeolite on Catalytic Performance in n-Hexane Cracking, Catalysts. 6 (2016) 8. doi:10.3390/catal6010008.

[29] M. Lv, W. Xie, S. Sun, G. Wu, L. Zheng, S. Chu, C. Gao, J. Bao, Activated-Carbon-Supported K-Co-Mo Catalysts for Synthesis of Higher Alcohols from Syngas, 2015. doi:10.1039/C5CY00083A.

[30] N. Jäckel, D. Weingarth, A. Schreiber, B. Krüner, M. Zeiger, A. Tolosa, M. Aslan, V. Presser, Performance evaluation of conductive additives for activated carbon supercapacitors in organic electrolyte, Electrochim. Acta. 191 (2016) 284–298. doi:10.1016/j.electacta.2016.01.065.

[31] V.S. Pradeep, D.G. Ayana, M. Graczyk-Zajac, G.D. Soraru, R. Riedel, High Rate Capability of SiOC Ceramic Aerogels with Tailored Porosity as Anode Materials for Li-ion Batteries, Electrochim. Acta. 157 (2015)

41–45. doi:10.1016/j.electacta.2015.01.088.

[32] M. Enterría, F.J. Martín-Jimeno, F. Suárez-García, J.I. Paredes, M.F.R. Pereira, J.I. Martins, A. Martínez-Alonso, J.M.D. Tascón, J.L. Figueiredo, Effect of nanostructure on the supercapacitor performance of activated carbon xerogels obtained from hydrothermally carbonized glucose-graphene oxide hybrids, Carbon N. Y. 105 (2016) 474–483. doi:10.1016/j.carbon.2016.04.071.

[33] K.S.W. SING, L.M. , D. H. EVERETT, R. A. W. HAUL, Reporting physisorption data for gas/solid systems — with special reference to the determination of surface area and porosity, Pure App!. Chem.,. 57 (1985) 603–619. https://www.iupac.org/publications/pac/pdf/1985/pdf/5704x0603.pdf (accessed April 6, 2017).

[34] A.L. Cazetta, A.M.M. Vargas, E.M. Nogami, M.H. Kunita, M.R. Guilherme, A.C. Martins, T.L. Silva, J.C.G. Moraes, V.C. Almeida, NaOH-activated carbon of high surface area produced from coconut shell: Kinetics and equilibrium studies from the methylene blue adsorption, Chem. Eng. J. 174 (2011) 117–125. doi:10.1016/j.cej.2011.08.058.

[35] M.S. Patterson, S.J. Madsen, J.D. Moulton, B.C. Wilson, 0 1991, Time. 91 (1991) 905–908.

[36] S. Brunauer, P.H. Emmett, E. Teller, Adsorption of Gases in Multimolecular Layers, J. Am. Chem. Soc. 60 (1938) 309–319. doi:10.1021/ja01269a023.

[37] E.P. Barrett, L.G. Joyner, P.P. Halenda, The Determination of Pore Volume and Area Distributions in Porous Substances. I. Computations from Nitrogen Isotherms, J. Am. Chem. Soc. 73 (1951) 373–380. doi:10.1021/ja01145a126.

[38] P.R. Aravind, G.D. Soraru, Porous silicon oxycarbide glasses from hybrid ambigels, Microporous Mesoporous Mater. 142 (2011) 511–517. doi:10.1016/j.micromeso.2010.12.033.

[39] K.H. An, W.S. Kim, Y.S. Park, J.M. Moon, D.J. Bae, S.C. Lim, Y.S. Lee, Y.H. Lee, Electrochemical properties of high-power supercapacitors using single-walled carbon nanotube electrodes, Adv. Funtional Mater. 11 (2001) 387–392. doi:10.1002/1616-3028(200110)11:5<387::AID-ADFM387>3.0.CO;2-G.

[40] C. Portet, P.L. Taberna, P. Simon, E. Flahaut, C. Laberty-Robert, High power density electrodes for Carbon supercapacitor applications, Electrochim. Acta. 50 (2005) 4174–4181. doi:10.1016/j.electacta.2005.01.038.

[41] P.L. Taberna, P. Simon, J.F. Fauvarque, Electrochemical Characteristics and Impedance Spectroscopy Studies of Carbon-Carbon

Supercapacitors, J. Electrochem. Soc. 150 (2003) A292. doi:10.1149/1.1543948.

[42] V. Srinivasan, J.W. Weidner, Studies on the Capacitance of Nickel Oxide Films: Effect of Heating Temperature and Electrolyte Concentration, J. Electrochem. Soc. 147 (2000) 880. doi:10.1149/1.1393286.

[43] A.K. M, M. M, J. B, Pradeep V S, S. Jayalekshmi, Mn 3 O 4 /reduced graphene oxide nanocomposite electrodes with tailored morphology for high power supercapacitor applications, Electrochim. Acta. 236 (2017) 424–433. doi:10.1016/j.electacta.2017.03.167.

[44] M.Y. Ho, P.S. Khiew, D. Isa, T.K. Tan, a Review of Metal Oxide Composite Electrode Materials for, 9 (2014) 1–25. doi:10.1142/S1793292014300023.

[45] E.Y.L. Teo, L. Muniandy, E.-P. Ng, F. Adam, A.R. Mohamed, R. Jose, K.F. Chong, High surface area activated carbon from rice husk as a high performance supercapacitor electrode, Electrochim. Acta. 192 (2016) 110–119. doi:10.1016/j.electacta.2016.01.140.

[46] A.K. Arof, M.Z. Kufian, M.F. Syukur, M.F. Aziz, A.E. Abdelrahman, S.R. Majid, Electrical double layer capacitor using poly(methyl methacrylate)–C4BO8Li gel polymer electrolyte and carbonaceous material from shells of mata kucing (Dimocarpus longan) fruit,

Electrochim. Acta. 74 (2012) 39–45. doi:10.1016/j.electacta.2012.03.171.

[47] M.M. Iqbaldin, M. Mohd Iqbaldin, I. Khudzir, M. Mohd Azlan, A. Zaidi, B. Surani, Z. Zubri, PROPERTIES OF COCONUT SHELL ACTIVATED CARBON, J. Trop. For. Sci. 25 (2013) 497–503. https://www.frim.gov.my/v1/JTFSOnline/jtfs/v25n4/497-503.pdf (accessed April 6, 2017).

[48] Y.-J. Kim, B.-J. Lee, H. Suezaki, T. Chino, Y. Abe, T. Yanagiura, K.C. Park, M. Endo, Preparation and characterization of bamboo-based activated carbons as electrode materials for electric double layer capacitors, Carbon N. Y. 44 (2006) 1592–1595. doi:10.1016/j.carbon.2006.02.011.

[49] C. Lei, N. Amini, F. Markoulidis, P. Wilson, S. Tennison, C. Lekakou, Activated carbon from phenolic resin with controlled mesoporosity for an electric double-layer capacitor (EDLC), J. Mater. Chem. A. 1 (2013) 6037. doi:10.1039/c3ta01638b.

[50] Y. Huang, S.L. Candelaria, Y. Li, Z. Li, J. Tian, L. Zhang, G. Cao, Sulfurized activated carbon for high energy density supercapacitors, J. Power Sources. 252 (2014) 90–97. doi:10.1016/j.jpowsour.2013.12.004.

[51] D. Hulicova-Jurcakova, A.M. Puziy, O.I. Poddubnaya, F. Suá Rez-

García, J.M.D. Tascón, G.Q. Lu, Highly Stable Performance of Supercapacitors from Phosphorus-Enriched Carbons, JACS Commun. 131 (2009) 5026–5027. doi:10.1021/ja809265m.

[52] L. Sun, C. Tian, M. Li, X. Meng, L. Wang, R. Wang, J. Yin, H. Fu, From coconut shell to porous graphene-like nanosheets for high-power supercapacitors, J. Mater. Chem. A. 1 (2013) 6462–6470. doi:10.1039/c3ta10897j.

CHAPTER 4

Manganese Oxide/Reduced Graphene Oxide Nanocomposite Electrodes with Tailored Morphology for High Power Supercapacitor Applications

Abstract:

The studies carried out to assess the suitability of the nanocomposite of manganese oxide (Mn_3O_4) and reduced graphene oxide (rGO) as the electrode material for high power supercapacitor applications, form the focal theme of the present chapter. The Mn_3O_4 nanorods are synthesized using the hydrothermal method, the rGO, by the modified Hummer's method and the Mn_3O_4/ rGO nanocomposite is obtained by the physical mixing of the component materials. The electrochemical performance of the nanocomposite electrode, with the component materials taken in 1:1 ratio, in both the three electrode and the two electrode configurations is quite impressive performance characteristics with outstanding cycling stability and excellent retention of the initial capacitance over 5000 cycles.

Anilkumar.K. M , et al ;Mn_3O_4 /reduced graphene oxide nanocomposite electrodes with tailored morphology for high power supercapacitor applications, Electrochim. Acta. 236 (2017) 424–433. doi:10.1016/j.electacta.2017.03.167.

4.1 Introduction

The rapid advancements in the development of portable electronic devices and hybrid electric vehicles, have resulted in a dramatic increase in the demand for developing sustainable energy storage systems. In the quest to meet the growing needs for high power energy storage systems, the supercapacitors have been identified as attractive energy storage devices with versatile application prospects in the present global energy scenario[1]. The supercapacitors are classified mainly as electrical double-layer capacitors (EDLCs) and pseudo-capacitors, based on their charge storage mechanisms and have emerged as leading energy storage devices owing to their long cycle life and high power density. [2]. The charge storage mechanism in EDLCs is based on the electrostatic forces within the electrical double-layers formed along the electrodes with large surface area [3]. Carbon based materials have already been identified as ideal electrode materials for high power density EDLCs but the available energy density of these types of supercapacitors is low [4]. In pseudo-capacitors, fast Faradaic redox reactions are responsible for the charge storage[5]. Supercapacitors based on metal oxides like RuO_2 and IrO_2 and conducting polymers like poly-aniline as electrodes possess good specific capacitance, but, they face limitations due to their poor cycling stability and the high production cost involved. Moreover, the low electrical conductivity and the sluggish redox kinetics of these electrode materials adversely affect the device performance significantly [6,7]. A number of the transition metal oxides

,which include $Co(OH)_2$, $Ni(OH)_2$, Fe_2O, NiO, MnO_2 and Mn_3O_4 have drawn extensive attention as alternative electrode materials to many of the conventional ones, owing to the easy availability of the precursor materials and the possibility of achieving higher capacitance, longer cycle life and stable performance for the supercapacitor devices assembled.[8–12]

Among the above mentioned transition metal oxides, Mn_3O_4, is gaining acceptance as one of the most promising electrode materials for supercapacitor applications, based on some of the laudable features of this material which include the possibility of achieving high capacitance value for the assembled supercapacitors, the low cost and the non-toxic nature of this material [13,14].The application of Mn_3O_4 based electrodes in high power supercapacitors, however, faces limitations due to its low electrical conductivity [15]. But, there are methods to address this issue and one of the most feasible techniques is to enhance the electrical conductivity of Mn_3O_4 by making nano-composites with highly conducting carbon nanostructures [16] Among the nanostructured carbon materials, reduced graphene oxide (rGO) is one of the best choices for supercapacitor applications due to its flexible and porous structure, and the advantageous features of high surface area, high electrical conductivity and good electrochemical stability [12]. Carbon nanotubes (CNTs) are known to have high electrical conductivity, flexibility and good mechanical strength. However the extent of porosity in CNTs is much less compared to that in rGO and graphene [17]**.** The structural characteristics and the electrical and mechanical properties of rGO are almost comparable to those of graphene. Since rGO can be synthesized from graphite using simple techniques, the material cost of rGO is less compared to that of high pure graphene, the synthesis of which involves sophisticated techniques like chemical vapour deposition (CVD) [18]. Embedding Mn_3O_4 in the form of nanorods within a highly conductive carbon based porous matrix like rGO can be beneficial for achieving the desired supercapacitor action. [19]. The resulting high surface area facilitates the generation of electrochemically active sites for charge storage. The possibility of achieving a good extent of tunable porosity for the Mn_3O_4/rGO nano-composite is beneficial for ion transportation and electrolyte permeation [20].

Many reports are available related to the various synthesis approaches and experiments using manganese oxide/rGO hybrid materials as supercapacitor electrodes [21–24]. The Li group has reported a hydrothermal method for the synthesis of Mn_3O_4/rGO nanocomposites of particle size 20–40 nm. The group has developed Mn_3O_4/rGO/activated carbon, asymmetric supercapacitors with a maximum energy density of 34.6 Wh kg^{-1} at a power density of 500 W kg^{-1} in the Na_2SO_4 electrolyte [24]. The Gao group has reported that electrodes made of the crumpled, nitrogen-doped rGO/ultrafine Mn_3O_4 nanocomposites synthesized in their laboratory, exhibit a specific capacitance six times higher than that of pure Mn_3O_4 [25]. The Qiu group's experiments emphasize the impressive performance of the supercapacitors based on rGO/Mn_3O_4 composites, with very high rate of electrochemical capacitance retention (92–94 %), after 1000 continuous cycles of galvanostatic charge–discharge [23] . The Yang group has reported the work on a nanocrystalline Mn_3O_4 /rGO hybrid electrode showing a capacitance of 260 F g^{-1} at 0.25 A g^{-1} in 1 M Na_2SO_4 electrolyte [26]. Reasonable success has already been achieved by scientists in their efforts to improve the electrochemical performance of Mn_3O_4 based electrode materials.

In the present work, a simple physical mixing method is attempted for the synthesis of the Mn_3O_4/rGO nanocomposite, to be used as a supercapacitor electrode material, anticipating impressive device performance. The hydrothermal method in the presence of a surfactant has been employed for the synthesis of Mn_3O_4 in the form of nanorods and the modified Hummer's method for that of rGO.

4.2 Experimental details

4.2.1 Synthesis procedures

All the chemicals used were of analytical grade and deionized water was used for washing purposes and also for making solutions. Manganese acetate tetra hydrate (MATH), hexadecyltrimethylammonium bromide (CTAB), graphite powder and hydrazine hydrate were purchased from Sigma Aldrich.

4.2.1.1 Synthesis of Mn_3O_4 nanorods

The saturated aqueous solution of manganese acetate tetra hydrate (MATH) was obtained by dissolving 4.9 g of MATH (purchased from Sigma

Aldrich), in 20 ml of distilled water and the solution was stirred continuously for 3 hours at 50 ºC. The aqueous solution (1M) of hexadecyltrimethylammonium bromide (CTAB) was added drop wise to the above solution and the stirring was continued until the colour of the solution changed to pink. The resulting solution was then cooled down to 25 ºC with continuous stirring. Afterwards, 10 ml of hydrazine hydrate was added to the solution and the resulting brown colour solution was immediately transferred to a teflon lined autoclave and maintained at 180 ºC for 12 hours. The resulting solution after the hydrothermal reaction was washed several times with ethanol and deionized water, filtered and dried at 80ºC under vacuum for 12 hours to obtain the brown coloured nanorods of Mn_3O_4.

4.2.1.2 Synthesis of rGO

4.2.1.2.1 Synthesis of grapheme oxide

Graphene oxide(GO) was synthesized from graphite powder using the modified Hummer's method based on previously reported procedures [27]. Graphite flakes (3 g) were first mixed with 150 ml of H_2SO_4 and the mixture was ultra-sonicated for one hour. The mixture was stirred for 30 minutes in an ice bath and 9 g of potassium permanganate was added very slowly. The rate of addition of $KMnO_4$ was controlled to maintain the reaction temperature below 20 ºC. After vigorous stirring for 3 hours, the ice bath was removed and the mixture was stirred for 6 hours at 30 ºC. The resulting solution was then diluted by the slow addition of 300 ml of water. The reaction temperature was found to increase rapidly to 100 °C with effervescence and the colour of the solution changed to brown. In the final step, 25 ml of hydrogen peroxide was added to the above solution and the colour changed to yellow. The mixture was purified by washing with 5 % HCl and de-ionized water for several times until the pH of the mixture became 7. The resultant product was dried at 100 °C under vacuum for 12 hours to get GO.

4.2.1.2.2 Synthesis of reduced graphene oxide (rGO)[28]

To start with, 500 mg of GO was mixed with 300 ml of water, followed by ultra-sonication of the dispersion for 3hours to achieve a homogenous solution. As the next step, 50 ml of the reducing agent, hydrazine hydrate was added and the solution was refluxed at 100 °C for 12 hours to complete the reduction process. The reduced GO was obtained as a black solid. This product was filtered and washed with deionized water several times to remove the impurities and dried under vacuum to obtain the reduced graphene oxide (rGO)

4.2.1.3 Physical mixing of the components to generate the Mn_3O_4/rGO nanocomposite samples

A mixture of Mn_3O_4 and rGO in the weight ratio 9:1 was dispersed in acetone and subjected to ultra-sonication for 2 hours. Upon the evaporation of acetone, the nanocomposite of Mn_3O_4 and rGO was obtained in powder form and was marked as MnrGO10. Two more composite samples were obtained with Mn_3O_4 and rGO taken in the weight ratios 7:3 and 5:5 and were marked as MnrGO30 and MnrGO50 respectively. A schematic representation of the synthesis of the Mn_3O_4/rGO nanocomposite is shown in figure 1.Out of the three nanocomposite samples synthesized, MnrGO10, MnrGO30 and MnrGO50, the third sample, MnrGO50 was found to show the best electrochemical behaviour in the initial investigations and hence this sample was selected for all the detailed structural, morphological and electrochemical studies.

4.2.2 Structural and morphological characterizations

The XRD patterns of the synthesized samples were recorded using PANAlytical X'Pert PRO machine with Cu-K_α radiation of wavelength 1.54 Å. The FTIR spectra of the samples were obtained in the wave number range 400–4000 cm^{-1} using the JASCO 4100 model FTIR spectrophotometer. The Raman spectra were acquired using Horiba LabRam (800 mm) HR spectrometer equipped with a 514 nm Argon ion laser of 15 mW power. The field emission scanning electron microscopy (FE-SEM) images were collected using Carl-Zeiss sigma electron microscope. The high resolution transmission electron microscopy (HR-TEM) images were obtained using JEOL/JEM 2100 machine from the Sophisticated Analytical Instrument Facility (SAIF) at STIC, CUSAT, INDIA.The technique of BET analysis was used to estimate the surface area of the synthesized samples using the Micromeritics Tristar II 3020 machine.

4.2.3 The electrochemical characterization

The Mn_3O_4/rGO nanocomposite was assessed for its suitability as the electrode material for high power supercapacitor applications in both the three electrode and the two electrode configurations, by carrying out the detailed electrochemical characterization, using cyclic voltammetry (CV) and galvanostatic charge-discharge (GCD) studies.

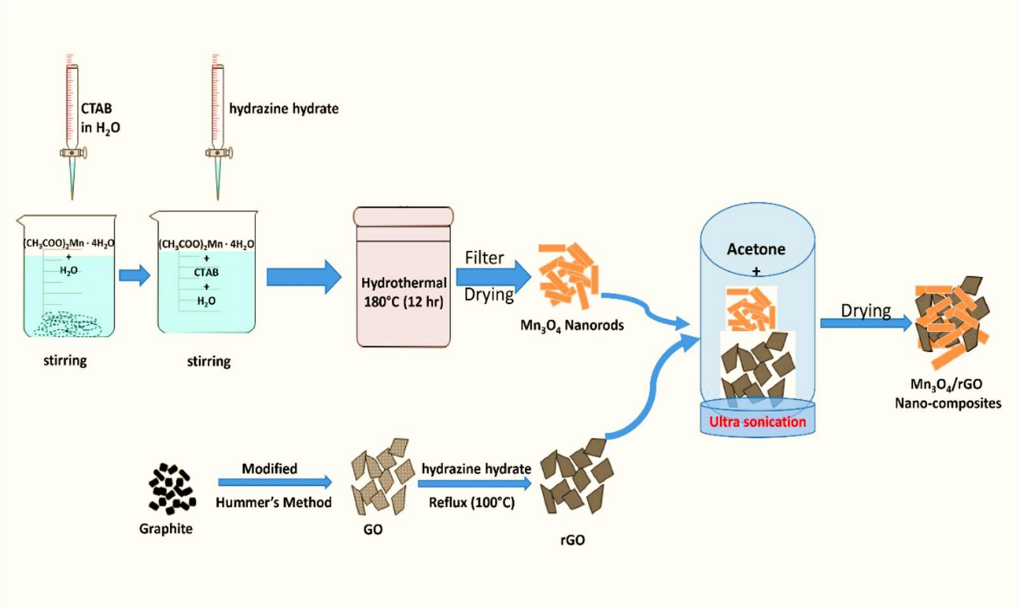

Figure 1: Schematic representation of the synthesis of Mn_3O_4/rGO nano-composite

The working electrodes for the three electrode and the two electrode electrochemical characterization of the Mn_3O_4/rGO nanocomposite were prepared by mixing the nanocomposite material(80% by weight) with conducting carbon black(10%) and the binder material, poly(vinylidene difluoride)(10%) in the presence of N-methyl pyrrolidinone (NMP), to make a slurry. The slurry was pasted on stainless steel discs of diameter 16 mm and heated at 120 °C under vacuum overnight. The three-electrode configuration was realized using the saturated calomel electrode (SCE) at 0.24 V versus the standard hydrogen electrode (SHE) as the reference electrode, platinum rod as the counter electrode, the synthesized Mn_3O_4/rGO nanocomposite as the working electrode and 1 M Na_2SO_4 as the electrolyte. The two-electrode supercapacitor test cells with symmetrical electrodes made of the MnrGO50 nanocomposite sample were assembled using 1M tetraethylammonium tetrafluoroborate in acetonitrile as the electrolyte. Cyclic voltammetry (CV) and galvanostatic charge-discharge studies were carried out over the potential range from 0 V to 1 V for the three electrode and from 0 to 2.5 V for the two electrode configurations at various scan rates in the range 1 to 50 mV s^{-1} and different current densities ranging from 0.2 A g^{-1} to 5 A g^{-1} using the SP-300 Bio-Logic, electrochemical workstation.

4.3 Results and Discussion

4.3.1 The FTIR and Raman spectroscopic analysis

The Fourier transform infrared spectra (FTIR) of the synthesized GO, rGO, Mn_3O_4 and the typical Mn_3O_4/rGO nano-composites sample, MnrGO50 are shown in figures 2(A) and 2(B) respectively. Out of the three different The FTIR spectrum of GO illustrates O-H (broad coupling) bond vibrations at 3200 cm^{-1} originating from the carboxylic acid, C-O vibrations (epoxy or alkoxy) at 1053 cm^{-1}, C=O vibrations in carboxylic acid at 1219cm^{-1} and carbonyl group vibrations at 1725 cm^{-1}.The C=C band at 1603 cm^{-1} refers to the skeletal vibrations of the non-oxidized graphitic domains[29] After the exfoliated GO is chemically reduced with hydrazine hydrate, peak shifts are observed for the peaks at 1053 cm^{-1} and 1603 cm^{-1} to 1020 cm^{-1} and 1551 cm^{-1}

respectively and considerable reduction in the intensity of the peaks is also observed. The peak at 1725 cm^{-1} also undergoes significant decrease in intensity. The peaks of GO at 1219 cm^{-1} and 3200 cm^{-1} are found to disappear completely in the spectrum of rGO.

The reduction in intensity and the shift in the positions of some of the significant peaks and the disappearance of a few of the signature peaks of GO, after the reduction process, using hydrazine hydrate, provide genuine conformation for the formation of rGO from GO. In figure 2(B), the bands in the range of 400–700 cm^{-1} can be assigned to Mn_3O_4 vibrations. The vibrations at 490 and 620 cm^{-1} correspond to Mn–O stretching modes in the tetrahedral and the octahedral environments respectively. [30]. The peak at 2320 cm^{-1} is related to the impurity peak of carbon dioxide [31]. The one at 3450 cm^{-1} is due to the O–H vibrations of the adsorbed moisture. The characteristic peaks of Mn_3O_4 are retained in the spectrum of the Mn_3O_4/rGO nanocomposite, MnrGO50, without any peak shift. The homogenous physical mixing of Mn_3O_4 and rGO can hence be ascertained.

The Raman spectra of pure Mn_3O_4, rGO and the Mn_3O_4/rGO nanocomposite, MnrGO50are shown in figures 2(C), 2(D) and 2(E) respectively. The minor peaks between 200 cm^{-1} to 400 cm^{-1} as well as the dominant peak at 640 cm^{-1} in the spectrum of Mn_3O_4, shown in figure 2(C) , represent the specific vibrations of pure Mn_3O_4 [32]. In the spectrum of rGO shown in figure 2(D), the ordered, sp_2 bonded carbon gives rise to the G band at

1585 cm^{-1}**.** The disordered layers or edges of rGO are responsible for the D band observed at 1353 cm^{-1}.The extent of disorder in rGO can be estimated on the basis of the intensity ratio of the D and the G bands, I_D/I_G [33]. The intensity ratio, I_D/I_G for the synthesized rGO is 1.13, due to the presence of the unrepaired defects, which are retained after the removal of oxygen moieties [34], suggesting that the reduction of GO leads to the formation of smaller and more disordered layers.

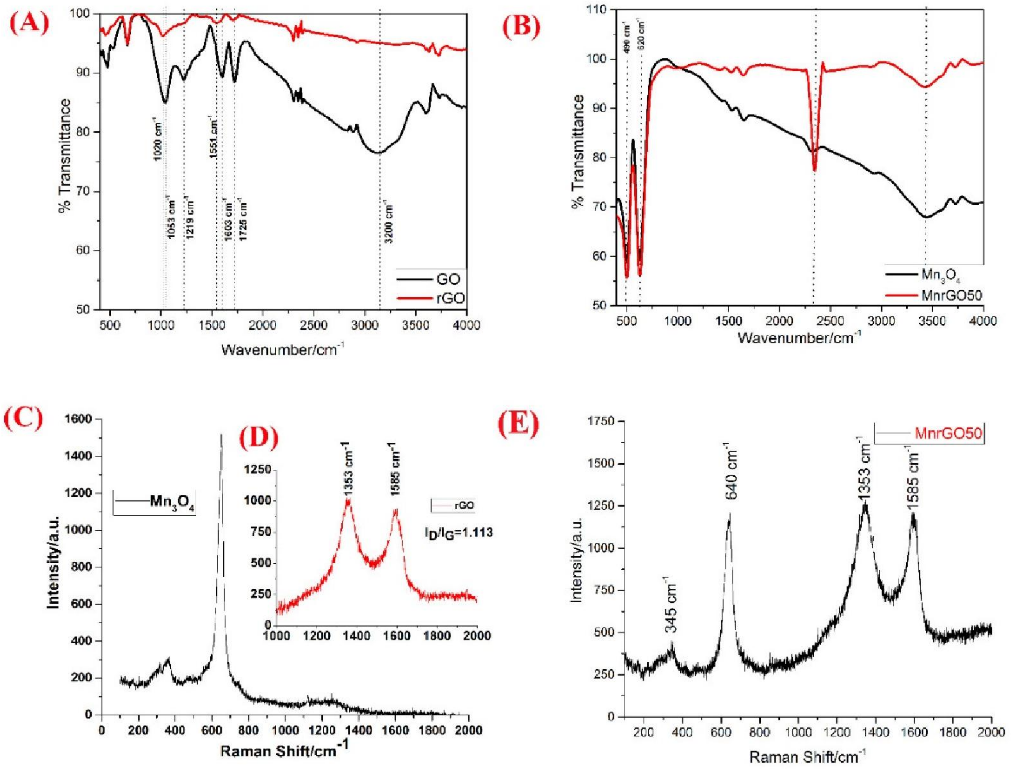

Figure 2: (A) FTIR spectra of GO and rGO , (B) FTIR spectra of Mn_3O_4 and MnrGO50 (C) Raman spectrum of Mn_3O_4 (D) Raman spectrum of rGO (E) Raman spectrum of MnrGO50

The Raman spectrum of the nanocomposite, MnrGO50 shown in figure 2(E) is a combination of that of pure rGO and pure Mn_3O_4. The intensity ratio I_D/I_G for rGO is also retained in the spectrum of the nanocomposite. This implies that Mn_3O_4 and rGO are in their own pristine structures in the nanocomposite and no chemical reactions have occurred between them during the physical mixing process.

4.3.2 The X-ray diffraction (XRD) analysis

The XRD patterns of pure Mn_3O_4, rGO and the Mn_3O_4/rGO nanocomposite are shown in figure 3. The pattern (A) in figure 3 shows the characteristic XRD peaks of rGO and the pattern (B) those of the pure crystalline Mn_3O_4 phase, with no observed impurities. No trace of the Mn_2O_3 phase is observed in the sample [35].

The peak positions agree with the JCPDS card no. 18-0803 with the peaks at 2θ values of 17.83 °, 28.87 °, 31 °, 32.23°, 36.07 °, 44.32 °, 50.57 °, 59.79 °, 60.02 °, 64.67 °, and 74.19 ° corresponding to the (101), (112), (200),(103), (211), (220), (105), (224), (400), and (413) planes respectively of the body centered tetragonal manganese oxide.

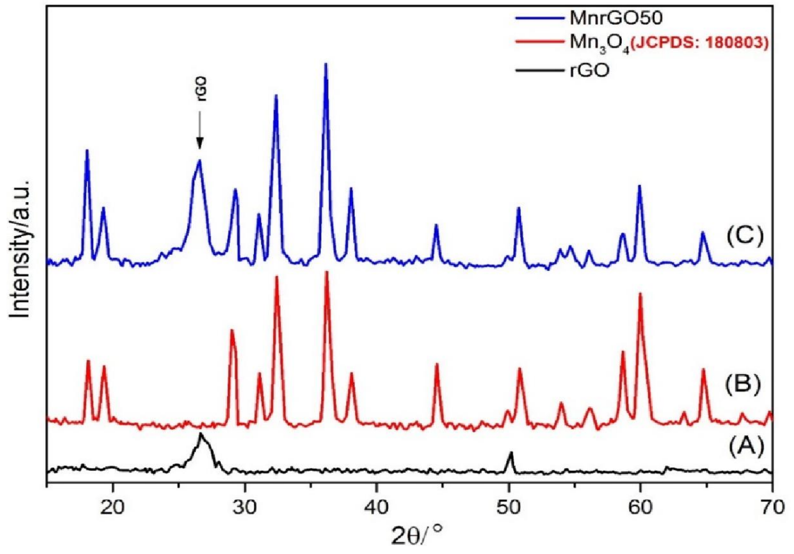

Figure 3: The XRD patterns of rGO, Mn_3O_4 and MnrGO50

The XRD pattern of the Mn_3O_4/rGO nanocomposite, MnrGO50 shown in figure (C) has peaks corresponding to both of the Mn_3O_4 and rGO phases. The figure contains the peaks representing individual Mn_3O_4 and rGO compounds, indicating the homogeneous distribution of Mn_3O_4 within the porous structure of rGO. It can be inferred that in the synthesized nanocomposite, the structural features of the component materials, Mn_3O_4 and rGO are retained without any changes.

4.3.3 Electron microscopy studies: FE-SEM and TEM analysis

The morphological features of the synthesized Mn_3O_4 and rGO samples were analysed using the FE-SEM images shown in figures 4(A) and 4(B) respectively. For the Mn_3O_4/rGO composite sample, MnrGO50, the structural and morphological analysis was done using the TEM images depicted in figures

4(C), 4(D) and 4 (E).The concentration of the surfactant CTAB used in the present work is found to influence the size and shape of the synthesized Mn_3O_4.

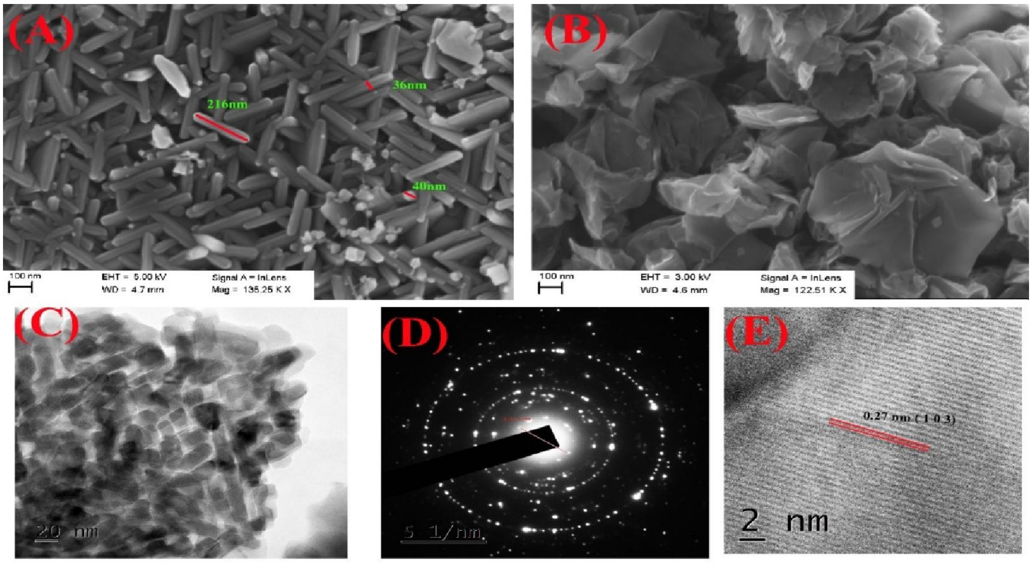

Figure 4 : SEM images of (A) Mn_3O_4 nanorods (B) rGO; TEM image of (C) MnrGO50; SAED pattern of (D) MnrGO50 and TEM image of (E)MnrGO50 showing the inter-planar spacing

The FE-SEM image 4(A) illustrates the formation of quite attractive and homogeneously sized nanorods of Mn_3O_4 of diameter 30-40 nm and length around 216 nm, with minimum agglomerations of the particles, mainly due to the presence of the surfactant CTAB. The flake like structure of rGO is quite evident from the FE-SEM image 4(B). The TEM image shown in figure 4(C) gives a beautiful view of the arrangement of the Mn_3O_4 nanorods within the flakes of rGO. The SAED pattern of MnrGO50 is shown in figure 4(D) in which, the ring patterns indicate the presence of rGO and the dotted ones that of Mn_3O_4. The (1 0 3) plane of the Mn_3O_4 in the MnrGO50 composite is shown in the TEM image 4 (E). These microscopy images establish the homogeneous dispersion of the Mn_3O_4 nanorods within the flakes of rGO upon physical mixing.

4.3.4 The BET Analysis

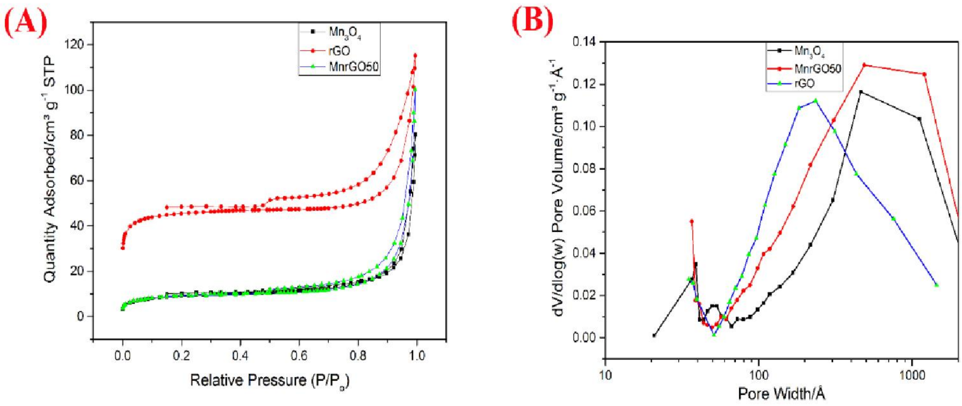

Figure 5: (A) Adsorption/desorption isotherms of Mn_3O_4, rGO and MnrGO50. (B) The pore size distribution plot (the data for plotting is taken from the desorption branch of the isotherm).

The BET adsorption/desorption isotherms of Mn_3O_4, rGO and the Mn_3O_4/rGO nanocomposite sample, MnrGO50, taken under nitrogen atmosphere, are presented in figure 5(A). The pore size distribution is obtained from the desorption branch of the isotherm and is shown in figure 5(B). The specific surface area (S_{BET}) of the samples investigated is determined using the BET equation with an accuracy of ± 10 $m^2\ g^{-1}$ [36]. The total pore volume is obtained from the pore volume data using equation (1);

$$\boldsymbol{V = V_a \times D} \ \ldots\ldots\ldots\ldots\ldots\ldots\ldots\ldots\ldots\ldots\ldots..\mathbf{(1)}$$

$$\boldsymbol{Average\ pore\ size} = \frac{\mathbf{4} \times \boldsymbol{V}}{\boldsymbol{S_{BET}}} \quad \ldots\ldots\ldots\ldots\ldots (\mathbf{2})$$

where V_a is the volume adsorbed at $P/P_0 = 0.99$, D is the density conversion factor (0.0015468 for nitrogen as the adsorbate gas). Barrett–Joyner–Halenda (BJH) method is used to obtain the pore size distribution data. Average pore size of the studied samples is calculated using equation (2) and the pores are assumed to be cylindrical and open at both ends [37,38]. The isotherms fall in class IV according to the IUPAC nomenclature , characteristic of capillary condensation in mesopores, which specifies the mesoporous nature of the materials studied. At lower pressures, the isotherms are not linear which indicates the presence of micropores in the material [37,39,40].

Table 1

The BET surface area, pore volume and the average pore size of the studied samples

Sample	Surface area /m^2 g^{-1}	Pore volume /cc g^{-1}	Pore size /nm
Mn_3O_4	33.9	0.13	15
rGO	172	0.18	4.1
MnrGO50	34.25	0.16	18

The BET isotherm of the rGO is similar to the one with type H3 loops, representing materials comprised of aggregates of plate like particles forming slit like pores [39,40]. For the MnrGO50 composite sample, the adsorption/desorption isotherm resembles that of Mn_3O_4. The presence of a considerable fraction of macropores cannot be ruled out as the isotherms do not show a well-defined saturation plateau. The BET characterization results are summarized in Table 1.

The surface areas of Mn_3O_4 and rGO are 33.9 m^2 g^{-1} and 172 m^2 g^{-1} respectively. The higher surface area of rGO can be linked to its higher value of total pore volume of 0.18 cc g^{-1} with an average pore size of 4.1 nm. The Mn_3O_4 has a pore volume of 0.13 cc g^{-1} and an average pore size of 15 nm. The MnrGO50 composite shows a surface area of 34.25 m^2 g^{-1} with an average pore size of 18 nm. The pore volume and the BET surface area of the composite sample are found to be decreased in comparison with those of rGO, indicating the dispersion of Mn_3O_4 nanorods in rGO and forming a homogeneous mixture. The BET surface area (34.25 m^2 g^{-1}), the pore size (18 nm) and the pore volume (0.16 cc g^{-1}) of the nanocomposite are comparable to those of pure Mn_3O_4 nanorods. The BET results are in agreement with the FE- SEM and TEM analysis, with the pores present in rGO being occupied by the Mn_3O_4 nanorods, in the final nanocomposite.

4.3.5 Electrochemical studies

4.3.5.1 Three electrode studies

The three electrode CV curves of rGO, Mn_3O_4 and the three nanocomposite samples ,MnrGO10, MnrGO30 and MnrGO50, recorded at a constant scan rate of 5 mV s^{-1} in the 0 to 1 V range are shown in figure 6 (A).

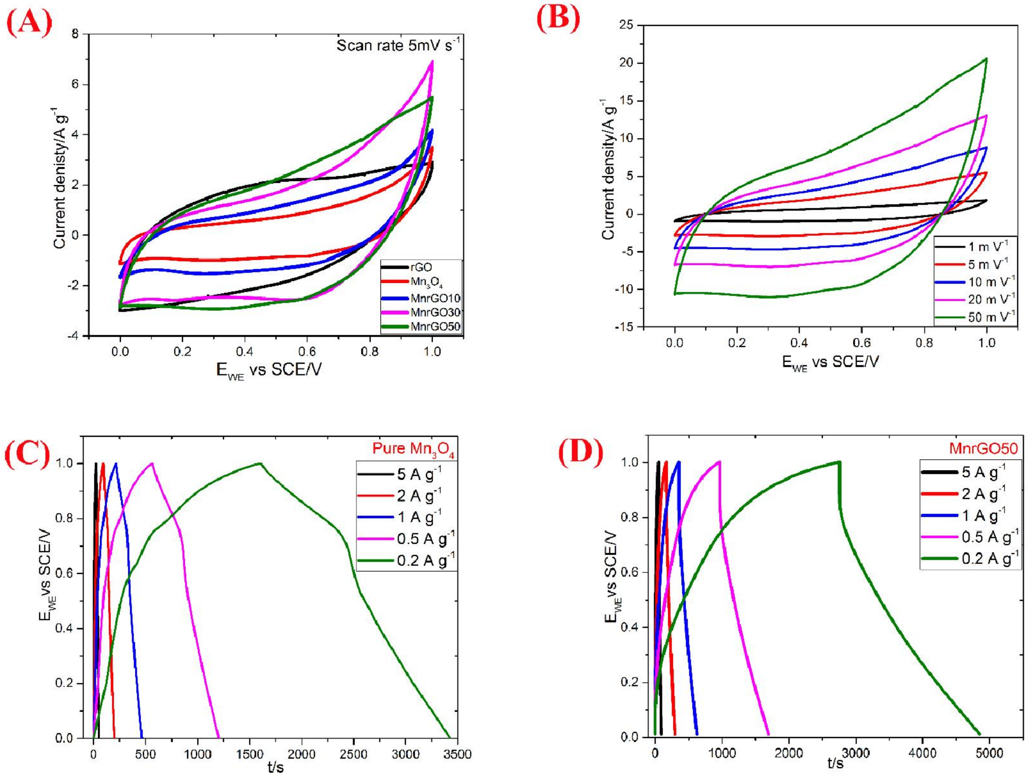

Figure 6: (A) The CV curves of all the samples at a scan rate of 5 mV s^{-1} (B)The CV curve of MnrGO50 at different scan rates (C) The GCD curve of Mn_3O_4 and (D) The GCD curve of MnrGO50 at different current densities.

The specific capacitance values of these electrode materials are given in Table 2. It is observed that the CV curve of pure Mn_3O_4 shows the pseudo-capacitance nature. By increasing the amount of rGO in Mn_3O_4/rGO composite, the pseudo-capacitance nature slowly disappears and a quasi-rectangular shape of the CV curve is observed for the MnrGO50 sample. The effective capacitance of the MnrGO50 is due to the double layer capacitance of rGO and the pseudo capacitance of the Mn_3O_4 nanorods. The specific capacitance value for each sample was estimated from the CV curve by integrating the area under the curve using origin lab software and then dividing by the sweep rate ϑ, the mass of the active material on the electrode m, and the potential window ΔV, according to the equation [41] given below,

$$C = \frac{1}{m\vartheta\Delta V}\int_{v_0}^{v_1} IVdV \quad \dots\dots\dots\dots (3) .$$

It is found that pure Mn_3O_4 shows a specific capacitance of 144 F g^{-1} and upon mixing with rGO, the capacitance value increases gradually. The electrical conductivity of the Mn_3O_4/rGO nanocomposite increases on increasing the rGO concentration in the composite. In the nanocomposite, charge transfer takes place from the highly conducting rGO layers of conductivity around 100 S/cm to the Mn_3O_4 nanorods, resulting in improved conductivity of the nanocomposite. This in turn facilitates better charge storage and ion transfer and enhances the capacitance as well [42].

Table 2

Specific capacitance at 5 m V s^{-1}

Sample	***Specific capacitance F g^{-1}***
Pure Mn_3O_4	144
rGO	198
MnrGO 10	212
MnrGO 30	366
MnrGO 50	406

Table 3

Specific capacitance of MnrGO50

Scan rate /m V s^{-1}	***Specific capacitance F g^{-1}***
1	451
5	406
10	326
20	242
50	152

The MnrGO50 electrode sample with maximum observed capacitance and quasi-rectangular shaped CV curve was further subjected to CV measurements at different scan rates. The CV curves of MnrGO50 sample at various scan rates are shown in figure 6(B). The specific capacitance values, calculated using equation 3 are shown in Table 3. It is observed that the increase of scan rate leads to a decrease in the specific capacitance, due to the electrode/electrolyte interface effects. At higher scan rates, the ions get intercalated only on the surfaces of the electrodes, whereas at lower scan rates, the ions can diffuse more into the inner active sites of the electrodes. Lower scan rates provide more time for ion diffusion and permit better intercalation of the ions within the active sites of the electrodes.

The galvanostatic charge–discharge (GCD) studies carried out on the electrode samples in the potential window from 0 to 1 V provide a complementary measurement of the capacitance. The charge–discharge profiles of Mn_3O_4 and MnrGO50 nanocomposite electrodes for the current density varying from 0.2A g^{-1} to 5A g^{-1} are shown in figures 6(C) and 6(D).

The charge discharge curve of Mn_3O_4 is not symmetrical. A potential drop is observed in the discharge curve due to the comparatively lower electronic conductivity of Mn_3O_4. For the MnrGO50 nanocomposite, the charge curve is almost symmetrical with its corresponding discharge counterpart, which is a true evidence of double layer capacitance contribution. There is a small internal resistance (IR) drop observed, which is specifically related to the pseudo-capacitive contribution. The specific capacitance is calculated using the equation given below,

$$C = \frac{i \text{ x } \Delta t}{m \text{ x } \Delta V} \ldots\ldots\ldots\ldots\ldots\ldots\ldots\ldots.(4)$$

where 'i' is the discharge current, 'Δt', the discharge time, 'm', the mass of the active material in the electrode and 'ΔV', the potential window.

Table 4

Comparison of the specific capacitance of the composites of Mn_3O_4 with various carbon nanostructures

Materials	**Specific capacitance F g^{-1}**	**Current density A g^{-1}**	**Electrolyte**	**Ref**
Porous Mn_3O_4	229	1	1M Na_2SO_4	[48]
Mn_3O_4 / carbon nanowires	132	1	1M Na_2SO_4	[49]
Mn_3O_4 nano ribbons / rGO	176	1	1M Na_2SO_4	[50]
Mn_3O_4 / RCDGO	187	1	1M Na_2SO_4	[23]
Mn_3O_4 / graphene	250	1	1M Na_2SO_4	[47]
Mn_3O_4 / rGO	121	0.5	1M Na_2SO_4	[44]
Mn_3O_4 / rGO	260	0.25	1M Na_2SO_4	[26]
Mn_3O_4 / rGO	270	0.5	1M Na_2SO_4	[51]
Mn_3O_4 / rGO	312	1	1M Na_2SO_4	Present work

The calculated specific capacitance values of pure Mn_3O_4 and MnrGO50 composite are shown in figure 7. The Mn_3O_4 sample gives a capacitance of 343 F g^{-1}, 301 F g^{-1}, 232 F g^{-1}, 198 F g^{-1} and 125 F g^{-1} for the current densities 0.2 A, 0.5 A, 1 A, 2 A and 5 A respectively. These values are comparable with the previously reported capacitance values of nanostructured Mn_3O_4 samples [43–45]. For the MnrGO50 composite sample, the capacitance values are 485 F g^{-1}, 424 F g^{-1}, 312 F g^{-1}, 295 F g^{-1} and 228 F g^{-1} for current densities of 0.2A, 0.5A, 1A, 2A and 5A respectively.

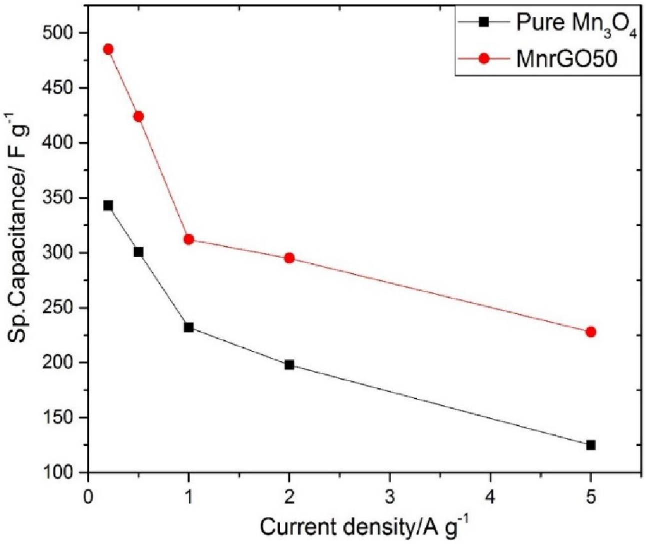

Figure 7: The GCD capacitance values of Mn_3O_4 and MnrGO50 at different current densities

These values are considerably higher than those of pure Mn_3O_4 sample and the results are in agreement with those obtained from the CV studies. The capacitance drop due to the internal resistance is very small in the MnrGO50 composite sample compared to that in pure Mn_3O_4 sample which results in the enhanced capacitance of the composite sample. A comparison of the specific capacitance of the composites of Mn_3O_4 with various carbon nanostructures is given in Table 4.The capacitance obtained for the MnrGO50 composite sample, in the present work, is higher than those in the previous reports on Mn_3O_4/rGO composites.[16,46,47] .

4.3.5.2 Two electrode studies

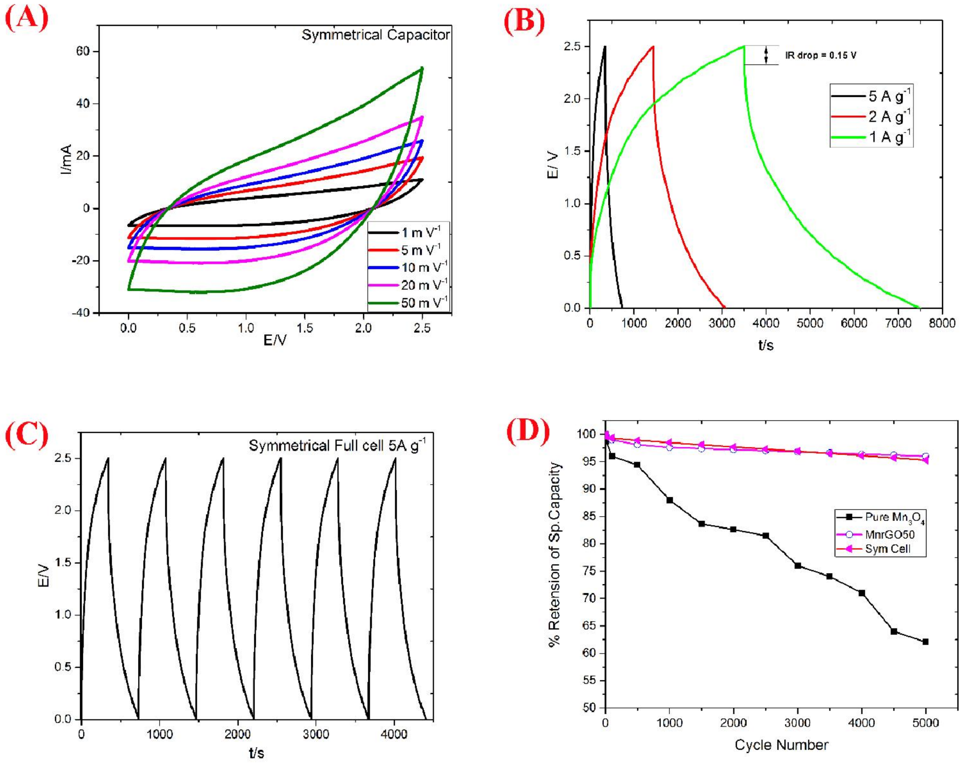

Figure 8: *(A) The CV Curves of MnrGO50 based super-capacitor at different scan rates (B) The GCD curves of MnrGO50 based super-capacitor at different current densities (C) The GCD curves of MnrGO50 based supercapacitor for 6 cycles (D) Capacitance retention (%) versus cycle number for Mn_3O_4 , MnrGO50 and the supercapacitor test cell.*

The three electrode studies of the active material provide the platform for assessing the suitability of the material for supercapacitor applications. The two electrode studies afford the supercapacitor performance at the device level for practical applications. Most of the reports on the electrochemical studies on

Mn_3O_4/rGO composites are limited to the three electrode studies. In the present work, symmetrical supercapacitor test cells using 14 mg of the active electrode material MnrGO50 were assembled with 1 M organic electrolyte and the capacitor level performance was analyzed using CV and GCD studies.

The CV and the GCD curves of the assembled symmetrical supercapacitor test cells at different scan rates in the potential window of 0 to 2.5 V are shown in figures 8A & 8B. The GCD curves of the test cell for six cycles are shown in figure 8(C). The symmetry of the charging and the discharging states of the assembled test cell is evident from these curves. The CV curves have quasi rectangular shape for all the scan rates used and redox peaks are not observed. This could be due to the dominance of the double layer behaviour of rGO compared to the faradic nature of Mn_3O_4. In the charge/discharge cycling (GCD) curve as well, no characteristic behaviour corresponding to redox reaction is observed. There are previous reports on the charge/discharge characteristics of the supercapacitors assembled using metal phosphates and oxides, and the curves are similar in shape to those in the present work. These supercapacitors are reported to show pseudocapacitive behaviour and the capacitance of the devices is expressed in farads [52–54]. In the case of the Mn_3O_4 / rGO based supercapacitor of the present work, the performance of the device can be approximated in terms of pseudocapacitive behaviour in the potential range of 0 to 2.5 V. The specific capacitance values obtained from the CV and the GCD studies are shown in Table 5.

The energy density and the power density are two important parameters that play key roles in determining the performance efficiency of a supercapacitor. These parameters are calculated using the equations 5 and 6 given below [16,24] and the values are shown in table 3:

$$Energy\ density\ E = \frac{1}{2*3.6}\ C * \Delta V^2 \qquad (5)$$

$$Power\ density\ P = \frac{E}{T} * 3600 \qquad (6)$$

where C is the specific capacitance, ΔV the potential window in volts and T the discharging time in seconds. The calculated energy density and power density values are comparable with those of the early reports on the supercapacitors based on Mn_3O_4 / carbon nanocomposites [16]. The energy density obtained is as high as 82 Wh Kg^{-1} at the current density of 1 A g^{-1} and a power density of 7097 W Kg^{-1} is observed at a current density of 5 A g^{-1}.

Table 5

The electrochemical parameters of the two electrode supercapacitor test cell

CV		**GCD**			
Scan rate mV s^{-1}	**Specific capacitance F g^{-1}**	**Current density A g^{-1}**	**Specific capacitance F g^{-1}**	**Energy density Wh Kg^{-1}**	**Power density W Kg^{-1}**
1	133	1	94	82	1032
5	108	***	***	***	***
10	96	2	88	77	2901
20	69	***	***	***	***
50	54	5	67	58	7097

The percentage retention of the specific capacitance of pure Mn_3O_4, MnrGO50 and the two electrode symmetrical supercapacitor test cell based on the MnrGO50 sample, for 5000 cycles is shown in figure 8(D). The Mn_3O_4 sample shows 60 % capacitance retention after 5000 cycles. For the MnrGO50 sample and the symmetrical supercapacitor test cell, the retention rate is above 95 % upon the completion of 5000 cycles.

4.4 Conclusions

In the present work, the Mn_3O_4/rGO nanocomposite is synthesized, using a simple physical mixing of the component materials. The Mn_3O_4 nanorods are obtained by the hydrothermal method in the presence of a surfactant and rGO by modified Hummer's method. The structural and the morphological characterization of the nanocomposite using XRD, Raman spectroscopy, FE-SEM, TEM and BET techniques confirms the formation of Mn_3O_4 nanorods and rGO flakes and the homogeneous dispersion of the nanorods within the rGO flakes. Electrodes made from the synthesized MnrGO50 nanocomposite sample, with the Mn_3O_4 and the rGO taken in 1:1 weight ratio exhibit excellent electrochemical performance. The electrochemical studies for the MnrGO50 nanocomposite electrode in the three electrode configuration, with 1 M Na_2SO_4 as the electrolyte, give specific capacitance of 228 F g^{-1} at a current density of 5 A g^{-1}. The two electrode studies conducted using symmetric supercapacitor test cells with the MnrGO50 nanocomposite as the electrode give a capacitance of 94 F g^{-1} and an energy density of 82 Wh kg^{-1} at a current density of 1 A g^{-1} and a power density of 7097 W kg^{-1} at a current density of 5 A g^{-1} with excellent cycling stability. It is observed that 95 % of the initial capacitance is retained after 5000 cycles at a current density of 5 A g^{-1}. The promising electrochemical behavior of the Mn_3O_4/rGO nanocomposite of the present work can be attributed to the controlled synthesis of the Mn_3O_4 nanorods and their homogenous dispersion within the rGO flakes, keeping the initial structural morphology of the Mn_3O_4 nanorods intact. The present synthesis method of the Mn_3O_4 nanorods, followed by the physical mixing with rGO, facilitating the homogenous dispersion of the Mn_3O_4 nanorods within the rGO flakes, is a novel and feasible approach towards the development of nanostructured hybrid electrode materials for designing high power supercapacitors.

4.5 References:

[1] A. Burke, Ultracapacitors: why, how, and where is the technology, J. Power Sources. 91 (2000) 37–50. doi:10.1016/S0378-7753(00)00485-7.

[2] M. Winter, R.J. Brodd, What Are Batteries, Fuel Cells, and Supercapacitors?, Chem. Rev. 104 (2004) 4245–4270. doi:10.1021/cr020730k.

[3] L.L. Zhang, X.S. Zhao, Carbon-based materials as supercapacitor electrodes, Chem. Soc. Rev. 38 (2009) 2520. doi:10.1039/b813846j.

[4] X. Zhao, B.M. Sánchez, P.J. Dobson, P.S. Grant, The role of nanomaterials in redox-based supercapacitors for next generation energy storage devices., Nanoscale. 3 (2011) 839–55. doi:10.1039/c0nr00594k.

[5] M. Pumera, Graphene-based nanomaterials for energy storage, Energy Environ. Sci. 4 (2011) 668–674. doi:10.1039/C0EE00295J.

[6] B.E. Conway, Transition from “Supercapacitor” to “Battery” Behavior in Electrochemical Energy Storage, J. Electrochem. Soc. 138 (1991) 1539. doi:10.1149/1.2085829.

[7] D. Wang, Y. Li, Q. Wang, T. Wang, Facile synthesis of porous Mn_3O_4 nanocrystal-graphene nanocomposites for electrochemical supercapacitors, Eur. J. Inorg. Chem. (2012) 628–635. doi:10.1002/ejic.201100983.

[8] V. Ibarra-Galván, C.I. Villavelázquez-Mendoza, E. Elorza Rodriguez, A. López-Valdivieso, S. Song Hu, R. Muñiz-Valencia, Synthesis of porous Mn_3O_4 microparticles by the $KMnO_4$ –AC reduction and combustion system, Part. Sci. Technol. 6351 (2016) 1–4. doi:10.1080/02726351.2016.1143069.

[9] S. Zhu, P. Zhang, L. Chang, Y. Zhong, K. Wang, H. Shao, J. Wang, J. Zhang, C. Cao, Photochemical fabrication of 3D hierarchical Mn_3O_4/H-TiO_2 composite films with excellent electrochemical capacitance performance, Royal Society of Chemistry, 2016. doi:10.1039/C6CP00372A.

[10] Y. Ma, L.B. Li, G.X. Gao, X.Y. Yang, Y. You, Effect of montmorillonite on the ionic conductivity and electrochemical properties of a composite solid polymer electrolyte based on polyvinylidenedifluoride/polyvinyl alcohol matrix for lithium ion batteries, Electrochim. Acta. 187 (2016) 535–542. doi:10.1016/j.electacta.2015.11.099.

[11] X. Du, C. Wang, M. Chen, Y. Jiao, J. Wang, Electrochemical Performances of Nanoparticle Fe_3O_4 /Activated Carbon Supercapacitor Using KOH Electrolyte Solution, J. Phys. Chem. C. 113 (2009) 2643–2646. doi:10.1021/jp8088269.

[12] J. Yan, Z. Fan, W. Sun, G. Ning, T. Wei, Q. Zhang, R. Zhang, L. Zhi, F. Wei, Advanced Asymmetric Supercapacitors Based

on $Ni(OH)_2$/Graphene and Porous Graphene Electrodes with High Energy Density, Adv. Funct. Mater. 22 (2012) 2632–2641. doi:10.1002/adfm.201102839.

[13] F. Yang, M. Zhao, Q. Sun, Y. Qiao, A novel hydrothermal synthesis and characterisation of porous Mn 3 O 4 for supercapacitors with high rate capability, RSC Adv. 5 (2015) 9843–9847. http://xlink.rsc.org/?DOI=C4RA10175H.

[14] C. Liu, H. Song, C.C. Zhang, Y. Liu, C.C. Zhang, X. Nan, G. Cao, Coherent Mn_3O_4-carbon nanocomposites with enhanced energy-storage capacitance, Nano Res. 8 (2015) 3372–3383. doi:10.1007/s12274-015-0837-4.

[15] C.-C. Hu, C.-Y. Hung, K.-H. Chang, Y.-L. Yang, A hierarchical nanostructure consisting of amorphous MnO_2, Mn_3O_4 nanocrystallites, and single-crystalline MnOOH nanowires for supercapacitors, 2011. doi:10.1016/j.jpowsour.2010.08.001.

[16] M. Mandal, D. Ghosh, K. Chattopadhyay, C.K. Das, A Novel Asymmetric Supercapacitor Designed with Mn_3O_4@Multi-wall Carbon Nanotube Nanocomposite and Reduced Graphene Oxide Electrodes, J. Electron. Mater. (2016). doi:10.1007/s11664-016-4493-6.

[17] K. Tanaka, S. (Shinji) Iijima, Carbon nanotubes and graphene, n.d. http://www.sciencedirect.com/science/book/9780080982328.

[18] C.N.R. Rao, A.K. Sood, K.S. Subrahmanyam, A. Govindaraj, Graphene: The new two-dimensional nanomaterial, Angew. Chemie - Int. Ed. 48 (2009) 7752–7777. doi:10.1002/anie.200901678.

[19] S. Wang, J. Yang, X. Wu, Y. Li, Z. Gong, W. Wen, M. Lin, J. Yang, Y. Yang, Toward high capacity and stable manganese-spinel electrode materials: A case study of Ti-substituted system, J. Power Sources. 245 (2014) 570–578. doi:10.1016/j.jpowsour.2013.07.021.

[20] W. Wang, T. Yang, G. Yan, H. Li, Synthesis of Mn_3O_4 hollow octahedrons and their possible growth mechanism, 2012. doi:10.1016/j.matlet.2012.05.070.

[21] B.G.S. Raj, R.N.R. Ramprasad, A.M. Asiri, J.J. Wu, S. Anandan, Ultrasound assisted synthesis of Mn_3O_4 nanoparticles anchored graphene nanosheets for supercapacitor applications, Electrochim. Acta. 156 (2015) 127–137. doi:10.1016/j.electacta.2015.01.052.

[22] D. Li, F. Meng, X. Yan, L. Yang, H. Heng, Y. Zhu, One-pot hydrothermal synthesis of Mn_3O_4 nanorods grown on Ni foam for high performance supercapacitor applications, Nanoscale Res. Lett. 8 (2013) 1–8. doi:10.1186/1556-276X-8-535.

[23] F. Gao, J. Qu, Z. Zhao, Q. Zhou, B. Li, J. Qiu, A green strategy for the synthesis of graphene supported Mn_3O_4 nanocomposites from graphitized coal and their supercapacitor application, Carbon N. Y. 80 (2014) 640–650. doi:10.1016/j.carbon.2014.09.008.

[24] Y. Xiao, Y. Cao, Y. Gong, A. Zhang, J. Zhao, S. Fang, D. Jia, F. Li, Electrolyte and composition effects on the performances of asymmetric supercapacitors constructed with Mn_3O_4 nanoparticles-graphene nanocomposites, J. Power Sources. 246 (2014) 926–933. doi:10.1016/j.jpowsour.2013.07.118.

[25] S. Yang, X. Song, P. Zhang, L. Gao, Crumpled nitrogen-doped graphene–ultrafine Mn_3O_4 nanohybrids and their application in supercapacitors, J. Mater. Chem. A. 1 (2013) 14162. doi:10.1039/c3ta12554h.

[26] X. Yang, Y. He, Y. Bai, J. Zhang, L. Kang, H. Xu, F. Shi, Z. Lei, Z.H. Liu, Mn3O4 nanocrystalline/graphene hybrid electrode with high capacitance, Electrochim. Acta. 188 (2016) 398–405. doi:10.1016/j.electacta.2015.12.024.

[27] D.C. Marcano, D. V. Kosynkin, J.M. Berlin, A. Sinitskii, Z. Sun, A. Slesarev, L.B. Alemany, W. Lu, J.M. Tour, Improved Synthesis of Graphene Oxide, ACS Nano. 4 (2010) 4806–4814.

doi:10.1021/nn1006368.

[28] N.A. Kumar, S. Gambarelli, F. Duclairoir, G. Bidan, L. Dubois, Synthesis of high quality reduced graphene oxide nanosheets free of paramagnetic metallic impurities, J. Mater. Chem. A. 1 (2013) 2789. doi:10.1039/c2ta01036d.

[29] H. Guo, X. Wang, Q. Qian, F. Wang, X. Xia, ARTICLE A Green Approach to the Synthesis of, ACS Nano. 3 (2009) 2653–2659. doi:10.1021/nn900227d.

[30] X. Hao, J. Zhao, Y. Li, Y. Zhao, D. Ma, L. Li, Mild aqueous synthesis of octahedral Mn3O4 nanocrystals with varied oxidation states, Colloids Surfaces A Physicochem. Eng. Asp. 374 (2011) 42–47. doi:10.1016/j.colsurfa.2010.10.048.

[31] D. Philip, Honey mediated green synthesis of gold nanoparticles., Spectrochim. Acta. A. Mol. Biomol. Spectrosc. 73 (2009) 650–3. doi:10.1016/j.saa.2009.03.007.

[32] C.M. Julien, M. Massot, C. Poinsignon, Lattice vibrations of manganese oxides. Part I. Periodic structures., Spectrochim. Acta. A. Mol. Biomol. Spectrosc. 60 (2004) 689–700. http://www.ncbi.nlm.nih.gov/pubmed/14747095 (accessed June 21, 2016).

[33] Y. Wang, Zhou, To draw an air electrode of a Li–air battery by pencil, Energy Environ. Sci. 4 (2011) 1704. doi:10.1039/c0ee00759e.

[34] Y. Zhou, Q. Bao, L.A.L. Tang, Y. Zhong, K.P. Loh, Hydrothermal Dehydration for the "Green" Reduction of Exfoliated Graphene Oxide to Graphene and Demonstration of Tunable Optical Limiting Properties, Chem. Mater. 21 (2009) 2950–2956. doi:10.1021/cm9006603.

[35] G. Jian, Y. Xu, L.-C. Lai, C. Wang, M.R. Zachariah, Mn_3O_4 hollow spheres for lithium-ion batteries with high rate and capacity, J. Mater. Chem. A. 2 (2014) 4627. doi:10.1039/c4ta00207e.

[36] S. Brunauer, P.H. Emmett, E. Teller, Adsorption of Gases in Multimolecular Layers, J. Am. Chem. Soc. 60 (1938) 309–319. doi:10.1021/ja01269a023.

[37] E.P. Barrett, L.G. Joyner, P.P. Halenda, The Determination of Pore Volume and Area Distributions in Porous Substances. I. Computations from Nitrogen Isotherms, J. Am. Chem. Soc. 73 (1951) 373–380. doi:10.1021/ja01145a126.

[38] P.R. Aravind, G.D. Soraru, Porous silicon oxycarbide glasses from hybrid ambigels, Microporous Mesoporous Mater. 142 (2011) 511–517. doi:10.1016/j.micromeso.2010.12.033.

[39] M.K. and, M. Jaroniec, Gas Adsorption Characterization of Ordered Organic−Inorganic Nanocomposite Materials, (2001). doi:10.1021/CM0101069.

[40] K.S.W. Sing, D.H. Everett, R.A.W. Haul, L. Moscou, R.A. Pierotti, J. Rouquerol, T. Siemieniewska, K.S.W. Sing, D.H. Everett, R.A.W. Haul, L. Moscou, R.A. Pierotti, J. Rouquerol, T. Siemieniewska, Reporting Physisorption Data for Gas/Solid Systems, in: Handb. Heterog. Catal., Wiley-VCH Verlag GmbH & Co. KGaA, Weinheim, Germany, 2008. doi:10.1002/9783527610044.hetcat0065.

[41] V. Srinivasan, J.W. Weidner, Studies on the Capacitance of Nickel Oxide Films: Effect of Heating Temperature and Electrolyte Concentration, J. Electrochem. Soc. 147 (2000) 880. doi:10.1149/1.1393286.

[42] L. Li, Z. Guo, A. Du, H. Liu, Rapid microwave-assisted synthesis of Mn_3O_4–graphene nanocomposite and its lithium storage properties, J. Mater. Chem. 22 (2012) 3600. doi:10.1039/c2jm15075a.

[43] N. Zhang, P. Qi, Y.-H. Ding, C.-J. Huang, J.-Y. Zhang, Y.-Z. Fang, A novel reduction synthesis of the graphene/Mn_3O_4 nanocomposite for supercapacitors, J. Solid State Chem. 237 (2016) 378–384. doi:10.1016/j.jssc.2016.02.049.

[44] J.W. Lee, A.S. Hall, J.-D. Kim, T.E. Mallouk, A Facile and Template-Free Hydrothermal Synthesis of Mn_3O_4 Nanorods on Graphene Sheets for Supercapacitor Electrodes with Long Cycle Stability, Chem. Mater. 24 (2012) 1158–1164. doi:10.1021/cm203697w.

[45] Y. Qiao, Q. Sun, H. Cui, D. Wang, F. Yang, X. Wang, Synthesis of micro/nano-structured Mn_3O_4 for supercapacitor electrode with excellent rate performance, RSC Adv. 5 (2015) 31942–31946. doi:10.1039/C5RA02395E.

[46] K. Zhao, K. Lyu, S. Liu, Q. Gan, Z. He, Z. Zhou, Ordered porous Mn_3O_4@N-doped carbon/graphene hybrids derived from metal–organic frameworks for supercapacitor electrodes, J. Mater. Sci. 52 (2017) 446–457. doi:10.1007/s10853-016-0344-3.

[47] Q. Jiangying, G. Feng, Z. Quan, W. Zhiyu, H. Han, L. Beibei, W. Wubo, W. Xuzhen, Jieshan, Highly atom-economic synthesis of graphene/Mn_3O_4 hybrid composites for electrochemical supercapacitors, Nanoscale. 5 (2013) 2999. doi:10.1039/c3nr33700f.

[48] F. Yang, M. Zhao, Q. Sun, Y. Qiao, A novel hydrothermal synthesis and characterisation of porous Mn_3O_4 for supercapacitors with high rate capability, RSC Adv. 5 (2015) 9843–9847. doi:10.1039/C4RA10175H.

[49] K. Wang, X. Ma, Z. Zhang, M. Zheng, Z. Geng, Z. Wang, Indirect Transformation of Coordination-Polymer Particles into Magnetic Carbon-Coated Mn_3O_4 (Mn_3O_4 @C) Nanowires for Supercapacitor Electrodes with Good Cycling Performance, Chem. - A Eur. J. 19 (2013) 7084–7089. doi:10.1002/chem.201300188.

[50] Y. Liu, W. Wang, Y. Wang, Y. Ying, L. Sun, X. Peng, Binder-free three-dimensional porous Mn_3O_4 nanorods/reduced graphene oxide paper-like electrodes for electrochemical energy storage, RSC Adv. 4 (2014) 16374–16379. doi:10.1039/C4RA01395F.

[51] L. Zhu, S. Zhang, Y. Cui, H. Song, X. Chen, One step synthesis and capacitive performance of graphene nanosheets/Mn_3O_4 composite, Electrochim. Acta. 89 (2013) 18–23. doi:10.1016/j.electacta.2012.10.157.

[52] J.H. Lee, J.A. Kim, J.-M. Kim, S.-Y. Lee, S.-H. Yeon, S.-Y. Lee, Beyond Slurry-Cast Supercapacitor Electrodes: PAN/MWNT Heteromat-Mediated Ultrahigh Capacitance Electrode Sheets, Sci. Rep. 7 (2017) 41708. doi:10.1038/srep41708.

[53] K. Raju, K.I. Ozoemena, Hierarchical One-Dimensional Ammonium Nickel Phosphate Microrods for High-Performance Pseudocapacitors, Nat. Publ. Gr. (2015) 1–13. doi:10.1038/srep17629.

[54] J. Ni, H. Wang, Y. Qu, L. Gao, PbO_2 electrodeposited on graphite for hybrid supercapacitor applications., Phys. Scr. 87 (2013) 045802, 4 . doi:10.1088/0031-8949/87/04/045802.

CHAPTER 5

Realizing Lithium Sulfur Cells Using Layered, Sulfur / Polymer Nano Composite Electrodes

Abstract:

Lithium-Sulfur (Li-S) cells are considered to be the potential candidates for the development of next generation energy storage devices owing to the impressive electrochemical properties of sulfur cathodes with high theoretical specific capacity of 1675 mAh g^{-1}. Lack of electronic conductivity of sulfur in the required range, large volume expansion of sulfur during lithium intake and the formation of soluble polysulfides during the cycling process are the main limitations of this technology. To address these challenges, in the present chapter, the composite of sulfur with the conducting polymer PEDOT: PSS, obtained using hydrothermal technique is tested as the cathode materials for Li-S cells.

Anilkumar K.M.,et al. Layered sulfur/PEDOT:PSS nano composite electrodes for lithium sulfur cell applications, Appl. Surf. Sci. 442 (2018) 556–564. doi:10.1016/j.apsusc.2018.02.178.

5.1 Introduction

Rechargeable batteries are being developed for portable power applications in mobile phones, laptops and medical implants and in electric vehicles and the present day research is being focused on identifying suitable materials to make the technology more efficient, economically viable and scalable for the reach of all sections of the society [1]. Lithium ion based cells are still dominating the scenario because of their high energy density in the range of 100 – 200 Wh kg^{-1} compared to the various other types of rechargeable cells [2]. At present, cathode materials based on transition metal oxides and olivine phosphates including $LiCoO_2$, $LiMn_2O_4$, and $LiFePO_4$ with specific capacity around 100-170 mAh g^{-1} are being extensively used in commercialized lithium ion cells [3,4]. These cathode materials have certain drawbacks mainly due to their weight and nearly single-electron reactions per mole, which limit the specific capacity to below 200 mAh g^{-1}.

To achieve the high energy density, high specific capacity and low production costs needed for the modern technology applications of Li cells, new materials with light weight and multi-electron reactions must be explored. Sulfur being non-toxic and light and with the added merit of having earth abundance has come up as a highly sought after electrode material which offers a high theoretical capacity of 1675 mAh g^{-1} and a high energy density of 2600 Wh kg^{-1} versus lithium, for developing the so called lithium sulfur (Li-S) cells [5,6].However, the commercialization of the Li-S cells is presently facing several challenges owing to the low sulfur utilization during cycling, the low columbic efficiency and the comparatively faster capacity fading [7]. These issues are mainly due to the very poor electrical conductivity of sulfur of the order of 10^{-30} S cm^{-1} , the shuttle effect of higher order soluble polysulfides and the large volumetric expansion of sulfur, around 80% during the lithiation on sulfur [8] .

The early research on the Li-S cells to overcome the above mentioned issues, was focused on carbon based materials to serve as a conducting as well as a buffering medium. Various carbon materials such as porous carbon, carbon black, carbon nanotubes, aerogel carbon, graphene, and hybrid carbon composites have been used as support materials for the sulfur cathode, generally using melt diffusion methods [9–11]. Such processes usually require thermal treatment at elevated temperatures to increase the electronic conductivity of the sulfur- carbon composite layer. The high temperature treatment is often not suitable for sulfur, because it generally results in considerable loss of sulfur in the composite [12].

Recently conductive polymer coated sulfur composites have received much attention as prospective cathode materials in Li-S cells. The presence of delocalized π electrons in the conducting polymer helps to enhance the electrical conductivity of the composite cathode material [13,14]. The electrochemical performance of these types of composites will be improved because of (a) the enhanced electrical conductivity, (b) the formation of a buffering matrix to prevent the agglomeration of sulfur and (c) the inhibition of the dissolution of polysulfides in the electrolyte as a consequence of the presence of the polymer coating. There are a number of reports on the sulfur composites based on conductive polymers like polypyrrole , polyaniline , polyacrylonitrile , polyimide and poly(3,4 –ethylenedioxy thiophene) (PEDOT) to serve as the cathode materials in Li-S cells [15,16].

The electrically conducting polymer PEDOT is generally mixed with the polymer ,polystyrenesulfonate (PSS) to improve the stability of the former and the PEDOT: PSS is a promising conducting polymer system to function as the buffer coating over sulfur, due to its environmental friendliness , good thermal stability and quite high electrical conductivity [17–19]. The PEDOT:PSS is found to retain its electrically conducting nature up to 450 K [20]. When sulfur is melted at temperatures around 380 K, the PEDOT: PSS coating remains intact without losing its high electrical conductivity. The PSS unit in PEDOT:PSS , dispersed in water is generally known to enhance the polymer solubility in aqueous media, which helps to form a homogeneous film or layer over sulfur in the composite, as compared to the PEDOT:PSS when used as itself [21].

Li and co-workers have [22] compared the electrochemical performance of different conducting polymer/sulfur composites and verified that long-term cycling stability and high discharge capacity are observed for PEDOT coated samples. Chen group [15] has reported an initial discharge capacity of

1117 mAh g^{-1} for S-PEDOT nanocomposite cathode prepared by membrane assisted precipitation technique. Yang group [16] has applied PEDOT based conducting polymer coating on mesoporous sulfur-carbon composite and reported a discharge capacity of 1140 mAh g^{-1} and a capacity retention of 85 % over 100 cycles. Lee group [23] has applied a wet mixing method (surface modification) on the commercially available sulfur to prepare S-PEDOT composite and reported an initial discharge capacity of 1100 mAh g^{-1}.

In the present work, we have synthesized sulfur/polymer composite by hydrothermal method using the commercial sulfur powder and the PEDOT:PSS conducting polymer to investigate the effect of having the conducting polymer buffer layer, without carbon support on sulfur electrodes. The advantage of hydrothermal method is that the sulfur/conducting polymer composite can be synthesized at low temperatures around 120 °C in a short time span with sulfur being homogeneously distributed in between the polymer layers after the treatment. The resulting, layered sulfur/polymer nanocomposite can be considered as a potential cathode material for lithium–sulfur cells with impressive electrochemical characteristics and the advantages of low energy consumption and short period of synthesis, maintaining the required sulfur content in the final composite [12].

The sulfur/polymer composite cathodes are evaluated on the basis of various electrochemical parameters such as capacity, rate capability and cycling stability to establish the application prospects of these composite cathode materials in the design of high energy density Li-S cells.

5.2 Experimental details

Conductive grade, poly (3,4-ethylenedioxythiophene)-poly (styrenesulfonate), 1.3 wt % dispersion in H_2O, (PEDOT:PSS), dimethyl sulfoxide, ACS reagent, ≥99.9% purity (DMSO) and sulfur were purchased from Sigma-Aldrich(India) and were used as received.

Three samples with sulfur/PEDOT: PSS ratios of 90:10, 80:20 and 70:30 were synthesized using hydrothermal approach. In a typical synthesis, 10 wt % of PEDOT: PSS was added to 5 ml of dimethyl sulfoxide (DMSO) and left stirring for 4 hours. In a separate beaker, finely powdered sulfur was dispersed in 5 ml of DMSO by stirring for 2 hours. The as prepared PEDOT: PSS in DMSO was then added drop wise to the sulfur dispersion in DMSO and the stirring was continued for another 6 hours. The resulting mixture was transferred to a teflon lined auto clave and kept at a temperature of 120 ºC for 6 hours. The auto clave was allowed to cool to room temperature after the hydrothermal treatment. The resultant product was subjected to washing several times using deionized water to remove the residual DMSO. The product obtained after washing was dried at 60 ºC under vacuum overnight to get the final sulfur/polymer composite sample. The sulfur/polymer composite has a greenish appearance and is labelled as PS1. The synthesis procedure is represented in figure 1. The above synthesis approach was repeated for compositions with 20 wt% and 30 wt% of PEDOT: PSS and the samples obtained are named as PS2 and PS3 respectively.

The structural aspects of these samples were studied using XRD technique, employing PANAlytical X'Pert PRO machine with Cu-K_α radiation of wavelength 1.54 Å. The Raman studies were carried out using Horiba LabRam (800 nm) HR spectrometer equipped with a 514 nm Argon ion laser of 15 mW power. The morphological aspects of the samples were investigated using Nova Nanosem 450, field emission scanning electron microscope. The high resolution TEM images of the samples were obtained using Jeol/JEM 2100 machine of the Sophisticated Analytical Instrument Facility (SAIF) at CUSAT, Kochi, India.

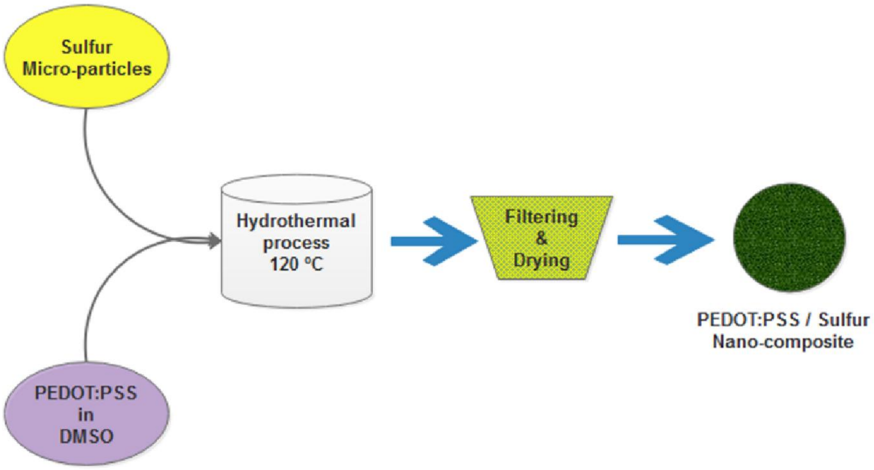

Figure 1: Schematic representation of the synthesis of the sulfur / PEDOT:PSS nano-composite.

The working electrodes for the electrochemical characterisations were prepared by mixing 80 wt% of sulfur/PEDOT:PSS active material with 10 wt%

of carbon black as conducting medium and 10 wt% of polyvinylidene difluoride (PVDF) as binder in the presence of N-methyl pyrrolidinone (NMP) solvent. The homogeneous slurry obtained was coated on a thin aluminum foil by spray coating and was allowed to dry at 60 °C under vacuum overnight. Circular discs of 16 mm diameter were cut from the coating and used as active cathode electrodes. Electrochemical characterisations were carried out by assembling 2032 type coin cells with 1 M $LiClO_4$ in 1,2-dimethoxymethane (DME)/1,3-dioxolane (DOL) (1 : 1 v/v) with 0.5 M $LiNO_3$ as the electrolyte and lithium chip as the anode [24].

The cells were assembled in an argon filled glove box. The assembled cells were subjected to charge-discharge cycling at current rates of 0.1 C, 0.2 C, 0.5 C and 1 C (The C rate was calculated, taking the theoretical capacity of sulfur with respect to lithium as 1650 mAh g^{-1}) within the potential window of 1.5-3 V using the 8 Channel Battery Analyser (MTI Corporation-USA). The specific capacity calculations were done with respect to the active sulfur content in the electrodes*. The cells were also subjected to cyclic voltammetry (CV) analysis within 1.5-3 V at a scanning rate of 0.1 mV s^{-1}. The Electrochemical impedance spectroscopic (EIS) studies of the cells were carried out from 1 MHz to 10 mHz at the open cell voltage of the cells. The CV and the EIS studies were carried out using the Bio-Logic SP300 unit.

***Appendix B**-*TGA Curves of PS1, PS2, and PS3 composite samples.*

5.3 Results and discussion

5.3.1 The XRD analysis

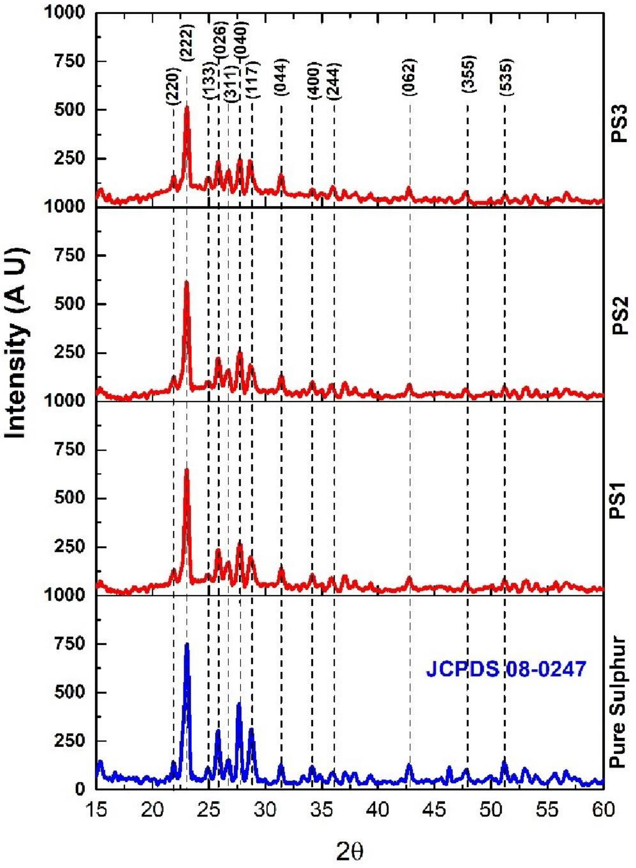

Figure 2: XRD patterns of pure sulfur and PS1, PS2, PS3

The XRD patterns of pure sulfur and sulfur/polymer composite samples are shown in figure 2. Characteristics peaks of the orthorhombic Fddd phase of sulfur can be observed in the XRD patterns of all the samples studied , which fit the JCPDS no. 08-0247 without any impurity phase. The peaks corresponding to PEDOT: PSS polymer are not seen in the XRD patterns owing to its amorphous nature. [23] . A decrease in the intensity of sulfur diffraction peaks is observed with the increase in PEDOT:PSS concentration, which is due to the formation of the polymer covering layer over the sulfur particles and the intensity is found to be minimum for the PS3 sample with maximum PEDOT:PSS concentration. [25]. The XRD patterns of pure sulfur and sulfur/polymer composites confirm the formation of an active polymer layer over the sulfur particles without any chemical reaction, as the structural features of pure sulfur are found to be retained in the final composite.

5.3.2 Raman spectroscopic studies

The Raman spectra of the PS1, PS2 and PS3 composite samples are presented in figures 3A and 3B. The characteristic peaks of elemental sulfur and those of polymer are present in all the studied compositions. The spectra shown in Figure 3A between the range 50-2000 cm^{-1} have three sharp peaks centred at 153, 220 and 476 cm^{-1} respectively, which are the signature peaks of elemental orthorhombic sulfur [26] . The peaks of PEDOT: PSS are not visible in figure 3A.This is either due to the very high intensity of the sulfur peaks or because the resulting coating of the PEDOT: PSS over sulfur is very thin. A separate scan carried out exclusively in the range of 1000-2000 cm^{-1} is shown in figure 3B, which clearly gives the characteristic peaks of PEDOT: PSS. The band located at 1264 cm^{-1} is attributed to the stretching vibrations of CR-CR′, where R and R’ denote alkyl groups [27]. The strong peak at 1442 cm^{-1} is due to the C–C stretching vibration of the thiophene ring, originating from the neutral parts existing between the localized elementary excitations such as positive polarons or bipolarons generated upon doping . The peaks centered at 1498 cm^{-1} and 1570 cm^{-1} are assigned to the C=C asymmetric stretching vibrations of the thiophene rings in the middle and at the end of the chains, respectively [28]. The appearance of the peaks corresponding to pure PEDOT: PSS in the sulfur/polymer composites indicates the existence of PEDOT: PSS without any structural changes in the composite samples.

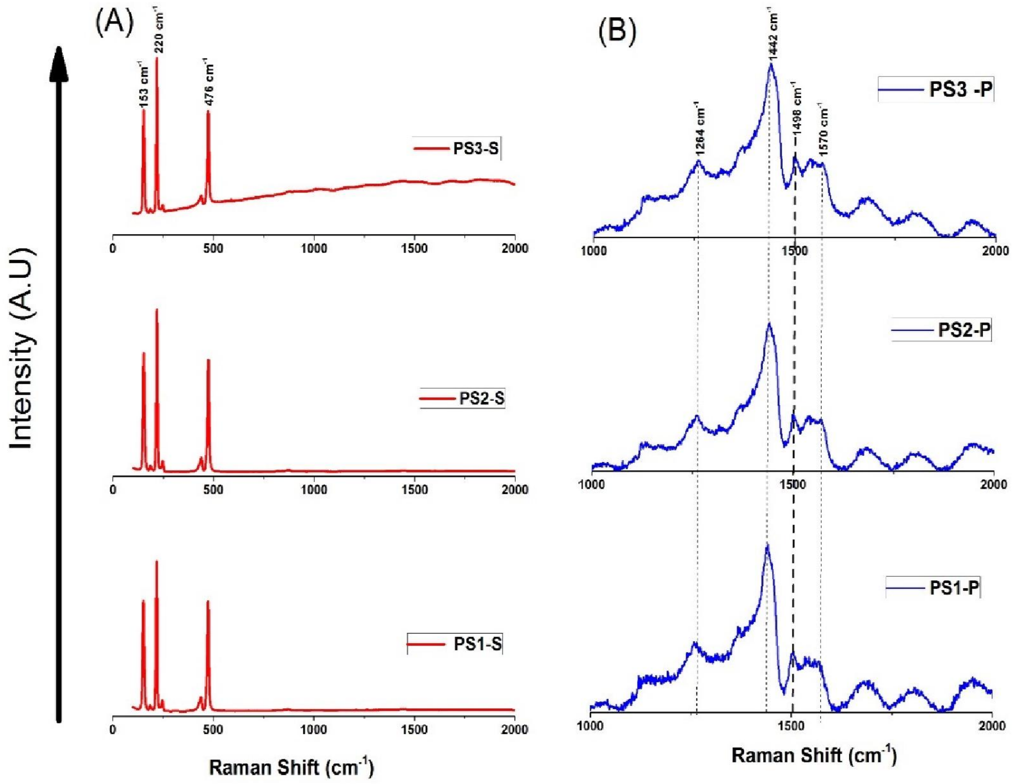

Figure 3: Raman spectra of the PS1, PS2, PS3 samples scanned in the range (A) 50-2000 cm^{-1} (B) 1000-2000 cm^{-1}

The formation of the sulfur/polymer composites with the retention of the individual polymer-sulfur structural features further supports the assumption that the polymer coating process over the sulfur particles in the composite takes place without any possible chemical reaction between the polymer and the active sulfur.

5.3.3 The FESEM and TEM analysis

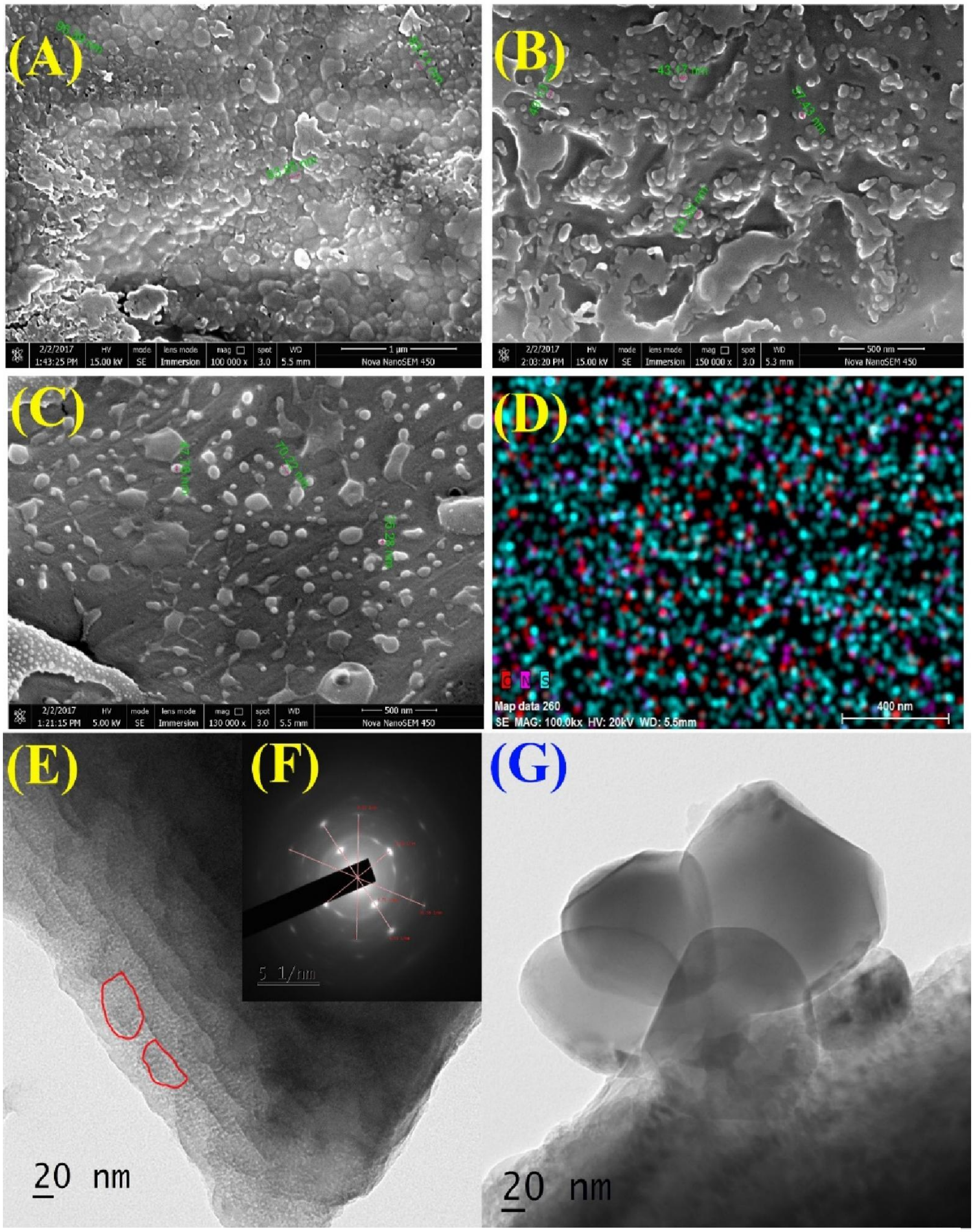

Figure 4: FESEM micrographs of (A) PS1 (B) PS2 (C) PS3 samples, (D) Elemental mapping of PS1 sample, (E) and (G) TEM images of PS1 sample and (F) SAED pattern of PS1 sample.

The FESEM images of the studied sulfur/polymer composites are presented in figure 4, with the figures 4A, 4B and 4C representing individual micrographs of the PS1, PS2 and PS3 compositions respectively. In all the studied compositions, the polymer PEDOT: PSS is expected to form a covering layer over the sulfur particles during the hydrothermal process. The FESEM images support the proposed structure of the composites, with the nano sized sulfur embedded within the polymer layers. Increase in the concentration of the polymer in the composite leads to the formation of a thick polymer coating over sulfur nanoparticles, which results in partial masking of the active sulfur within the polymer layer. In the case of the PS1 composition, a thin layer of polymer is coated over the sulfur particles and the active sulfur is readily visible on the surface of the composite as evidenced from figure 4A. In the images of PS2 and PS3 samples with increased polymer content, sulfur is found to be concealed in between thicker polymer layers with a fewer fraction available on the surface of the composite.

The PS1 sample, with 90 % sulfur content is further subjected to an elemental mapping analysis in order to understand more about the distribution of active sulfur within the polymer layer. In the PS1 sample, active sulfur is seen to be widely distributed all over the composite with the polymer forming only a thin covering layer. Elemental mapping of C, N and S contents in the PS1 composite is shown in figure 4D. The mapping confirms the homogeneous distribution of C, N and S elements over the surface of the sulfur/polymer composite. The presence of C and N is mainly due to the presence of these elements in the polymer back bone of PEDOT: PSS. Elemental mapping with spots representing sulfur spots surrounded by those of C and N, supports the formation of a thin polymer layer over the sulfur particles in the final composite

The TEM image of PS1 composite is shown in figure 4E, which illustrates the presence of nano sized sulfur particles packed in between thin polymer layers. Sulfur, during the hydrothermal treatment melts and diffuses into the polymer. After the hydrothermal process, polymer forms a thin covering over the sulfur particles, with the sulfur being finely distributed in between the thin polymer layers. The inset in figure 3E, titled as 3F shows the SAED pattern of the PS1 composite with the diffused spots representing the nano sized sulfur particles and the bright circles representing the amorphous polymer content. The packing of sulfur particles in between the polymer layers is further evidenced from figure 4G with the sulfur particles leaking out from the polymer layer. The sulfur particles have nearly spherical shape with particle size in the range of 50-100 nm. No large agglomerates have been observed in the FESEM/TEM investigations. The FESEM images with elemental mapping, the TEM images and the SAED pattern clearly confirm the formation of the sulfur/polymer nano composite with the polymer serving as a covering layer over the sulfur particles.

5.3.4 Electrochemical studies

5.3.4.1 Cyclic voltammetric and impedance spectroscopic analysis

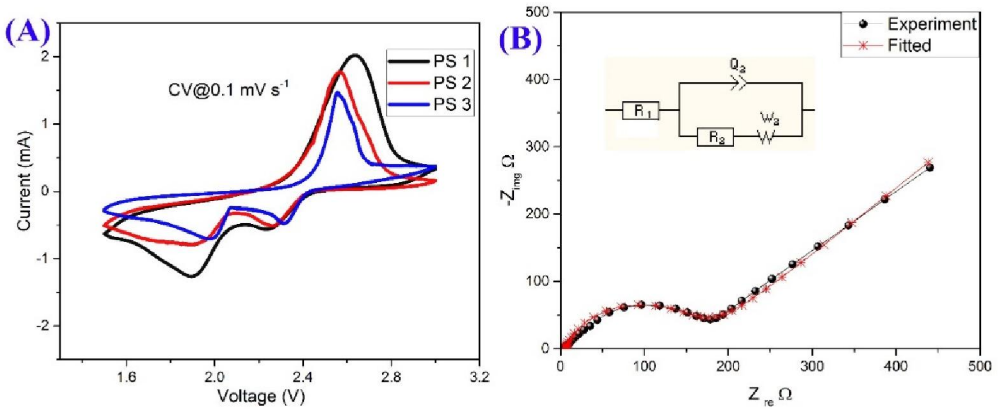

Figure 5: (A) The CV curves of the Li-S cells based on the PS1, PS2 and PS3 samples at a scan rate of 0.1 mV s^{-1} (B) Nyquist plot of the PS1 sample.

The cyclic voltammetric curves of the lithium sulfur cells based on the PS1, PS2 and PS3 samples, at a scan rate of 0.1mV s^{-1} between the voltage range 3 V to 1.5 V are shown in figure 5(A). During the first cycle, two broad reduction peaks at ~2.25 V and ~1.95 V are observed [7]. These two peaks correspond to the reduction of elemental sulfur to the soluble lithium polysulfides (Li_2S_n, 4<n≤8) and the subsequent formation of the insoluble Li_2S and Li_2S_2. . The strong and broad oxidation peak observed at ~2.62 V is due to the conversion of the polysulfides to elemental sulfur [14].

For the PS2 and PS3 based cells , a small shift in the reduction peaks is observed with respect to that for the PS1 based cell, but the intensity of the peaks is less compared to that of the latter. A small shift is also observed in the oxidation peaks of the PS2 and PS3 cells compared to that of the PS1 cell. For the PS1 test cell the oxidation peak at 2.62 V and the reduction peaks at 2.25V and 1.95V are all quite broad compared to those for the PS2 and PS3 test cells. This indicates that upon lithiation, the conversion from the soluble polysulfides to the insoluble forms Li_2S or Li_2S_2 takes place more effectively and to a higher extent in the PS1 based cell compared to the other two cells. Hence for the PS1 cell, the possibility of dissolution of sulfur in the electrolyte, leading to the loss of sulfur can be minimized to a higher degree, compared to the other two cells. Upon delithiation, the conversion of the insoluble polysulfides to elemental sulfur takes place more efficiently for the PS1 cell owing to the broad nature of the oxidation peak at 2.62 V. The CV results conclusively establish that for the PS1 cell, the transition between S_8 and lithium sulfides (Li_2S_2 or Li_2S) and vice versa takes place more efficiently, compared to the other two cells [29] The clear, broad and overlapped CV peaks in the PS1 test cell indicate its excellent electrochemical capability [16].

The electrochemical impedance spectroscopy (EIS) studies were carried out for the PS1 based lithium sulfur cell and the corresponding Nyquist plot is shown in figure 5(B). The measured data was fitted with the help of EC-Lab software and the equivalent circuit used is shown in the inset of figure 5(B). The impedance spectrum in figure 5(B) is composed of one depressed semicircle in the medium-frequency region which represents the charge transfer resistance of the interface between the sulfur electrode and electrolyte, and the inclined line (Warburg impedance) in the low frequency region corresponding to semi-infinite diffusion. In the equivalent circuit shown as inset in figure 5(B), R1 is the resistance of the electrolyte, R2 the charge transfer resistance, Q1 the constant phase element, and W the Warburg diffusion impedance of the electrode. [30,31]. It is observed that for the cell based on the PS1 sample, the charge transfer resistance is very low mainly due to the presence of the polymer PEDOT: PSS layer over sulfur, which enhances the overall electrical conductivity of the PS1 electrode. This effect, in turn, provides improvement in the electrochemical performance with better reversible capacity in the Li-S cells.

5.3.4.2 Charge-Discharge studies

The charge discharge profiles of the PS1, PS2 and PS3 based Li-S cells at 0.1 C rate are shown in Figures 6 A and 6 B .The performance data including the values of capacity and efficiency are given in table 1. For the first cycle, the initial discharge and charge capacities of the PS1based cell are 1301 mAh g^{-1} and 1190 mAh g^{-1} respectively with a columbic efficiency of 91 %. For the PS2 cell, the discharge and charge capacities are found to be 1132 mAh g^{-1} and 985 mAh g^{-1} respectively with 87 % efficiency and for the PS3 based cell, the values are 740 mAh g^{-1} and 620 mAh g^{-1} respectively with an efficiency of 83 %. The PS1 based cell shows two characteristic plateaus during the discharge process in the first cycle, one at 2.25 V and the other at 2.0 V. The short plateau at 2.25 V corresponds to the formation of soluble higher order lithium polysulfides, and the longer one which is observed at 2.0 V is related to the formation of insoluble lower order lithium polysulfides such as Li_2S_2, and Li_2S from S_8 during the initial lithiation process within the Li-S cell.

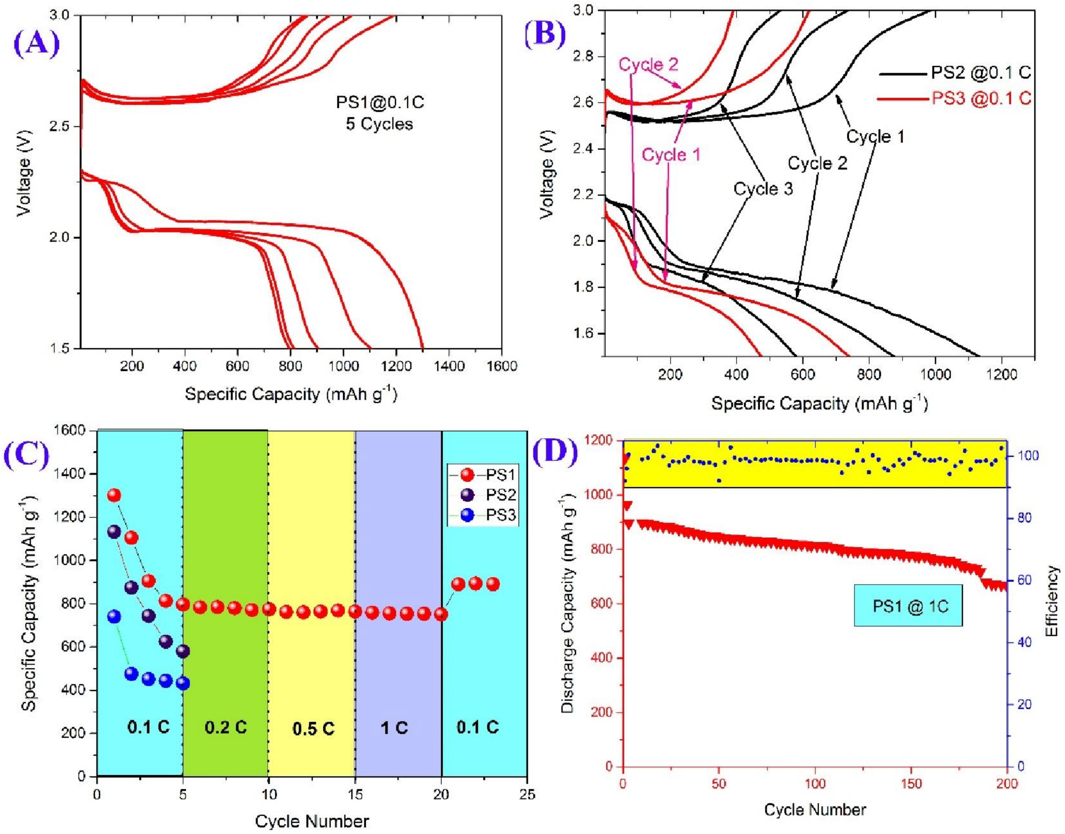

Figure 6: Charge discharge curves of the Li-S cells based on (A) PS1 (B) PS2 and PS3 samples (C) Rate capability data of the PS1, PS2 and PS3 based Li-S cells (D) Cycle life performance of the PS1 based cell.

During the second charge/discharge cycle, the PS1 based cell shows a higher columbic efficiency compared to the first cycle, mainly due to a decrease in the formation of higher order polysulfides as clear from the charge-discharge profile. The discharge and charge capacities of 1104 mAh g^{-1} and 1031 mAh g^{-1}, respectively are observed for the second cycle. The second cycle discharge capacity is around 85 % of the initial capacity. For the PS2 based cell, the second cycle discharge and charge capacities are found to decrease to 874 mAh g^{-1} and 735 mAh g^{-1} respectively and for the PS3 based cell these values are 476 mAh g^{-1} and 390 mAh g^{-1} respectively. These capacities are 77 % and 64 % of the respective first cycle discharge capacities. During the 3rd, 4th and 5th cycles, the discharge capacities of the PS1 based cell are 905 mAh g^{-1}, 813 mAh g^{-1} and 796 mAh g^{-1} respectively. The capacity attains a stable behaviour during the 4th and 5th cycles.

Table 1: ***Specific capacity and efficiency data of the PS1,PS2 and PS3 based cells***

Cells	**1st**			**3rd**	**5th**
	Discharge (mAh g^{-1})	**Charge (mAh g^{-1})**	**Efficiency (%)**	**Discharge (mAh g^{-1})**	**Discharge (mAh g^{-1})**
PS1	1301	1190	91	905	796
PS2	1132	985	87	744	580
PS3	740	620	83	451	432

For the PS2 and PS3 based cells, the retention of capacity is poor irrespective of having a thicker polymer coating, compared to the PS1 based cell. The stable capacities of the PS1 based cell may be attributed to the presence of the thin layer of polymer coating as observed in the FESEM and TEM micrographs. The polymer coating acts as a buffering medium to control the morphological changes like volume expansion, happening during the initial cycling process, in addition to helping in enhancing the overall electrical conductivity of the composite electrode. In the case of the PS2 and PS3 based test cells, the thicker polymer coating hinders the easier diffusion of lithium ions to the active sulfur sites. [15]. For these two cells, the main lithiation plateau around 2.0 V gradually decreases in size with cycling, resulting in capacity fading during the charge/discharge process.

The results of the rate capability studies of the PS1, PS2 and PS3 based Li-S cells are presented in figure 6C. Cells based on the PS1 electrodes exhibit much higher capacities compared to the PS2 and PS3 based cells when cycled at a current rate of 0.1 C. Capacities are found to be fading during initial cycling and stability is attained after 4 cycles of continuous charging/discharging. For the PS2 and PS3 based cells, the 5th cycle capacities go down to 580 mAh g^{-1} and 432 mAh g^{-1}, respectively, much less than their initial capacities. The PS1 based cell is found to deliver a capacity of 796 mAh g^{-1} at the end of the 5th cycle, with a capacity retention of ~60 % with respect to the first cycle discharge capacity.

The cell based on the PS1 electrode was further subjected to cycling at higher current rates for the rate capability studies. The cell exhibits a stable behaviour from the 5th cycle onwards up to the 20th cycle, with retention of more or less the same capacity. The cell is also found to retain a capacity of ~751 mAh g^{-1} at a rate of 1 C after 20 continuous charge/discharge cycling. The improved capacity values of the PS1 based cells could be due to the formation of an efficient polymer coating on the nano sized sulfur with sulfur particles packed in between the polymer layers. The coating helps to prevent the dissolution of the polysulfides into the electrolyte, enhances the electrical conductivity of the composite electrode and also acts as a buffer layer to control the volume expansion of sulfur during high lithium intake. The cell is found to recover the initial capacity of ~850 mAh g^{-1} when cycled at a rate of ~ 0.1 C, after multiple electrochemical cycling at higher current rates. This retention of the initial capacity indicates the stability of the electrodes with resistance to any sort of exfoliation during the continuous cycling at different current rates. The cells based on the PS1 electrode were also subjected to cycling for 200 cycles at a constant current rate of 1C. The cycling performance and the columbic efficiency values of the PS1 based cell at 1 C rate for 200 cycles are shown in figure 6D. The cell has an initial discharge capacity of 1136 mAh g^{-1} with 92 % columbic efficiency. The capacity attains a stable value of around 897 mAh g^{-1} with 98 % efficiency at the end of the 3rd cycle. A discharge capacity of 664 mAh g^{-1} is found to be retained at the end of the 200th cycle with a retention of ~75 % with respect to the initial stable capacity.

The improved electrochemical performance of the sulfur/polymer composite electrodes can be correlated with the formation of a thin polymer layer around the sulfur particles, which acts as a buffering layer to overcome the limitations of the sulfur cathodes. One of the prime factors promoting the improved electro-chemical performance is the reduced particle size of the sulfur/polymer composite electrode to the nanometer scale, attained by the PEDOT: PSS assisted hydrothermal method of synthesis. This helps to have better contact for the sulfur nanoparticles with the conducting polymer layer, which facilitates better and easier electron transport across the electrodes and in turn enhances the utilization of sulfur. The conducting PEDOT: PSS encapsulation provides better electrical contact and limits the dissolution of the lithium polysulfide ions and the shuttling effect during cycling. In addition, the polymer matrix can prevent the aggregation of sulfur particles. Lastly, the PEDOT: PSS shells can also withstand the volume changes during the charge/discharge cycles.

5.4 Conclusions

The sulfur / PEDOT: PSS composites with different weight ratios of the component materials were synthesized by hydrothermal method. From the XRD and Raman spectroscopic analysis the structural integrity of sulfur and PEDOT: PSS in the sulfur/polymer composites, after the hydrothermal process can be established. The morphological studies using FESEM and TEM techniques confirm the formation of a thin polymer coating over the sulfur particles, with sulfur being finely distributed in between the polymer layers. The presence of the conducting polymer coating over the sulfur particles enhances the overall electrical conductivity of the composite electrode. The polymer coating helps to minimize the volume changes of sulfur due to lithium insertion during the charge/discharge cycles .The electro-chemical studies show that the cells assembled with the sulfur/PEDOT: PSS composite synthesized in 9:1 weight ratio of sulfur and PEDOT: PSS (PS1) respectively as electrode , offer quite impressive electrochemical behaviour with an initial discharge capacity of 1301 mAh g^{-1} at 0.1 C rate and a columbic efficiency of 91 %. The PS1 based cell retains 75 % of the initial stable capacity of 897 mAh g^{-1} after 200 cycles at a rate of 1 C. The electro-chemical investigations convincingly establish the excellent application prospects of the sulfur/ PEDOT: PSS nanocomposite to be used as the cathode material for developing high energy density, next generation Li-S cells

5.5 References

[1] Y.X. Yin, S. Xin, Y.G. Guo, L.J. Wan, Lithium-sulfur batteries: Electrochemistry, materials, and prospects, Angew. Chemie - Int. Ed. 52 (2013) 13186–13200. doi:10.1002/anie.201304762.

[2] G. Griffiths, Review of developments in lithium secondary battery technology, Underw. Technol. 33 (2016) 153–163. doi:10.3723/ut.33.153.

[3] G. Li, Z. Li, B. Zhang, Z. Lin, Developments of electrolyte systems for lithium–sulfur batteries: a review, Energy Storage. 3 (2015) 5. doi:10.3389/fenrg.2015.00005.

[4] L. Yu, D. Cai, H. Wang, M.-M. Titirici, Synthesis of Microspherical $LiFePO_4$-Carbon Composites for Lithium-Ion Batteries, Nanomaterials. 3 (2013) 443–452. doi:10.3390/nano3030443.

[5] Q. Pang, X. Liang, C.Y. Kwok, L.F. Nazar, Advances in lithium–sulfur batteries based on multifunctional cathodes and electrolytes, Nat. Energy. 1 (2016) 16132. doi:10.1038/nenergy.2016.132.

[6] A. Manthiram, Y. Fu, Y.-S. Su, Challenges and Prospects of Lithium–Sulfur Batteries, Acc. Chem. Res. 46 (2013) 1125–1134. doi:10.1021/ar300179v.

[7] J.E.S. Technol, X. Zhao, G. Cheruvally, C. Kim, K. Cho, H. Ahn, K. Kim, J. Ahn, Lithium / Sulfur Secondary Batteries : A Review, 7 (2016) 97–114.

[8] K.R. Kim, K.-S. Lee, C.-Y. Ahn, S.-H. Yu, Y.-E. Sung, Discharging a Li-S battery with ultra-high sulphur content cathode using a redox mediator, Sci. Rep. 6 (2016) 32433. doi:10.1038/srep32433.

[9] Y.S. Su, Y. Fu, T. Cochell, a Manthiram, A strategic approach to recharging lithium-sulphur batteries for long cycle life, Nat Commun. 4 (2013) 2985. doi:10.1038/ncomms3985.

[10] J. Wu, J. Hu, K. Song, J. Xu, H. Gao, Spirulina-derived nitrogen-doped porous carbon as carbon/S composite cathodes for high cyclability lithium-sulphur batteries, J. Alloys Compd. 704 (2017) 1–6. doi:10.1016/j.jallcom.2017.02.052.

[11] D. Bresser, S. Passerini, B. Scrosati, Recent progress and remaining challenges in sulfur-based lithium secondary batteries – a review, Chem. Commun. 49 (2013) 10545. doi:10.1039/c3cc46131a.

[12] Y. Chen, H. Zhang, X. Yang, K. Feng, X. Li, H. Zhang, A novel facile and fast hydrothermal-assisted method to synthesize sulfur/carbon composites for high-performance lithium–sulfur batteries, RSC Adv. 6 (2016) 81950–81957. doi:10.1039/C6RA19613F.

[13] X. Zhu, Z. Wen, Z. Gu, Z. Lin, Electrochemical characterization and performance improvement of lithium/sulfur polymer batteries, J. Power Sources. 139 (2005) 269–273. doi:10.1016/j.jpowsour.2004.07.002.

[14] B.H. Jeon, J.H. Yeon, K.M. Kim, I.J. Chung, Preparation and electrochemical properties of lithium-sulfur polymer batteries, J. Power Sources. 109 (2002) 89–97. doi:10.1016/S0378-7753(02)00050-2.

[15] H. Chen, W. Dong, J. Ge, C. Wang, X. Wu, Ultrafine Sulfur Nanoparticles in Conducting Polymer Shell as Cathode Materials for High Performance Lithium/Sulfur Batteries, Sci. Rep. 3 (2013) 1910.

doi:10.1038/srep01910.

[16] Y. Yang, G. Yu, J.J. Cha, H. Wu, M. Vosgueritchian, Y. Yao, Z. Bao, Y. Cui, Improving the performance of lithium-sulfur batteries by conductive polymer coating, ACS Nano. 5 (2011) 9187–9193. doi:10.1021/nn203436j.

[17] T. Ji, L. Tan, X. Hu, Y. Dai, Y. Chen, A comprehensive study of sulfonated carbon materials as conductive composites for polymer solar cells, Phys. Chem. Chem. Phys. 17 (2015) 4137–4145. doi:10.1039/C4CP04965A.

[18] T.-R. Chou, S.-H. Chen, Y.-T. Chiang, Y.-T. Lin, C.-Y. Chao, Highly conductive PEDOT:PSS films by post-treatment with dimethyl sulfoxide for ITO-free liquid crystal display, J. Mater. Chem. C. 3 (2015) 3760–3766. doi:10.1039/C5TC00276A.

[19] E. Vitoratos, S. Sakkopoulos, E. Dalas, N. Paliatsas, D. Karageorgopoulos, F. Petraki, S. Kennou, S.A. Choulis, Thermal degradation mechanisms of PEDOT:PSS, Org. Electron. Physics, Mater. Appl. 10 (2009) 61–66. doi:10.1016/j.orgel.2008.10.008.

[20] E. Vitoratos, Conductivity Degradation Study of PEDOT: PSS Films under Heat Treatment in Helium and Atmospheric Air, Open J. Org. Polym. Mater. 2 (2012) 7–11. doi:10.4236/ojopm.2012.21004.

[21] S.I.W. Gil Ho Kim, Deok Hyun Hwang, Thermoelectric properties of nanocomposite thin films prepared with, Phys. Chem. C Hem. P Hys. (2012) 3530–3536. doi:10.1039/c2cp23517j.

[22] W. Li, G. Zheng, Y. Yang, Z.W. Seh, N. Liu, Y. Cui, High-performance hollow sulfur nanostructured battery cathode through a scalable , room temperature , (2013). doi:10.1073/pnas.1220992110/-/DCSupplemental.www.pnas.org/cgi/doi/10.1073/pnas.1220992110.

[23] J. Lee, W. Choi, Surface Modification of Sulfur Cathodes with PEDOT:PSS Conducting Polymer in Lithium-Sulfur Batteries, J.

Electrochem. Soc. 162 (2015) 935–939. doi:10.1149/2.0651506jes.

[24] W. Wang, Y. Wang, Y. Huang, C. Huang, Z. Yu, H. Zhang, A. Wang, K. Yuan, The electrochemical performance of lithium-sulfur batteries with LiClO 4 DOL/DME electrolyte, J. Appl. Electrochem. 40 (2010) 321–325. doi:10.1007/s10800-009-9978-z.

[25] H. Li, M. Sun, T. Zhang, Y. Fang, G. Wang, Improving the performance of PEDOT-PSS coated sulfur@activated porous graphene composite cathodes for lithium–sulfur batteries, J. Mater. Chem. A. 2 (2014) 18345–18352. doi:10.1039/C4TA03366C.

[26] B.Y.K. Venkateswarlo, Raman spectrum of sulphur, Proc. Iucl. Acad. Sci., A,. Xll, (1940) 453–461.

[27] S. Garreau, G. Louarn, J. Buisson, In situ spectroelectrochemical Raman studies of poly (3, 4-ethylenedioxythiophene)(PEDT), Macromolecules. 32 (1999) 6807. doi:10.1021/ma9905674.

[28] S. Sakamoto, M. Okumura, Z. Zhao, Y. Furukawa, Raman spectral changes of PEDOT-PSS in polymer light-emitting diodes upon operation, Chem. Phys. Lett. 412 (2005) 395–398. doi:10.1016/j.cplett.2005.07.040.

[29] Y. An, P. Wei, M. Fan, D. Chen, H. Chen, Q.J. Ju, G. Tian, K. Shu, Dual-shell hollow polyaniline/sulfur-core/polyaniline composites improving the capacity and cycle performance of lithium-sulfur batteries, Appl. Surf. Sci. 375 (2016) 215–222. doi:10.1016/j.apsusc.2016.03.070.

[30] H. Xu, Y. Deng, Z. Shi, Y. Qian, Y. Meng, G. Chen, F. Wei, C.M. Wang, L. V. Saraf, J.G. Zhang, I.A. Aksay, J. Liu, Graphene-encapsulated sulfur (GES) composites with a core–shell structure as superior cathode materials for lithium–sulfur batteries, J. Mater. Chem. A. 1 (2013) 15142. doi:10.1039/c3ta13541a.

[31] L. Yuan, X. Qiu, L. Chen, W. Zhu, New insight into the discharge

process of sulfur cathode by electrochemical impedance spectroscopy, J. Power Sources J. 189 (2009) 127–132. doi:10.1016/j.jpowsour.2008.10.033.

CHAPTER 6

Poly(Ethylene Oxide) (PEO) - Poly(Vinyl Pyrrolidone) (PVP) Blend Polymer Based Solid Electrolyte Membranes for Developing Solid State Magnesium Ion Cells

Abstract:

This chapter deals with the investigations carried out on the solid polymer electrolyte (SPE) material, based on the polymer blend of poly(ethylene oxide) and poly(vinyl pyrrolidone), complexed with magnesium nitrate. Flexible and free-standing membranes of this SPE are obtained by solution casting technique. These SPE membranes are found to have quite high Mg ion conductivity at room temperature, higher than the previously reported ionic conductivity for solid polymer electrolytes, complexed with Mg salts. The chapter begins with the synthesis procedures and the structural characterization of the SPE membranes and evolves into analyzing their application prospects in developing all solid state Mg ion cells, based on the detailed electrochemical studies.

Anilkumar.K.M. ,et al Poly(ethylene oxide) (PEO) - Poly(vinyl pyrrolidone) (PVP) blend polymer based solid electrolyte membranes for developing solid state magnesium ion cells, Eur. Polym. J. (2017). doi:10.1016/j.eurpolymj.2017.02.004.

6.1 Introduction

All solid-state, rechargeable cells, assembled using solid electrolytes have many distinct advantages over those with liquid electrolytes. The main advantage is the prevention of the leakage of the electrolyte from the cell which may result in chemical reactions with the cell container that can damage the cell performance. Consequently, the need for robust sealing of the cell can also be avoided [1] . Miniaturization of the device design is another added advantage of using solid electrolytes [2]. Solid-state cells have long shelf life and are inherently safer [3,4]. Solid polymer electrolyte(SPE) membranes have recently been identified as promising candidates for developing all-solid-state electrochemical devices like rechargeable cells, fuel cells and supercapacitors [5,6]. The flexibility and the excellent, mechanical, chemical, and thermal stability possessed by the SPE membranes facilitate the designing of devices of any desirable shape or size, having intimate electrode/electrolyte contact and with wider temperature ranges of operation, excellent cycling stability and shelf life [7] .They can also serve as the separator membranes between the electrodes along with helping in the transportation of ions.

Rechargeable cells based on Li, Na, and Mg are currently being widely investigated for applications in portable electronic devices and hybrid electric vehicles owing to the abundance and availability of the starting materials along with the high energy density and stable electrochemical behavior inherent to them. Lithium being the lightest metal, the Li-ion technology has dominated the scenario during the past two decades [8–11]. Magnesium ion cells are being identified as possible replacements for lithium-ion cells, with the significant advantages of comparatively lower production costs and the more availability of magnesium on earth [12]. Beyond the economic and environmental concerns, magnesium is also beneficial as an anode material due to its non-dendritic electrochemical behavior and the large theoretical volumetric capacity[13] of 3832 mAh/cm^3 . Many research groups are concentrating on the development of magnesium ion cells with high specific capacity, efficiency and good cycling stability, using suitable electrolyte materials [14]. The first step in the full-fledged development of secondary Mg ion cells should be the identification of suitable electrolyte materials, capable of maintaining the stability of the anode , in which Mg can be reversibly, deposited [15,16].

Poly(ethylene oxide) (PEO) is a semi crystalline polymer constituted by both crystalline and amorphous micro structures. It is possible to have complex formation of PEO with a wide variety of salts of lithium , sodium and magnesium [17,18]. Initially it has been assumed that the ion transport in PEO is promoted by the presence of the crystalline phases and the ions move along the PEO helices. However, the sole function of the amorphous phases of PEO in effecting ion transport in PEO could soon be identified [19].

The dissociation of inorganic salts in polymer hosts can be easily effected, provided the lattice energy of the salt is low and the dielectric constant (ε) of the host polymer high. The fraction of free ions that can be effectively transported is a significant factor. A prerequisite for the formation of free ions and the subsequent enhancement in ionic conductivity is the good extent of dissociation of the salt in the polymer [20]. The degree of dissociation of the salt dissolved in the polymer host is dependent on the total concentration of the salt in the polymer matrix. Generally, the degree of dissociation decreases with increasing salt concentration [2]. As a consequence, the fraction of "free ions" is a maximum at an optimal salt concentration. Polymer_based electrolytes synthesized from solvate-free magnesium salts such as $MgCl_2$ and Mg(SCN), incorporated in poly(ethylene oxide) are found to show a low ionic conductivity at temperatures below 100 ºC [21].

Two or more polymers can be blended to get new polymeric materials with desired mechanical strength and charge transport properties [22]. The most common interactions present in polymer blends are hydrogen bonding and ionic and dipole interactions. The blend systems have many advantages, the most significant one being the control over the physical and the micro-structural properties in terms of the compositional changes [23].The polymer, most commonly used for developing solid electrolytes is poly(ethylene oxide) [24] . The good ionic conductivity of PEO is due to the ionic transport in the amorphous region, and hence, the conductivity decreases with the increase in the extent of crystalline order. [25] . Poly(vinyl pyrrolidone) (PVP) is a promising material for making polymer blends with PEO, because of the following unique properties. First of all, PVP is an amorphous polymer that possesses high glass transition temperature (T_g) due to the presence of the rigid pyrrolidone group [26]and the amorphous nature permits faster ionic mobility compared to other semi-crystalline polymers. The presence of the carbonyl group (C=O) in the side chains of PVP facilitates complex formation with a large variety of inorganic salts [27] .

The present work is focused on realizing flexible and free-standing membranes of the polymer blend, PEO-PVP, complexed with the Mg salt, $Mg(NO_3)_2$, named as the solid polymer electrolyte (SPE) , using solution casting technique and assessing their suitability in the design of solid state Mg ion cells. The obtained SPE membranes are characterized by X-ray diffraction (XRD), Fourier transform infrared (FTIR) spectroscopy, Raman spectroscopy, scanning electron microscopy (SEM), thermo-gravimetric analysis (TGA), impedance spectroscopic analysis, transport number studies and cyclic voltammetry (CV) analysis.

6.2 Experimental details

Poly(ethylene oxide) (PEO) (average molecular weight 100,000, purity - 98-99 %), poly(vinyl pyrrolidone) (PVP) (average molecular weight 360,000,purity - 99 %) and $Mg(NO_3)_2$ (purity - 99 %) were purchased from Sigma Aldrich and were used as received for synthesizing the solid polymer electrolyte (SPE) membranes, based on the polymer blend, PEO-PVP, complexed with $Mg(NO_3)_2$.

As the first step of the synthesis, 0.1 g of PVP and 0.4 g of PEO were mixed in 5 ml anhydrous methanol and the mixture was stirred continuously at 700 rpm for 3 hours to get the polymer blend of PEO and PVP. To the solution of the polymer blend, the required amount of $Mg(NO_3)_2$ (taken as 10 weight % of the polymer blend), dissolved in 5 ml anhydrous methanol was added drop wise and the stirring was continued for 2 hours. The whole mixture was transferred to a teflon petri dish and kept in a vacuum oven at 80 ºC for 12 hours to form flexible SPE membranes (labeled as Mg10) of thickness 100-150 µm, which could be peeled off from the petri dish to form free standing membranes. The experiment was repeated for different amounts of $Mg(NO_3)_2$ corresponding to 15,20,25 and 30 weight percentages of the polymer blend and the resulting membrane samples were labeled as Mg15, Mg20, Mg25 and Mg30 respectively.

The cathode active material, $MgMn_2O_4$ used for assembling the magnesium ion cells, was synthesized by sol-gel method as described in previous reports [28]. Required amounts of magnesium acetate and manganese acetate, were dissolved in 100 ml of de-ionized water. Citric acid was added to this solution in the 1:1 molar ratio of metal ions to citric acid. The solution was stirred and heated on a hot plate until all of the liquid evaporated. The resulting material was fired in a furnace at 450 °C for 5 hours. The powder obtained was then pelletized and fired at a temperature of 900 °C for 12 hours to obtain $MgMn_2O_4$ .This spinel-type material was used as the positive electrode for assembling the magnesium-ion cells.

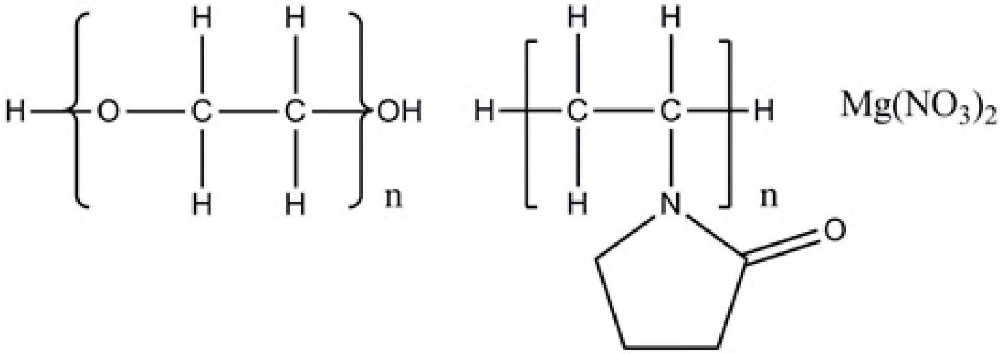

Chart 1: Schematic representation of the formation of the PEO-PVP-$Mg(NO_3)_2$ based SPE

In order to investigate the structural aspects of these SPE membranes, the XRD patterns were recorded using Rigaku Dmax C diffractometer with Cu K_α radiation. The IR spectra of the samples were obtained in the wave number range 400–4000 cm^{-1} using the JASCO 4100 model FTIR spectrophotometer. Raman spectra were acquired using Horiba LabRam (800 nm) HR spectrometer equipped with a 514 nm argon ion laser of 15 mW power. The field emission scanning electron microscopic (FE-SEM) images were collected using Carl-Zeiss Sigma electron microscope. The schematic representation of the formation of the SPE membrane, based on the PEO-PVP blend, complexed with

$Mg(NO_3)_2$,is represented in chart1, drawn with the help of CHEMDRAW Ultra 12.0 software.

The thermo-gravimetric analysis (TGA) of PEO, PVP, PEO-PVP polymer blend and the SPE membrane samples was done from room temperature to 700 °C using the Perkin Elmer, Diamond machine. The SPE membrane was sandwiched between two stainless steel blocking electrodes in a sealed teflon cell case for carrying out the impedance measurements. The ionic conductivity of the SPE membrane was measured using HP4192A impedance analyser, in which the ac frequency was scanned from 5 MHz to 5 Hz. The ac impedance was measured in the temperature range from 298 K to 358 K. The ionic transport number of the mobile species in the SPE membrane was calculated using Wagner's D.C. polarization technique. The cationic transference number of the SPE membrane was evaluated by Evans method using non-blocking electrode configuration and the cyclic voltammetry studies were carried out using the Bio-Logic SP-300 unit.

6.3 Results and Discussion

6.3.1 The X-ray diffraction(XRD) analysis

The XRD patterns of PEO,PVP, $Mg(NO_3)_2$ and the SPE membranes are shown in figure 1. Pure PEO, being semi crystalline has two intense peaks at 19.2 ° and 23.6 ° and a less intense one at 27.1 ° corresponding to the (1 2 0) , (1 1 2) and (2 2 2) planes respectively [29,30]. The PVP being totally amorphous does not give rise to any crystalline peaks [18]. Two broad amorphous peaks are observed at 11 ° and 22 °.

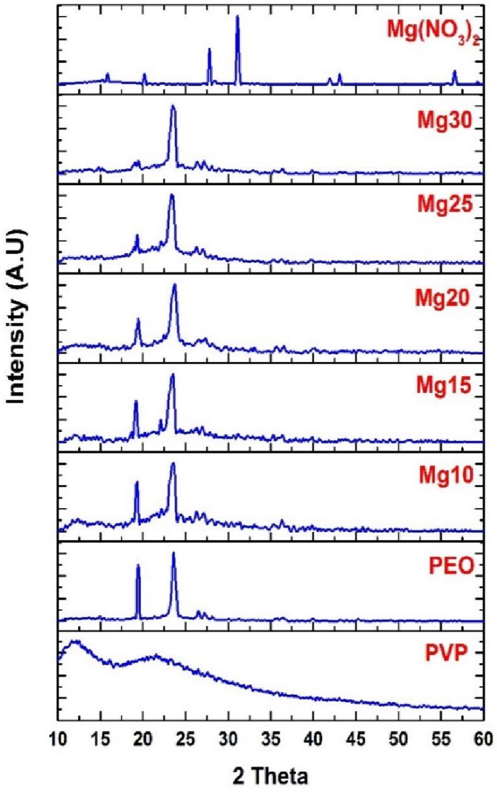

Figure 1: The XRD patterns of $Mg(NO_3)_2$, pure PEO, pure PVP and the SPE membranes

Figure 2: The photograph of the solid polymer electrolyte (SPE) free-standing membrane.

In order to analyze quantitatively, the effect of $Mg(NO_3)_2$ salt on the crystalline nature of the SPE membrane consisting of PEO-PVP blended polymer and $Mg(NO_3)_2$, the intensity of the most intense peak at 23.6 ° of PEO is normalized and the effect on the other intense peak at 19.2 ° is studied for different concentrations of $Mg(NO_3)_2$ in the SPE membrane. With the addition of $Mg(NO_3)_2$ to PEO-PVP blend, the peak at 19.2 ° becomes less intense, indicating enhancement in the amorphous nature of the blended polymer. The amorphous structure facilitates better ionic diffusivity and the ionic conductivity is subsequently enhanced [20,31,32]. The absence of the $Mg(NO_3)_2$ peaks in the XRD patterns of the SPE membranes indicates the complete dissolution of salt in the blended polymer matrix. The photograph of the SPE membrane, which is free-standing and flexible, is shown in figure 2.

6.3.2 Fourier transform infrared (FTIR) spectroscopy studies

The FTIR spectra of pure PEO, pure PVP, Mg $(NO_3)_2$, PEO-PVP polymer blend and the SPE membrane sample Mg30 are shown in figure 3(A). The spectrum of pure PEO shows absorption peaks at 2870 cm^{-1}, between 1300-1400 cm^{-1}, 1100 cm^{-1}, 950 cm^{-1} and 845 cm^{-1}. The broad peak at 2870 cm^{-1} is the inherent band of the asymmetric C-H stretching of the CH_2 group of PEO [20] . The peak at 1100 cm^{-1} corresponds to the C-O-C stretching vibration of PEO and is also attributed to the presence of the amorphous content of PEO. The peaks between 1300-1400 cm^{-1} are related to the swinging vibrations of C-H in the CH_2 group of PEO and are also the signatures of its amorphous phase [33]. The peaks at 950 cm^{-1} and 845 cm^{-1} are assigned to the CH_2 rocking vibrations of the methylene group and are related to the helical structure of PEO. The IR spectrum of pure PVP shows a peak at 2950 cm^{-1} corresponding to the CH_2 asymmetrical vibration. The C=O stretching and the C-N stretching vibrations in PVP are observed at 1665 cm^{-1} and 1332 cm^{-1} respectively. The peak at 1465 cm^{-1} is attributed to the CH_2 bending vibration. The broad peak at 3450 cm^{-1} is due to the presence of adsorbed moisture.

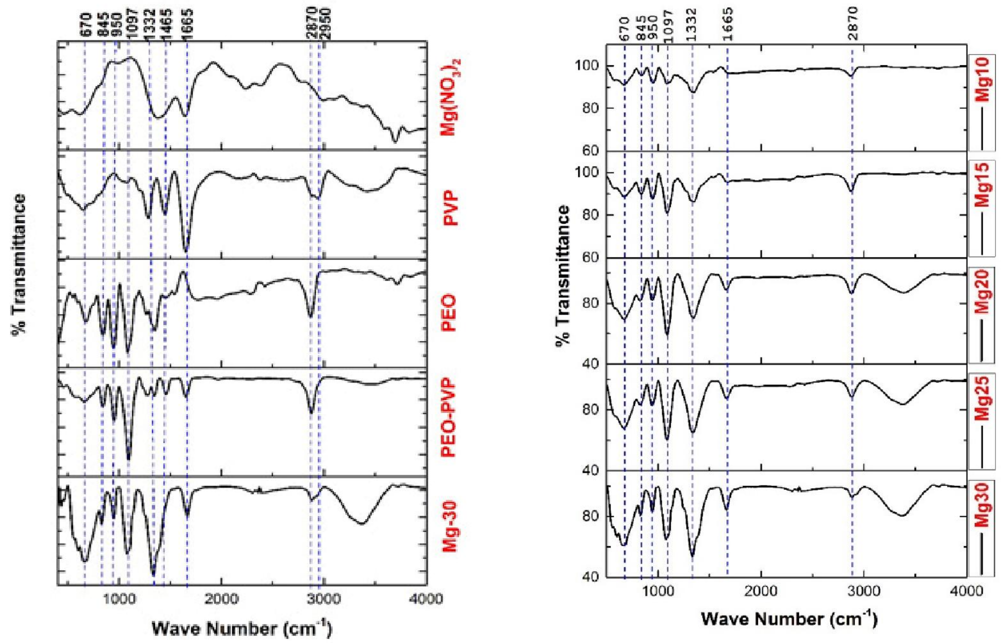

Figure3: (A) The FTIR spectra of PEO, PVP, $Mg(NO_3)_2$, PEO-PVP polymer blend and the SPE membrane Mg30;(B) The FTIR spectra of the SPE membranes with different concentrations of $Mg(NO_3)_2$.

The co-existence of the peak of PEO at 2870 cm^{-1} and that of PVP at 1665 cm^{-1}, in the IR spectrum of the PEO-PVP blend indicates that PEO and PVP form a good blend, upon mixing. The peak at 1097 cm^{-1} corresponding to the C-O-C vibration in PEO is found to be enhanced in intensity in the spectrum of the PEO-PVP blend .The CH_2 stretching vibration of PVP observed at 2950 cm^{-1} , gets shifted to 2870 cm^{-1}, in the spectrum of the PEO-PVP blend. These observations also confirm that the blend formation between PEO and PVP is effective to produce a homogeneous and stable polymer blend.

On the addition of the $Mg(NO_3)_2$ salt into the polymer blend, an increase in the intensity of the peaks between 1300 cm^{-1} -1400 cm^{-1} is observed. This could be due to the overlapping of the peaks observed in pure $Mg(NO_3)_2$, PEO and PVP in the above region [34]. The intensity of the peaks at 845 cm^{-1} and 950 cm^{-1} of PEO gets enhanced in the spectra of the SPE membrane samples due to the stretching of the helical confirmation of PEO, upon the incorporation of the Mg salt, so that the structure of PEO is completely distorted [35]. The peak observed at 670 cm^{-1} in the IR patterns of the SPE membranes with enhanced intensity, indicates the presence of Mg-O vibrations [36]. The changes in the intensity of the peaks, broadening of the peaks and the shifting of the peaks to lower wave numbers are observed as the effects of the Mg salt incorporation, on the vibrational modes of the PEO-PVP polymer blend. The anticipated Mg^{2+} incorporation into the PEO-PVP blend system is schematically illustrated in chart 1. In the chart, the dotted lines in the C-O-C group of PEO and the C=O group of PVP are the possible coordination sites for the incorporation of Mg^{2+} ions into the PEO-PVP polymer blend system, to form the SPE membrane.

The effect of varying the Mg salt concentration in the SPE samples, on their IR spectra is illustrated in figure 3(B). It is observed that the intensity of the peak corresponding to the C=O group in PVP at 1665 cm^{-1} gets enhanced in tune with the enhancement in the concentration of the Mg salt. This observation provides additional possibility for the C=O group of PVP to act as the coordination site for Mg^{2+} incorporation. The peak observed at 3450 cm^{-1} is found to get enhanced in intensity with the increase in the concentration of the $Mg(NO_3)_2$ in the SPE samples. This peak represents the adsorbed moisture content and the enhancement in intensity could be due to the cumulative effect of the amount of moisture content in the SPE samples. The Mg salt concentration was increased up to 30%, resulting in the sample Mg30, and further enhancement in the concentration was not practically possible due to the poor quality of the resulting SPE membranes.

6.3.3 The analysis of the Raman spectroscopy data

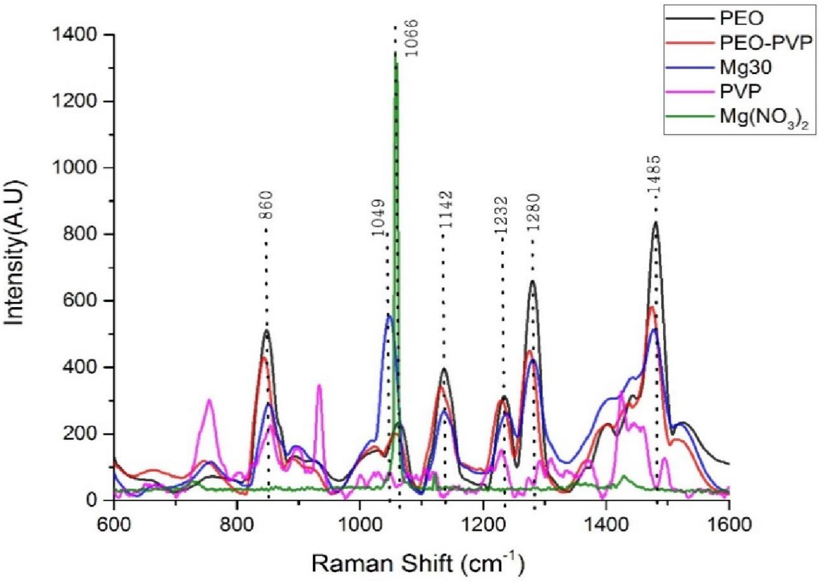

Figure 4: The Raman spectra of PEO, PVP, $Mg(NO_3)_2$, PEO-PVP polymer blend and the SPE sample Mg30

The Raman spectra of PEO, PVP, $Mg(NO_3)_2$, PEO-PVP polymer blend and the SPE sample, Mg30 are shown in figure 4. The characteristic Raman peaks of PEO are observed at 1485 cm^{-1} (bending mode CH_2), 1280 cm^{-1} (CH_2 symmetric stretching), 1232 cm^{-1} (CH_2 asymmetric stretching) and 1066 cm^{-1} (C–O-C stretching) [37]. In PEO and PVP, the peak at 1142 cm^{-1} corresponds to the rocking modes of CH_2 vibrations [38]. In the Raman pattern of Mg30, a strong peak is observed at 1049cm^{-1} due to the presence of the paired [39] anion $(NO_3)^-$ .The presence of $(NO_3)^-$ like anions in the polymer matrix is reported to improve the amorphous nature of the host polymer[35]. The broadening of the peaks in the Raman spectra indicates the enhanced amorphous nature of the blended polymer. By the addition of the Mg salt to the PEO-PVP polymer blend, the broadening of the Raman modes increases, resulting in drastic reduction in the peak intensity [40,41]. The Raman spectroscopic studies support the conclusions arrived at from the XRD analysis, regarding the enhanced amorphous nature of the SPE samples.

6.3.4 Field emission scanning electron microscopy(FE-SEM)studies

The scanning electron microscopy is an excellent technique to assess the compatibility between various phases of the materials under study, through the detection of phase separations and interfaces [42]. The FE-SEM images of pure PEO, PEO-PVP polymer blend and the SPE sample, Mg30 reveal various surface morphologies as shown in figure 5.

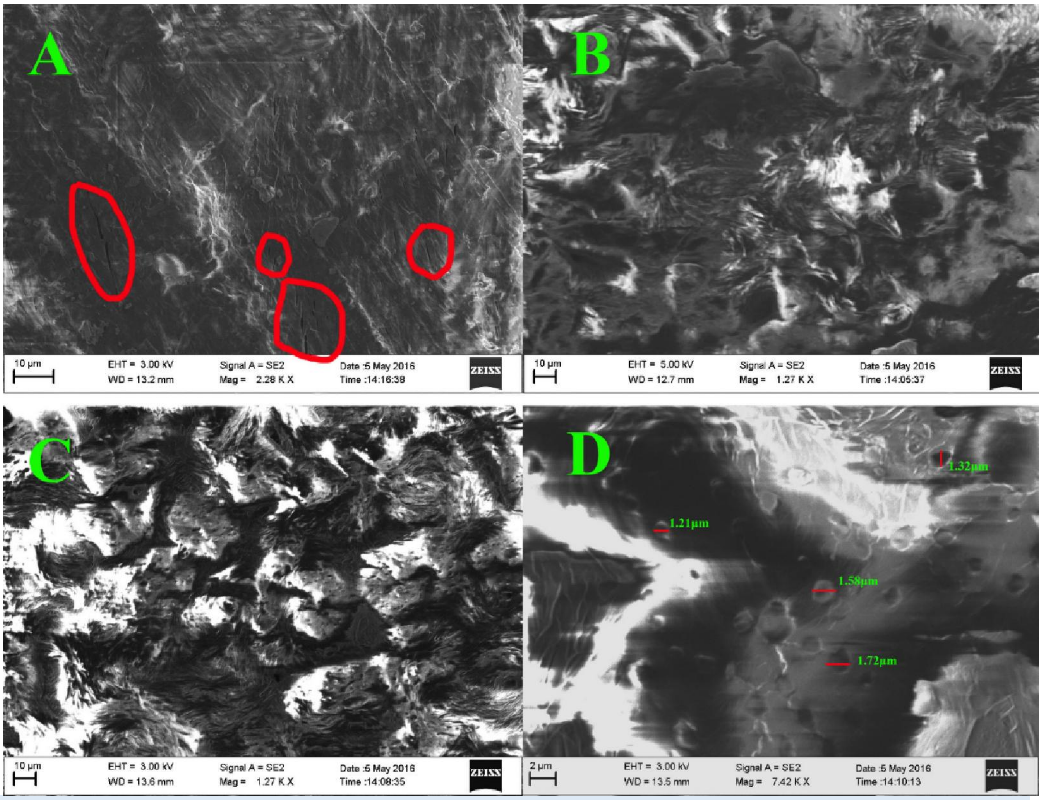

Figure 5: The FE-SEM images of (A) PEO; (B) PEO-PVP polymer blend; (C) & (D) SPE sample, Mg30

It can be seen from figure 5(A), that the micro structure of pure PEO shows several micro-cracks due to the rigid nature of PEO. After the formation of the polymer blend with PVP, the micro cracks disappear and the sample surface becomes more flexible due to the increase in the amorphous nature of the polymer blend, as seen from figure 5B [43]. On adding the Mg salt to the polymer blend, it is observed that, in addition to retaining the smooth appearance of the blend, several micro pores are also formed, as illustrated in figures 5C and 5D.These micro pores have average size around 1.5µm. The presence of such pores on the surfaces of the membranes is one of the desirable characteristics of the separator membranes used in rechargeable cells[44]. The random distribution and the dissociation of the Mg salt in the PEO-PVP polymer blend brings about a topological disorder in the blend which enhances the flexibility of the SPE membranes. The flexible nature makes the membranes more amorphous and this observation is well supported by the X-ray diffraction and the Raman spectroscopic studies.

6.3.5 *Thermo-gravimetric analysis (TGA)*

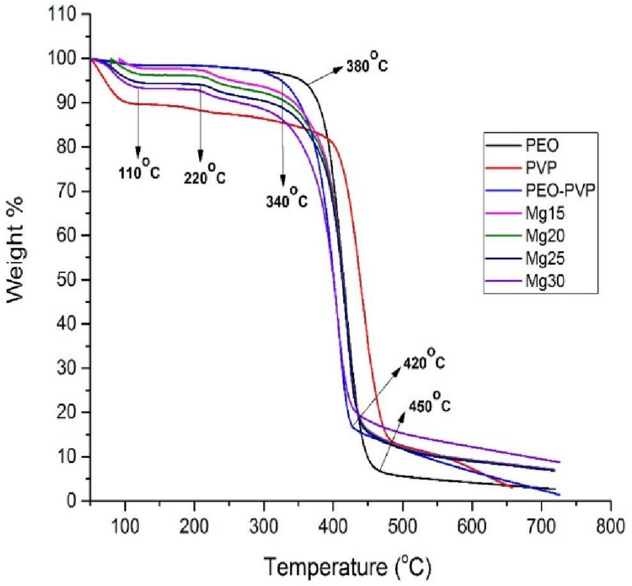

Figure 6: The TGA curves of PEO, PVP, PEO-PVP polymer blend and the SPE membranes

The TGA curves of PEO, PVP, PEO-PVP polymer blend and the SPE membrane samples are shown in figure 6. The weight loss of the samples with temperature was investigated under nitrogen ambience. For the pure PEO sample, there is a plateau extending up to 380 °C indicating minimal weight loss and good thermal stability up to 380 °C, and the sample gets completely dissociated at 450 °C. The TGA curve of PVP shows an initial weight loss of 10 % around 110 °C due to the release of adsorbed moisture. For the PEO-PVP polymer blend sample, the region without significant weight loss is up to 340 °C. Compared to the crystalline and rigid sample PEO, the PEO-PVP blend system is more amorphous and flexible, which results in a lower decomposition temperature for the polymer blend. There are two weight loss regions observed in the SPE membrane samples. The first region is up to 110 °C with a weight loss of around 7 % , which can be attributed to the evaporation of the trace amounts of the residual solvent and adsorbed moisture [45] . Thereafter there is a flat region extending up to 220 °C without any significant weight loss. The next weight loss region is around 340 °C with a weight loss of around 20 %, corresponding to the decomposition of the SPE membrane. A sharp fall is observed at 340 °C which is due to the degradation of the back bone of the PEO-PVP polymer blend and all the SPE membrane samples get completely dissociated at 420 °C. Such decompositions are usually observed in polymer samples due to the random decompositions or polymer unzipping [33]. The decomposition temperature observed for the SPE samples in the present work is considerably higher than that of the liquid electrolytes currently employed in Mg ion secondary cells [46]. The thermal analysis indicates that the SPE membranes of the present work are thermally stable up to 220 °C and are hence quite suitable for applications in high temperature Mg ion cells.

6.3.6 *Ionic conductivity studies*

The electrochemical impedance analysis was carried out using stainless steel blocking electrodes and the complex impedance plots (the Nyquist plots) for the SPE membrane sample, Mg30, at different temperatures are shown in figure 7(A). The impedance plots can be modeled to the general equivalent circuit, shown in figure 7(B), where R_b represents the resistance of the SPE membrane, C_{dl} is the coupling capacitance between the SPE membrane and the electrodes in the measuring circuit and Q, the constant phase element [47]. The complex impedance plots show two well-defined regions. The bulged semicircle observed in the high frequency region is due to the bulk effect of the SPE membrane, and the linear region, in the low frequency range arises due to the effect of the blocking electrodes. This linear tail indicates the capacitive nature of the interface and the absence of electronic conductivity[48].

The room temperature ionic conductivity of the SPE membrane samples was calculated using the equation

$$\sigma = {}^{t}/_{R_b A} \ \dots\dots\dots\dots\dots\dots\dots\dots\dots.. (1)$$

where t is the thickness of the membrane sample, R_b, the bulk resistance and A the cross sectional area of the sample [49]. The measurement was carried out in the frequency range of 5 MHz to 5 Hz of the ac source with an amplitude of 10 mV_{pp}.The variation of the ionic conductivity of the SPE membranes with the concentration of $Mg(NO_3)_2$ in the samples is shown in figure 8A and it is observed that the maximum ionic conductivity of the SPE membrane is around 5.8×10^{-4} S cm^{-1} at room temperature for the sample Mg30. This is much higher compared to that of the PEO-PVP polymer blend, which is only around 1.13×10^{-8} S cm^{-1} [34] .

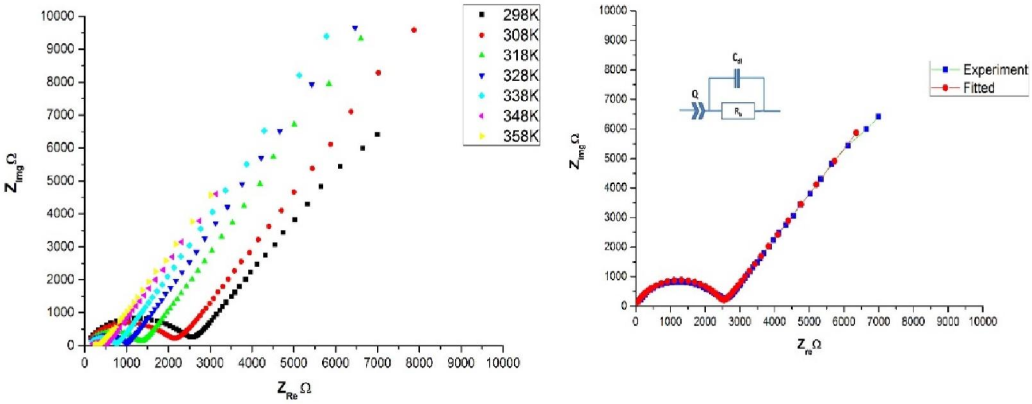

Figure 7: (A) The Nyquist plots of the Mg30 sample at different temperatures (B) The Nyquist plot of the Mg30 sample with theoretical fit

The ionic conductivity saturates around the maximum value observed and any further increase in the concentration of the Mg salt, $Mg(NO_3)_2$, results in the formation of poor quality SPE membranes. The present studies on the PEO/PVP/ $Mg(NO_3)_2$ based solid polymer electrolyte membranes, for applications in Mg ion cells are quite novel and have not been reported earlier. There are reports on PEO-Mg salt based solid electrolyte with ionic conductivity ranging from 10^{-5} to 10^{-4} S cm^{-1} at 80–100 °C [50,51]. The polymer electrolyte obtained by incorporating $Mg(NO_3)_2$ in PVA–PVP polymer blend is reported to have an ionic conductivity of 3.44×10^{-5} S/cm[52]. For the complex, (PEO-PMA)/PEGDE/MgX_2 ,an ionic conductivity around 4×10^{-4} S cm^{-1} has been reported for the system containing $Mg[(CF_3SO_2)_2N]_2$ at 60°C, but not at room temperature[53]. Compared to the previous reports, the room temperature ionic conductivity of the SPE membranes of the present work is quite high and is of much significance in the design of all solid state Mg ion cells.

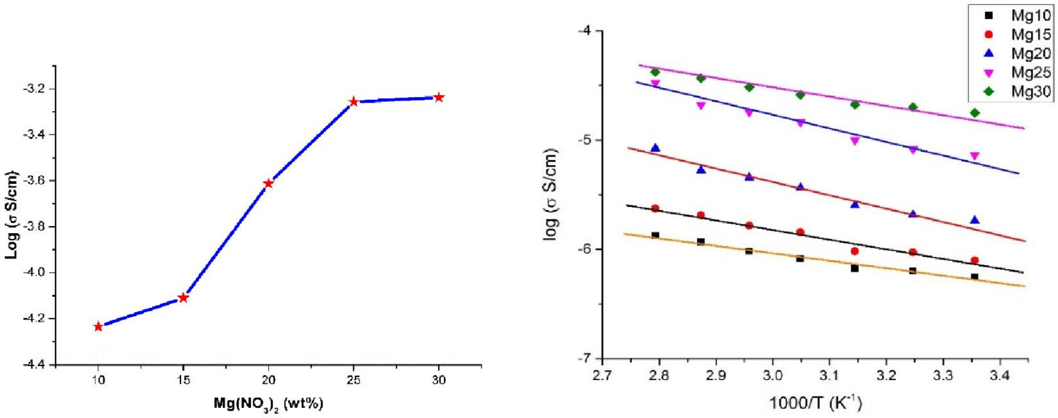

Figure 8 (A): The variation of the ionic conductivity of the SPE membranes with the concentrations of $Mg(NO_3)_2$ in the membranes at room temperature (B) The Arrhenius plots of the SPE membranes.

It is also observed that the ionic conductivity of the SPE membrane samples increases with increase in the concentration of $Mg(NO_3)_2$ and attains a saturated value. The increase in the ionic conductivity with the increase in the Mg salt concentration can be related to the increase in the concentration of the mobile charge carriers in the SPE samples [54]. The ionic conductivity attains saturation mainly due to the formation of ion pairs and ion aggregates [55].

Beyond the saturation limit, the number of mobile charge carriers gets reduced and the quality of the membranes formed is also affected [21].

The variation of the ionic conductivity, as a function of the temperature in the range 298-358 K for the SPE membrane samples is shown in figure 8(B). It can be seen that the conductivity obeys the Arrhenius behavior as expected for the electrolyte materials. The excellent correspondence with the Arrhenius behavior is evident from figure 8(B) [56,57]. With the increase in temperature, the ionic conductivity of the SPE samples is found to get enhanced. The rise in temperature results in polymer expansion to produce free volume which facilitates enhancement in ionic mobility and polymer segmental mobility[58] and in turn gives rise to increase in the ionic conductivity. The conductivity-temperature plots follow the Arrhenius behavior throughout the temperature range. The variation of the ionic conductivity σ with temperature T can be fitted to the equation given below [59],

$$\sigma = \sigma_o \exp\left(\frac{E_a}{KT}\right) \qquad \ldots\ldots\ldots\ldots\ldots\ldots\ldots\ldots\ldots.(2)$$

where σ_o is a constant, K, the Boltzmann constant, and E_a, the thermal activation energy. The activation energy for the Mg30 sample with the highest ionic conductivity is found to be 0.31 eV. It is the energy required to provide the suitable conductive conditions for the smooth migration of the ions through the electrolyte [17]. The smaller value of the activation energy obtained for the Mg30 sample indicates the possibility of the smooth and easy migration of ions through the SPE membrane sample.

6.3.7 The transport number studies

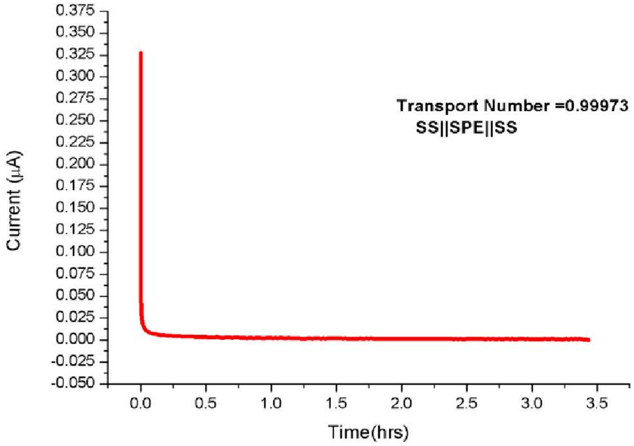

Figure 9: The variation of current with time of the SPE membrane, sandwiched between two stainless steel (SS) blocking electrodes

The total ionic transport number, t_{ion} was measured using the d.c. polarization method[60] . In this method, the d.c. current was monitored as a function of time on the application of a fixed d.c. voltage of 1V across the SS||SPE||SS arrangement, where SS stands for the stainless steel blocking electrode and SPE, the solid polymer electrolyte membrane. The current decays immediately and asymptotically approaches a steady value. The value of t_{ion} was determined from figure 9, using the equation,

$$t_{ion} = \frac{i_t - i_e}{i_t} \ldots\ldots\ldots\ldots\ldots\ldots\ldots. (3)$$

where i_t is the total current and i_e the saturated current. The value of t_{ion} is found to be 0.9997 for the SPE membrane sample which indicates that the conductivity of the sample is mainly ionic [42].

The cationic transference number T_+ of the SPE membrane, Mg30, was calculated using the Mg||SPE||Mg configuration, employing non-blocking Mg electrodes, by Evans Method [61]. In this method, the SPE membrane, sandwiched between the Mg electrodes was polarized by applying a constant voltage of about 1 V and the initial and the final current values were recorded at room temperature. Impedance measurement technique was employed to estimate the resistance of the system before and after polarization. The polarization curve of the Mg||SPE ||Mg system for the SPE membrane,Mg30, and the ac impedance plots are depicted in figure 10. The values of T_+ are obtained using the equation,

$$T_+ = \frac{I_S(V - I_0 R_0)}{I_0(V - I_S R_S)} \quad \ldots\ldots\ldots\ldots\ldots (4)$$

where I_o and I_s are the initial and the final current values respectively on d.c. polarization and R_o and R_s, the grain boundary resistance values obtained from the impedance plots, before and after polarization respectively.

For pure PEO-Mg salt complexes, it is already reported that the Mg ion conduction is almost negligible and these salts are dominantly anionic conductors [50]. Rather than using the pure PEO, in the present work, the PEO-PVP polymer blend system is used for making the complex with $Mg(NO_3)_2$. For the resulting SPE membrane sample Mg30, the value obtained for Mg ion transference number is 0.33. The earlier reports on PEO based Mg solid electrolytes give a cationic transference number close to zero [50]. One of the recent reports claims a value close to 0.45 in the presence of an ionic liquid [45].

The value of the cationic transference number obtained in the present case is 0.33. Although this number is less than the anionic transference number 0.67,the former guarantees Mg^{2+} ion flow between the electrodes, which is more important in the working of the cell.

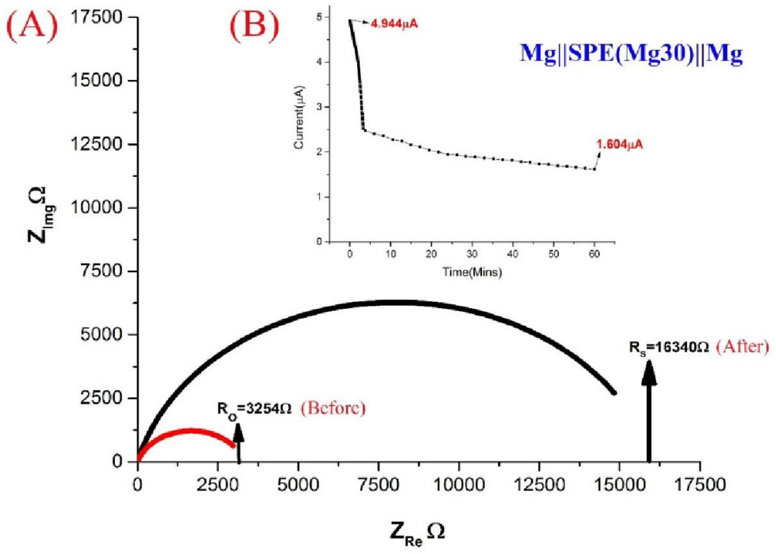

Figure 10: (A) The impedance plots of the SPE membrane, Mg30, before and after polarization. (B) The variation of current with time of the SPE membrane sandwiched between two magnesium non-blocking electrodes.

6.3.8 Cyclic voltammetry (CV) studies

The small current voltammetric response of the SPE membrane, Mg30, in SS||SPE||SS arrangement was studied using the Biologic SP300 unit at a scan rate of 0.5 mV/s from 0 to 4 V. The full cycle CV curve shown in figure 11 does not have any distinct peaks. The CV curves for five cycles are shown as inset in figure 11. The purity as well as the electrochemical stability of the SPE sample can be established on the basis of the reproducible and clear nature of the cyclic voltammetry curves [34] . From the CV curve, the stability window of the SPE sample is found to be in the voltage range 0 to 4 V.

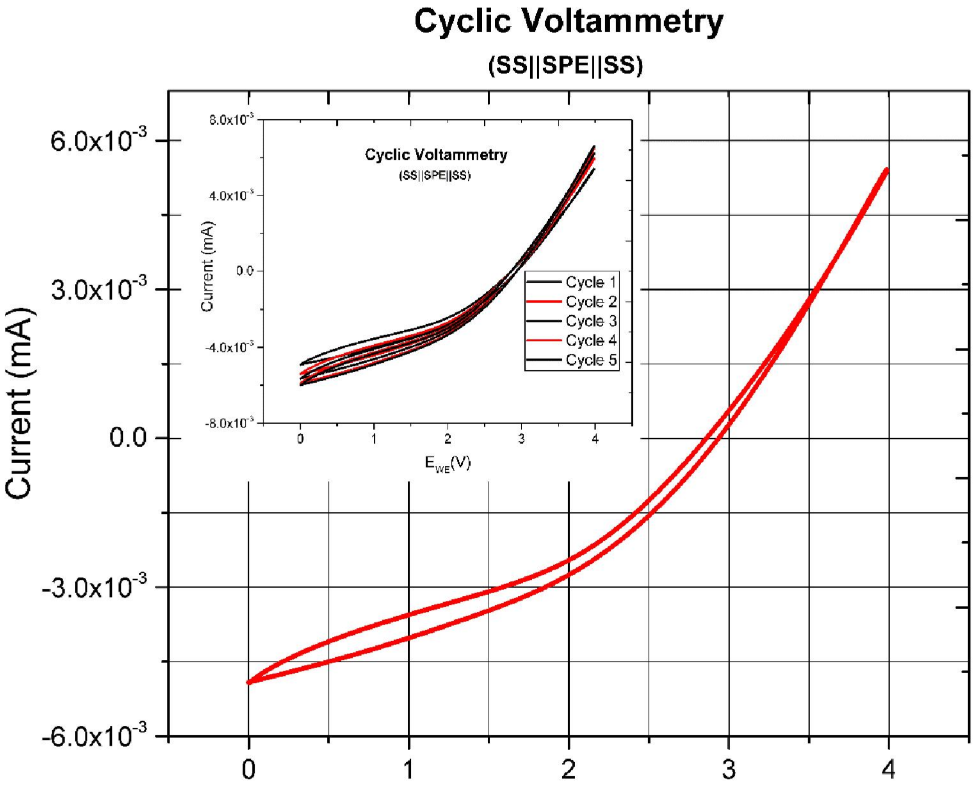

Figure 11: Cyclic voltammetry (CV) curve of the SPE membrane sandwiched between two stainless steel (SS) blocking electrodes. The CV curves for five cycles are shown as inset.

The CV analysis was repeated on the symmetric Mg||SPE||Mg arrangement, using the Mg non-blocking electrodes and the Mg30, SPE membrane sample. The CV curve is shown in figure 12. The cathodic and the anodic peaks are distinctly observed, which are not observed with the SS blocking electrode arrangement. The presence of these peaks clearly indicates Mg^{2+} ion conduction in the SPE membrane[45].

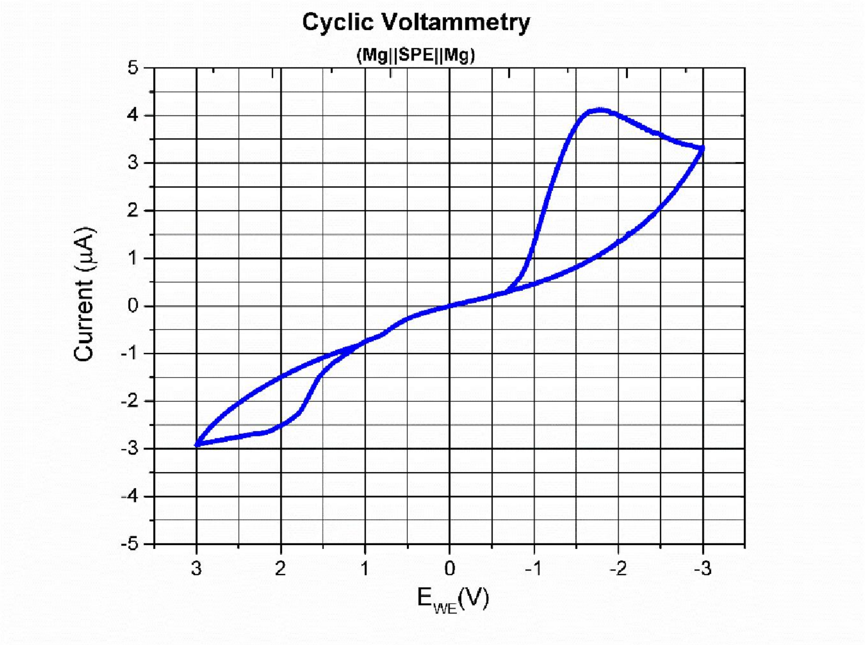

Figure 12: *Cyclic voltammetry (CV) curve of the SPE membrane sandwiched between two non-blocking Mg electrodes*

Using the SPE membrane,Mg30 as the electrolyte, all solid state electrochemical coin cells were assembled using magnesium metal as the anode and $MgMn_2O_4$ as the cathode active material. The SPE membrane,Mg30 serves both as the solid electrolyte and the separator. The cells show an open circuit voltage (OCV) of 1.46 V as illustrated in figure 13(A). The presence of the OCV indicates that the assembled cells are electrochemically active which in turn establishes the electrochemical activity of the SPE membrane sample. The assembled cells were further characterized using cyclic voltammetry at a scan rate of 0.1 mV/s and the CV curve is shown in figure 13(B). The CV curve shows the peaks corresponding to the cathodic and the anodic scan respectively at 2.24 V and 0.79 V. From the CV studies, it is observed that the Mg^{2+} intercalation occurs near 2.24 V and the deintercalation, around 0.79 V.

Large voltage difference between these intercalation and deintercalation peaks is possible in Mg ion cells mainly because of the slow kinetics of Mg insertion and the low level of attainable intercalation upon discharge [62,63]. The intercalation potential can be higher compared to the one for deintercalation, since more energy is required to insert the +2 cations into the oxide lattice. The large potential difference between the intercalation and the deintercalation processes for the Mg ion cells of the present work is also a consequence of the

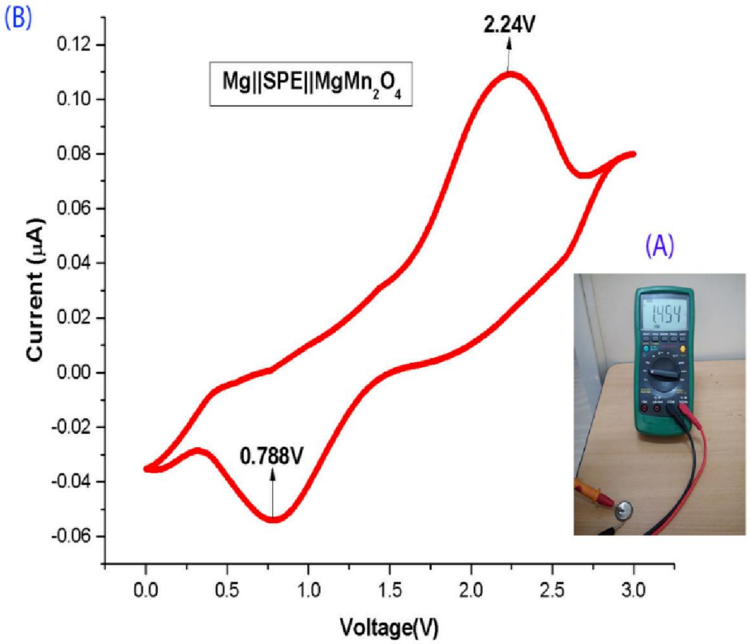

Figure 13: *(A) Open circuit voltage of the assembled Mg ion coin cell.*
(B) ***Cyclic voltammetry curve of the assembled Mg ion coin cell with $MgMn_2O_4$ as the cathode, SPE membrane*** *as the solid electrolyte cum separator and Mg metal as the anode.*

fact that the deintercalation process in Mg ion cells is not continuous and does not begin until a certain threshold voltage is reached [64,65].

6.4 Conclusions

In the present work, a fundamental study has been carried out for assessing the application prospects of the Mg salt, $Mg(NO_3)_2$, incorporated, PEO-PVP polymer blend based solid polymer electrolyte (SPE) membranes in Mg ion secondary cells. The SPE membranes, flexible and solid are synthesized for various concentrations of the Mg salt, $Mg(NO_3)_2$. The increase in the Mg salt concentration is found to bring about a decrease in the crystalline nature of the SPE, and improvement in the flexibility and ion diffusion and subsequently an enhancement in the Mg ion conductivity up to a saturation limit. The highest Mg ion conductivity observed in the present work is 5.8×10^{-4} S cm^{-1}, which is much higher than the previously reported ionic conductivity for Mg salt incorporated, solid polymer electrolytes. Based on the thermal studies, this solid electrolyte membrane is found to be thermally stable up to 220°C, which makes it suitable for designing Mg ion cells for high temperature applications. The total ionic transport number and the cationic transference number are found to be 0.9997 and 0.33 respectively for the SPE membrane sample Mg30, which is having the highest ionic conductivity. The electrochemical stability of the SPE membrane has been established on the basis of the CV studies and the stability window is found to be 4 V. The Mg ion coin cells assembled using the SPE membrane, Mg30, serving both as the solid electrolyte and the separator show an open circuit voltage of 1.46 V. The characteristic aspects of the CV curve of the coin cells establish the electrochemical activity and the rechargeable nature of the cells. These SPE membranes, developed in the present work, can be of profound applications in realizing all solid state magnesium ion cells with desired performance characteristics.

6.5 References

[1] D.E. Fenton, J.M. Parker, P.V. Wright, Complexes of alkali metal ions with poly(ethylene oxide), Polymer (Guildf). 14 (1973) 589. doi:10.1016/0032-3861(73)90146-8.

[2] C. Berthier, W. Gorecki, M. Minier, M.B. Armand, J.M. Chabagno, P. Rigaud, Microscopic investigation of ionic conductivity in alkali metal salts-poly(ethylene oxide) adducts, Solid State Ionics. 11 (1983) 91–95. doi:10.1016/0167-2738(83)90068-1.

[3] J. Li, C. Ma, M. Chi, C. Liang, N.J. Dudney, Solid Electrolyte: the Key for High-Voltage Lithium Batteries, Adv. Energy Mater. 5 (2015) 1401408. doi:10.1002/aenm.201401408.

[4] Y. Kato, S. Hori, T. Saito, K. Suzuki, M. Hirayama, A. High-power all-solid-state batteries using sulfide superionic conductors, Nat. Energy. 1 (2016) 16030. doi:10.1038/nenergy.2016.30.

[5] F.M. Gray, M. Armand, POLYMER ELECTROLYTES, in: T. Osaka, M. Datta (Eds.), ENERGY STORAGE Syst. Electron., Gordon & Breach, 2000: pp. 351–406.

[6] M.B. Armand, Polymer electrolytes, Ann. Rev. Mater. Sci. 16 (1986) 245–61. doi:10.1533/9781845699772.

[7] M. a. Ratner, D.F. Shriver, Ion transport in solvent-free polymers, Chem. Rev. 88 (1988) 109–124. doi:10.1021/cr00083a006.

[8] J. Suk, Y.H. Lee, D.Y. Kim, D.W. Kim, S.Y. Cho, J.M. Kim, Y. Kang, Semi-interpenetrating solid polymer electrolyte based on thiol-ene cross-linker for all-solid-state lithium batteries, J. Power Sources. 334 (2016) 154–161. doi:10.1016/j.jpowsour.2016.10.008.

[9] L. Porcarelli, C. Gerbaldi, F. Bella, J.R. Nair, Super Soft All-Ethylene

Oxide Polymer Electrolyte for Safe All-Solid Lithium Batteries, Sci. Rep. 6 (2016) 19892. doi:10.1038/srep19892.

[10] J.R. Nair, M. Destro, F. Bella, G.B. Appetecchi, C. Gerbaldi, Thermally cured semi-interpenetrating electrolyte networks (s-IPN) for safe and aging-resistant secondary lithium polymer batteries, J. Power Sources. 306 (2016) 258–267. doi:10.1016/j.jpowsour.2015.12.001.

[11] F. Bella, F. Colò, J.R. Nair, C. Gerbaldi, Photopolymer electrolytes for sustainable, upscalable, safe, and ambient-temperature sodium-ion secondary batteries, ChemSusChem. 8 (2015) 3668–3676. doi:10.1002/cssc.201500873.

[12] D. Aurbach, Z. Lu, A. Schechter, Y. Gofer, H. Gizbar, R. Turgeman, Y. Cohen, M. Moshkovich, E. Levi, Prototype systems for rechargeable magnesium batteries, Nature. 407 (2000) 724–727. http://www.nature.com/nature/journal/v407/n6805/abs/407724a0.html (accessed June 20, 2015).

[13] H. Oh, K. Xu, H.D. Yoo, D.S. Kim, C. Chanthad, G. Yang, J. Jin, I.A. Ayhan, S.M. Oh, Q. Wang, Poly(arylene ether)-Based Single-Ion Conductors for Lithium-Ion Batteries, Chem. Mater. 28 (2016) 188–196. doi:10.1021/acs.chemmater.5b03735.

[14] D. Aurbach, H. Gizbar, A. Schechter, O. Chusid, H.E. Gottlieb, Y. Gofer, I. Goldberg, Electrolyte Solutions for Rechargeable Magnesium Batteries Based on Organomagnesium Chloroaluminate Complexes, J. Electrochem. Soc. 149 (2002) A115. doi:10.1149/1.1429925.

[15] J. Muldoon, C.B. Bucur, A.G. Oliver, T. Sugimoto, M. Matsui, H.S. Kim, G.D. Allred, J. Zajicek, Y. Kotani, Electrolyte roadblocks to a magnesium rechargeable battery, Energy Environ. Sci. 5 (2012) 5941. doi:10.1039/c2ee03029b.

[16] C.B. Bucur, T. Gregory, A.G. Oliver, J. Muldoon, Confession of a Magnesium Battery, J. Phys. Chem. Lett. 6 (2015) 3578–3591. doi:10.1021/acs.jpclett.5b01219.

[17] K.K. Kumar, Y. Pavani, M. Ravi, S. Bhavani, A.K. Sharma, V.V.R.N. Rao, Effect of complexation of NaCl salt with polymer blend (PEO/PVP) electrolytes on ionic conductivity and optical energy band gaps, AIP Conf. Proc. 1391 (2011) 641–644. doi:10.1063/1.3643635.

[18] A.B. Puthirath, B. John, C. Gouri, S. Jayalekshmi, Lithium-doped PEO—a prospective solid electrolyte with high ionic conductivity, developed using n-Butyllithium in hexane as dopant, Ionics (Kiel). 21 (2015) 2185–2191. doi:10.1007/s11581-015-1406-2.

[19] M. Ravi, Y. Pavani, K. Kiran Kumar, S. Bhavani, A.K. Sharma, V.V.R. Narasimha Rao, Studies on electrical and dielectric properties of

PVP:KBrO4 complexed polymer electrolyte films, Mater. Chem. Phys. 130 (2011) 442–448. doi:10.1016/j.matchemphys.2011.07.006.

[20] S.A.M. Noor, A. Ahmad, I.A. Talib, M.Y.A. Rahman, Morphology, chemical interaction, and conductivity of a PEO-ENR50 based on solid polymer electrolyte, Ionics (Kiel). 16 (2010) 161–170.

[21] J.R. MacCallum, A.S. Tomlin, C.A. Vincent, An investigation of the conducting species in polymer electrolytes, Eur. Polym. J. 22 (1986) 787–791. doi:http://dx.doi.org/10.1016/0014-3057(86)90017-0.

[22] A.M. Rocco, R.P. Pereira, M.I. Felisberti, Miscibility, crystallinity and morphological behavior of binary blends of poly(ethylene oxide) and poly(methyl vinyl ether-maleic acid), Polymer (Guildf). 42 (2001) 5199–5205. doi:10.1016/S0032-3861(00)00784-9.

[23] E.M. Abdelrazek, I.S. Elashmawi, A. El-Khodary, A. Yassin, Structural, optical, thermal and electrical studies on PVA/PVP blends filled with lithium bromide, Curr. Appl. Phys. 10 (2010) 607–613.

[24] V. Thangadurai, W. Weppner, Solid state lithium ion conductors: Design considerations by thermodynamic approach, Ionics (Kiel). 8 (2002) 281–292. doi:10.1007/BF02376081.

[25] J.Y. Song, Y.Y. Wang, C.C. Wan, - Open Access LibrarySong, J.Y.; Wang, Y.Y.; Wan, C.C. Review of gel-type polymer electrolytes for lithium-ion batteries. J. Power Sources 1999, 77, 183–197, doi:10.1016/S0378-7753(98)00193-1., J. Power Sources. 77 (1999) 183–197. http://www.oalib.com/references/9023829 (accessed March 17, 2016).

[26] H. Feng, Z. Feng, L. Shen, A high resolution solid-state n.m.r. and d.s.c. study of miscibility and crystallization behaviour of poly(vinyl alcohol)poly(N-vinyl-2-pyrrolidone) blends, Polymer (Guildf). 34 (1993) 2516–2519. doi:10.1016/0032-3861(93)90581-T.

[27] P. Hu, J. Zhao, T. Wang, C. Shang, J. Zhang, B. Qin, Z. Liu, J. Xiong, G. Cui, A composite gel polymer electrolyte with high voltage cyclability for Ni-rich cathode of lithium-ion battery, Electrochem. Commun. 61 (2015) 32–35. doi:10.1016/j.elecom.2015.09.026.

[28] J.C. Knight, S. Therese, A. Manthiram, On the Utility of Spinel Oxide Hosts for Magnesium-Ion Batteries, ACS Appl. Mater. Interfaces. 7 (2015) 22953–22961. doi:10.1021/acsami.5b06179.

[29] E. Bortel, S. Hodorowicz, R. Lamot, Relation between crystallinity degree and stability in solid state of high molecular weight poly(ethylene oxide)s, Die Makromol. Chemie. 180 (1979) 2491–2498. doi:10.1002/macp.1979.021801023.

[30] K. Chrissopoulou, K.S. Andrikopoulos, S. Fotiadou, S. Bollas, C.

Karageorgaki, D.C. Los, G.A. Voyiatzis, S.H. Anastasiadis, Crystallinity and Chain Conformation in PEO / Layered Silicate Nanocomposites, Macromolecules. 44 (2011) 9710–9722.

[31] A.R. Polu, R. Kumar, Preparation and characterization of PEG–Mg (CH3COO) 2–CeO2 composite polymer electrolytes for battery application, Bull. Mater. Sci. 37 (2014) 309–314. http://link.springer.com/article/10.1007/s12034-014-0654-5 (accessed June 20, 2015).

[32] C. V Subba Reddy, A.-P. Jin, Q.-Y. Zhu, L.-Q. Mai, W. Chen, Preparation and characterization of (PVP + NaClO4) electrolytes for battery applications., Eur. Phys. J. E. Soft Matter. 19 (2006) 471–476. doi:10.1140/epje/i2005-10076-8.

[33] K.K. Kumar, M. Ravi, Y. Pavani, S. Bhavani, A.K. Sharma, V.V.R. Narasimha Rao, Investigations on PEO/PVP/NaBr complexed polymer blend electrolytes for electrochemical cell applications, J. Memb. Sci. 454 (2014) 200–211. doi:10.1016/j.memsci.2013.12.022.

[34] S. Chapi, R. S., D. H., Enhanced electrochemical, structural, optical, thermal stability and ionic conductivity of (PEO/PVP) polymer blend electrolyte for electrochemical applications, Ionics (Kiel). (2015). doi:10.1007/s11581-015-1600-2.

[35] K.N. KUMAR, M.V. REDDY, L. VIJAYALAKSHMI, Y.C. RATNAKARAM, Synthesis and analysis of Fe3+, Co2+ and Ni2+: PEO + PVP blended polymer composite films for multifunctional polymer applications, Bull. Mater. Sci. 38 (2015) 1015–1023. doi:10.1007/s12034-015-0925-9.

[36] Z. Rezvani, F. Arjomandi Rad, F. Khodam, Synthesis and characterization of Mg-Al-layered double hydroxides intercalated with cubane-1,4-dicarboxylate anions., Dalton Trans. (2014). doi:10.1039/c4dt03152k.

[37] I.S. Elashmawi, L. H. Gaabour, Raman, morphology and electrical behavior of nanocomposites based on PEO/PVDF with multi-walled carbon nanotubes, Results Phys. 5 (2015) 105–110. doi:10.1016/j.rinp.2015.04.005.

[38] X.H. Li, L.J. Zhao, J.L. Dong, H.S. Xiao, Y.H. Zhang, Confocal raman studies of Mg(NO3)2 aerosol particles deposited on a quartz substrate: Supersaturated structures and complicated phase transitions, J. Phys. Chem. B. 112 (2008) 5032–5038. doi:10.1021/jp709938x.

[39] X. Ji, W. Yang, Study of chemical processes involved in silver staining of gold nanostructures by Raman scattering., Nanoscale. 8 (2016) 9583–9591. doi:10.1039/c6nr01208f.

[40] M. Hema, S. Selvasekarapandian, G. Hirankumar, A. Sakunthala, D.

Arunkumar, H. Nithya, Laser Raman and ac impedance spectroscopic studies of PVA: NH4NO3 polymer electrolyte, Spectrochim. Acta - Part A Mol. Biomol. Spectrosc. 75 (2010) 474–478. doi:10.1016/j.saa.2009.11.012.

[41] D MartinVosshage , B V R Chowdari, SOLID STATE Characterization of poly (ethylene oxide) with cobaltbromide, 62 (1993) 205–216.

[42] L.Z. Fan, Z.M. Dang, C.W. Nan, M. Li, Thermal, electrical and mechanical properties of plasticized polymer electrolytes based on PEO/P(VDF-HFP) blends, Electrochim. Acta. 48 (2002) 205–209. doi:10.1016/S0013-4686(02)00603-5.

[43] P. V. Braun, J. Cho, J.H. Pikul, W.P. King, H. Zhang, High power rechargeable batteries, Curr. Opin. Solid State Mater. Sci. 16 (2012) 186–198. doi:10.1016/j.cossms.2012.05.002.

[44] R. Miao, B. Liu, Z. Zhu, Y. Liu, J. Li, X. Wang, Q. Li, PVDF-HFP-based porous polymer electrolyte membranes for lithium-ion batteries, J. Power Sources. 184 (2008) 420–426. doi:10.1016/j.jpowsour.2008.03.045.

[45] Y. Kumar, S.A. Hashmi, G.P. Pandey, Ionic liquid mediated magnesium ion conduction in poly(ethylene oxide) based polymer electrolyte, Electrochim. Acta. 56 (2011) 3864–3873. doi:10.1016/j.electacta.2011.02.035.

[46] R. Mohtadi, F. Mizuno, Magnesium batteries: Current state of the art, issues and future perspectives, Beilstein J. Nanotechnol. 5 (2014) 1291–1311. doi:10.3762/bjnano.5.143.

[47] J.M. Zen, G. Ilangovan, J.J. Jou, Square-wave voltammetric determination and ac impedance study of dopamine on preanodized perfluorosulfonated ionomer-coated glassy carbon electrodes, Anal. Chem. 71 (1999) 2797–2805. doi:10.1021/ac981009a.

[48] M.S. Michael, M.M.E. Jacob, S.R.S. Prabaharan, S. Radhakrishna, Enhanced lithium ion transport in PEO-based solid polymer electrolytes employing a novel class of plasticizers, Solid State Ionics. 98 (1997) 167–174. http://www.sciencedirect.com/science/article/pii/S0167273897001173 (accessed December 15, 2014).

[49] X. Qian, N. Gu, Z. Cheng, X. Yang, E. Wang, S. Dong, Methods to study the ionic conductivity of polymeric electrolytes using a.c. impedance spectroscopy, J. Solid State Electrochem. 6 (2001) 8–15. doi:10.1007/s100080000190.

[50] C. Vincent, Ion transport in polymer electrolytes, Electrochim. Acta. 40 (1995) 2035–2040. doi:10.1016/0013-4686(95)00138-5.

[51] L.L. Yang, A.R. McGhie, G.C. Farrington, Ionic Conductivity in

Complexes of Poly(ethylene oxide) and MgCl[sub 2], J. Electrochem. Soc. 133 (1986) 1380. doi:10.1149/1.2108891.

[52] A.R. Polu, R. Kumar, H.W. Rhee, Magnesium ion conducting solid polymer blend electrolyte based on biodegradable polymers and application in solid-state batteries, Ionics (Kiel). (2014). doi:10.1007/s11581-014-1174-4.

[53] M. Morita, T. Shirai, N. Yoshimoto, M. Ishikawa, Ionic conductance behavior of polymeric gel electrolyte containing ionic liquid mixed with magnesium salt, J. Power Sources. 139 (2005) 351–355. doi:10.1016/j.jpowsour.2004.07.028.

[54] C.S. Ramya, S. Selvasekarapandian, T. Savitha, G. Hirankumar, P.C. Angelo, Vibrational and impedance spectroscopic study on PVP-NH4SCN based polymer electrolytes, Phys. B Condens. Matter. 393 (2007) 11–17. doi:10.1016/j.physb.2006.11.021.

[55] K. Perera, M.A.K.. Dissanayake, P.W.S.. Bandaranayake, Ionic conductivity of a gel polymer electrolyte based on Mg(ClO4)2 and polyacrylonitrile (PAN), Mater. Res. Bull. 39 (2004) 1745–1751. doi:10.1016/j.materresbull.2004.03.027.

[56] R. Singh, J. Kumar, R.K. Singh, R.C. Rastogi, V. Kumar, Low frequency ac conduction and dielectric relaxation in pristine poly(3-octylthiophene) films, New J. Phys. 9 (2007) 40–40. doi:10.1088/1367-2630/9/2/040.

[57] A.K. Narula, R. Singh, S. Chandra, Low frequency ac conduction and dielectric relaxation in poly (N-methyl pyrrole), Bull. Mater. Sci. 23 (2000) 227–232. http://link.springer.com/article/10.1007/BF02719915 (accessed February 24, 2015).

[58] V. Aravindan, P. Vickraman, A novel gel electrolyte with lithium difluoro(oxalato)borate salt and Sb2O3 nanoparticles for lithium ion batteries, Solid State Sci. 9 (2007) 1069–1073. doi:http://dx.doi.org/10.1016/j.solidstatesciences.2007.07.011.

[59] F. Yakuphanoglu, Y. Aydogdu, U. Schatzschneider, E. Rentschler, DC and AC conductivity and dielectric properties of the metal-radical compound: Aqua[bis(2-dimethylaminomethyl-4-NIT-phenolato)]copper(II), Solid State Commun. 128 (2003) 63–67. doi:10.1016/S0038-1098(03)00651-3.

[60] S.A. Hashmi, S. Chandra, Experimental investigations on a sodium-ion-conducting polymer electrolyte based on poly(ethylene oxide) complexed with NaPF6, Mater. Sci. Eng. B. 34 (1995) 18–26. doi:http://dx.doi.org/10.1016/0921-5107(95)01219-2.

[61] J. Evans, C.A. Vincent, P.G. Bruce, Electrochemical measurement of transference numbers in polymer electrolytes, Polymer (Guildf). 28

(1987) 2324–2328. doi:10.1016/0032-3861(87)90394-6.

[62] D. Aurbach, I. Weissman, Y. Gofer, E. Levi, Nonaqueous magnesium electrochemistry and its application in secondary batteries, Chem. Rec. 3 (2003) 61–73. doi:10.1002/tcr.10051.

[63] N. Amir, Y. Vestfrid, O. Chusid, Y. Gofer, D. Aurbach, Progress in nonaqueous magnesium electrochemistry, J. Power Sources. 174 (2007) 1234–1240. doi:10.1016/j.jpowsour.2007.06.206.

[64] T.E. Sutto, T.T. Duncan, Electrochemical and structural characterization of Mg ion intercalation into RuO2 using an ionic liquid electrolyte, Electrochim. Acta. 79 (2012) 170–174. doi:10.1016/j.electacta.2012.06.099.

[65] D. Aurbach, G.S. Suresh, E. Levi, A. Mitelman, O. Mizrahi, O. Chusid, M. Brunelli, Progress in rechargeable magnesium battery technology, Adv. Mater. 19 (2007) 4260–4267. doi:10.1002/adma.200701495.

CHAPTER 7

Realizing Li Ion Full Cells Using $LiFePO_4$ and Activated Carbon as Electrodes

Abstract:

One of the prime objectives of the present investigations is to practically accomplish the assembling of Li ion full cells using the non-toxic material $LiFePO_4$ *as the cathode active material and the steam activated, coconut shell derived carbon as the anode. The present chapter gives an account of the attempts carried out to assemble the* $LiFePO_4$ *based Li ion full cells and assess their electrochemical performance efficiency.*

7. 1 Introduction

Lithium ion cells are presently struggling to meet the demanding standards in terms of cost, charge/discharge rate, power and energy densities, and safety in order to enter the new emerging markets of electric vehicles and the storage systems of renewable electrical energy [1]. Electrochemical cells exhibit relatively high energy densities as a result of the faradic reactions in the bulk of the active particles, but the rate capabilities are limited. An example of a well-known material that undergoes a redox reaction during the charging and the discharging processes is the lithium iron phosphate ($LiFePO_4$) [2]. After two decades of the seminal work by Goodenough and co workers, $LiFePO_4$ has been established as one of the most promising positive electrode materials for Li ion cells because of its low cost, safety, low toxicity, structural stability and excellent electrochemical properties [3–5]. This material can be reversibly charged and discharged at a stable voltage of 3.2 V vs Li+/Li, with negligible changes in the unit cell parameters during the $LiFePO_4$ to $FePO_4$ phase transition[6,7].

For the development of high power batteries based on this material, it is essential to understand and overcome the challenges related to the lithium transport through the electrodes [8]. In spite of its relatively high theoretical specific capacity around 170 mAh g^{-1} and long cycling life,the high-rate performance of pure $LiFePO_4$ is restricted by its poor electrical conductivity,which is around 10^{-9} S cm^{-1}, and slow lithium diffusion[9] . Large and inhomogeneous particle size distribution of $LiFePO_4$ can lead to a decrease in its lithium ion diffusion coefficient which further reduces the rate capability [10]. In order to achieve good rate capability and excellent electrochemical cycling behavior, it is very important to synthesize $LiFePO_4$ with small grain size, preferably in the nano range, and high electrical conductivity[11]. Many different approaches involving surface coating have been tried to improve the capacity and rate performance of $LiFePO_4$ as the cathode active material for Li ion cells. Increasing the electrical conductivity by coating the $LiFePO_4$ surface with conducting carbon or conducting polymers is one of the most popular methods. In this context, multiwalled carbon nanutubes (MWCNTs) are highly preferred for surface coating and they offer improved interfacial contact, owing to their quite high electronic conductivity, flexible nature, nanoscale dimensions and high surface area [12,13].

Currently, the most commonly used anode material in commercial Li-ion cells is graphite.Its lower theoretical capacity around 372 mAh g^{-1} is not sufficient for developing high energy density,rechargeable batteries to meet the ever increasing energy demands, especially of the automobile sector[14]. Intensive research efforts are being carried out to identify alternative anode materials. Silicon, SnO_2 [15], and the transition metal oxides [16], including CuO[17] and Fe_2O_3 [18] have been extensively investigated to assess their suitability as the anodes. Although there have been improvements in the electrochemical performance, large volumetric expansion and the poor electrical conductivity are the major challenges that need to be addressed in these materials, as a result of which, there is a surplus of issues related to poor cycle performance, lack of the required connectivity with the current collectors and poor columbic efficiency [19] in the first cycle. These drawbacks emphasize the need for developing novel types of carbon based anodes, for the Li ion cells, with the anticitated material qualities for ensuring excellent electrochemical behaviour.

Carbon is used extensively as the electrode material in the Electrochemical Double Layer Capacitors (EDLCs). With the recent development of the Li-ion capacitors (LICs) [14], which combine the advantages of both of the Li ion cells and the EDLCs, carbon, especially the activated carbon (AC) is gaining popularity as the LIC electrode, as well. The activated carbon can be mixed with the cathode material $LiMn_2O_4$ [20], or the anode material $Li_4Ti_5O_{12}$ [21]to act as the cathode or the anode, in Li-ion capacitors. Since the capacitance has a direct link with the surface area, porous activated carbon with high surface area can be employed as the LIC electrodes.There are not sufficient reports on the design and working of the Li ion cells,using activated carbon as the anode material. It will be quite advantageous to explore the application prospects of the activated carbon materials,derived specifically from natural raw materials as the anodes for high energy density Li ion cells.

The meritorious qualities of the hydrofluoric acid (HF) washed,steam activated carbon,derived from the natural product,coconut shell, for applications as the electrode material in high power supercapacitors form the focal theme of the third chapter. The laudable electrochemical behaviour of this HF washed, steam activated carbon sample,(AC) has been established,based on the CV,GCD and the EIS studies,as illustrated in the third chapter.The present work is hence directed towards developing Li ion full cells,using $LiFePO_4$/MWCNTs composite as the cathode material and the AC as the anode material with standard liquid electrolyte. The nano-structured $LiFePO_4$ with high electical conductivity, in bulk form is synthesised by sol-gel technique [22] and the HF washed,steam activated,coconut shell derived carbon,AC is synthesized,as described in chapter 3.

7. 2 Experimental details

7.2.1 Materials and methods

The starting materials**,** ferrous oxalate dihydrate, lithium nitrate, ammonium dihydrogen phosphate,citric acid and nitric acid, all of AR grade, were purchased from Alpha Chemicals,India.The MWCNTs were obtained from Grapheme Supermarket,USA.The synthesis of $LiFePO_4$ was carried out as follows. Stoichiometric amounts of ferrous oxalate dihydrate and lithium nitrate were dissolved in 1 M nitric acid solution into which 20 ml citric acid solution was added drop wise with continuous stirring. To this solution, a saturated solution of ammonium dihydrogen phosphate was added. The mixture was then heated gently at 50 °C with continuous stirring for 4 hours to remove the excess water. The resulting gel precursor was dried in a circulation oven for a week at 80 °C and then fired at 700 °C in a tubular furnace under 99.99 % flowing argon for 2 hours to get $LiFePO_4$ powder. In the above experiment, the molarity of the citric acid solution was fixed at 1 M to achieve particle size in the range 20-40 nm.

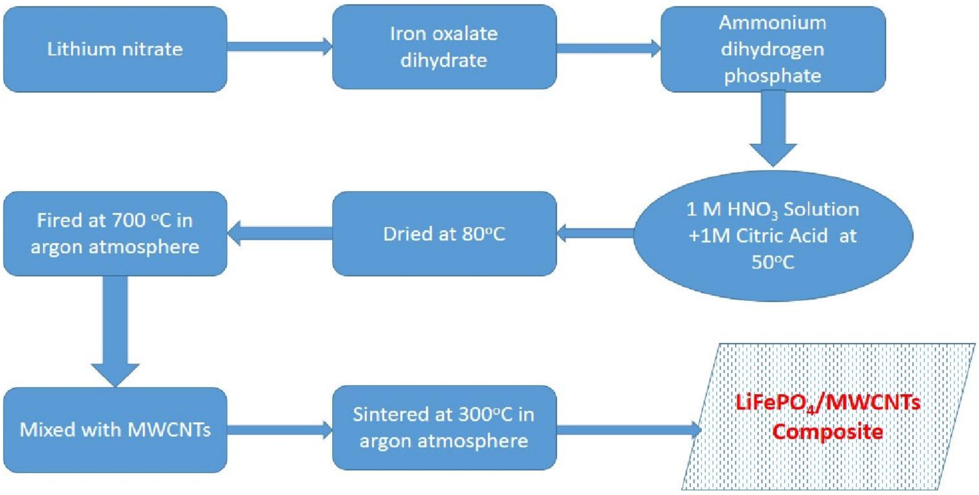

Figure 1 : The schematic representation of the synthesis of LiFePO4 / MWCNTs composite

In this sol-gel technique, the citric acid serves as the complexing /chelating agent that facilitates the mixing of cations at the molecular level. The citric acid also functions as a carbon source which prevents the oxidation of ferrous ions to the ferric state and provides the network structure of carbon for electron conduction. The $LiFePO_4$-MWCNTs (LFP-CNT) composite samples were obtained by mixing the synthesized $LiFePO_4$ powder with 10 weight % of MWCNTs and sintering the mixed powder in the form of pressed pellets at 300 °C for 3 hours under flowing argon. The schematic representation of the synthesis procedure of the LFP-CNT is shown in figure 1. The coconut shell derived, steam activated ,HFwashed, granular carbon, AC with high specific surface area,to be used as the anode, was synthesized,as explained in chapter 3.

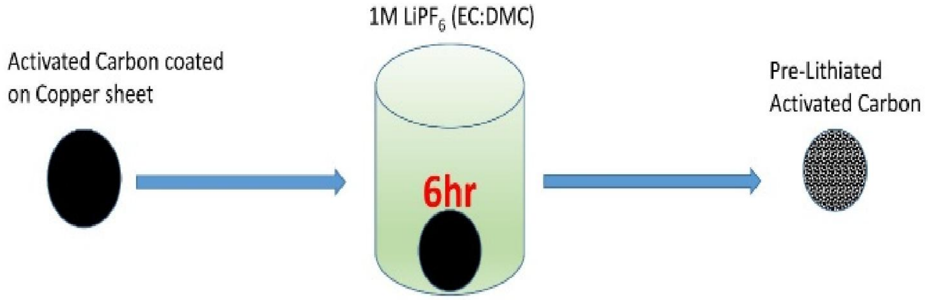

Figure 2: Schematic representation of the pre-lithiation of the AC electrode

In order to investigate the structural aspects of these samples, XRD patterns were recorded using PANAlytical X'Pert PRO with Cu-K_α radiation of wavelength 1.54 Å.The FESEM images were collected using Carl-Zeiss sigma electron microscope. The composite cathode, LFP-CNT, electrodes were prepared by mixing 80 wt% of the active material LFP-CNT,10 wt % of conducting carbon and 10 wt% of poly(vinylidene difluoride) (PVDF), in the presence of N-methyl pyrrolidinone (NMP), to make a slurry. It was pasted on aluminum sheet and heated at 120 ºC under vacuum overnight. In this case, the carbon content of 10% includes both the MWNTs and the conducting diluents. The anode electrodes were prepared by mixing 80 wt% of the active material AC4, 10 wt% of conducting carbon and 10 wt% of poly(vinylidene difluoride) (PVDF), in the presence of N-methyl pyrrolidinone (NMP), to make a slurry. It was pasted on copper foil and dried at 80 ºC under vacuum overnight.

The electrochemical behaviour of the LFP-CNT and the AC samples was investigated by assembling prototype lithium half cells with pure lithium metal as the counter electrode and the above materials as the working electrodes. The electrolyte used was the 1 M solution of $LiPF_6$ in a 1:1 mixture of ethylene carbonate (EC) and dimethyl carbonate (DMC). For full cell assembling, the AC sample was subjected to pre-lithiation process [24] as shown in figure 2. The pre-lithiation of the AC samples was carried out by dipping circular discs of the AC4 electrode in the $LiPF_6$ based electrolyte,mentioned above, for 6 hours inside the argon filled glove box, in which, the oxygen and the moisture levels are controlled to be < 1 ppm. After the pre-lithiation process,the AC sample was immediately transformed to the coil cell case as the anode,in which the LFP-CNT electrode disc was already loaded as the cathode. The pre-lithiation and the half cell and the full cell assembling were done in the argon filled glove box. The assembled cells were subjected to cyclic voltammetry and charge-discharge stu using the Bio-Logic SP300 Unit.

7. 3 Results and discussion

7.3.1 The XRD analysis

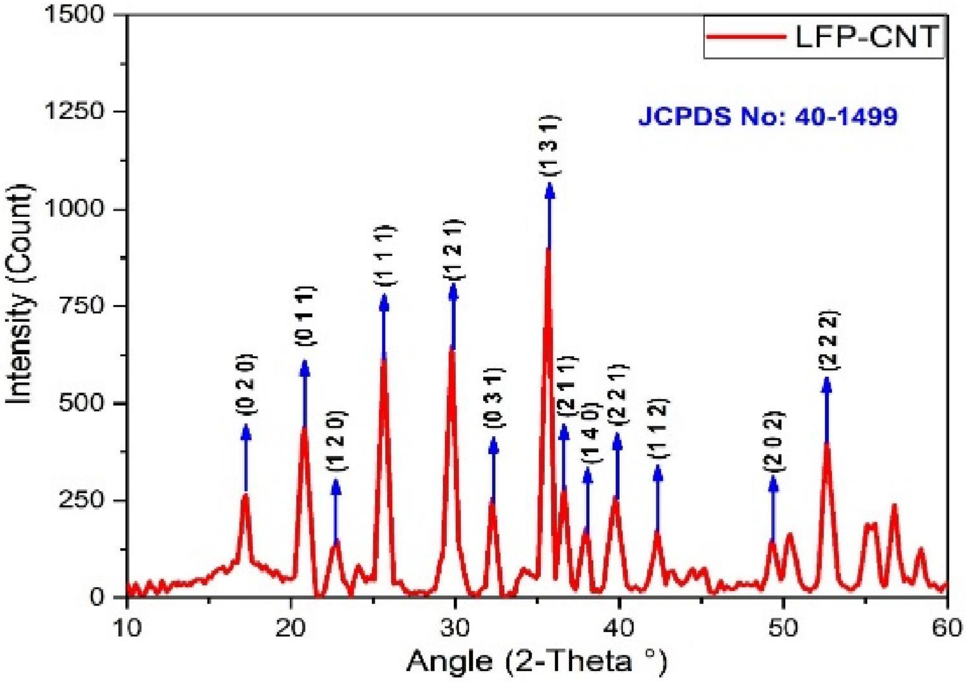

Figure 3A : The XRD pattern of the LFP-CNT composite

The XRD patterns of the LFP-CNT and the AC composite samples are shown in Figures 3A and 3B respectively. The pattern shows all the characteristic peaks of $LiFePO_4$. The absence of any extra peaks confirms the phase purity of the $LiFePO_4$, obtained by the sol-gel synthesis route adopted in the present work.. The peaks can be perfectly indexed to the ordered orthorhombic olivine crystal structure (JCPDS 40-1499, space group Pnma) [25]. There are no diffraction peaks for the MWCNTs, due to the low content or the low crystallinity of the MWCNTs in the LFP-CNT composite, indicating that the addition of the MWCNTs does not have any effect on the crystal structure of the LFP. The X-ray diffraction peaks of the LFP-CNT are broad, suggesing that the LFP-CNT sample is of smaller crystallite size.

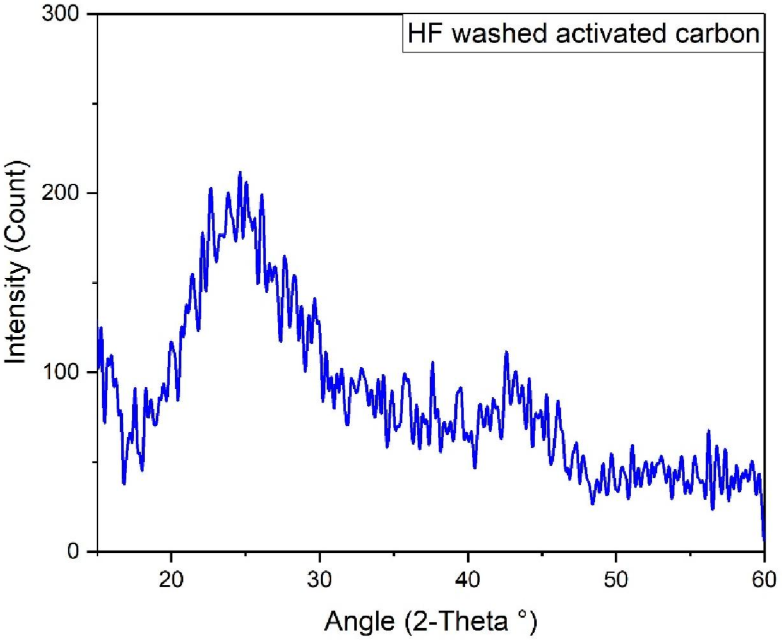

Figure 3B : The XRD pattern of the HF washed activated carbon

The XRD pattern from 2θ= 15 to 60° of the HF washed, activated carbon sample,AC,is shown in figure 3B. The AC sample shows a broad diffraction peak between 20 to 30 °. The absence of sharp peaks in the XRD pattern suggests that the phase present in the AC sample is largely amorphous [26]. A broad peak of the (002) reflection exists between 20° and 30°,centered at ~23°, which is contributed by the disordered carbon [27].

7.3.2 The FESEM analysis

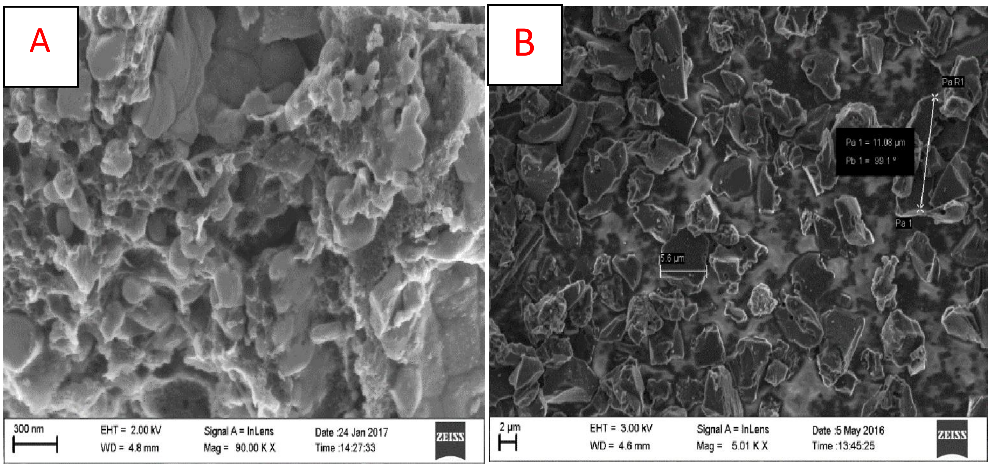

Figure 4: The FESEM micrographs of (A) the LFP-CNT composite (B) the AC sample

The FESEM micrographs of the LFP-CNT composite and the AC sample are shown in Figures 4A and 4B respectively. The $LiFePO_4$ sample has a small average particle size, less than 100 nm. The MWCNTs can also be seen in the FESEM image. These MWCNTs form a homogenous mixture with the nanostructured $LiFePO_4$. The presence of the MWCNTs significantly enhances the electrical conductivity of the $LiFePO_4$. The LFP-CNT composite contains well-crystallized and densely aggregated nanoparticles with interconnected nano-channels, which give rise to a high tap density. The MWCNTs and the citric acid are responsible for the formation of the nano-sized morphology of the $LiFePO_4$ during the synthesis process. It is found that the citric acid helps to decrease the packing density of the sample and regulate and control the homogenous distribution of the $LiFePO_4$.The MWCNTs can be observed on the $LiFePO_4$ particles clearly and the interlaced particles together form a carbon nano-network which leads to electronic continuity between particles. These interconnected nanochannels allow the liquid electrolyte to penetrate in all directions [28].

The FESEM image of the HF washed, steam activated coconut shell derived, carbon sample AC, shown in figure 4B, clearly shows its porous structure with an average particle size around 6 µm. As seen from the micrograph, pores are formed,possibly due to the release of some volatile materials and the activating agent from the sample. The external surface of the AC sample is full of cavities which are due to the removal of impurities upon washing with the hydrofluoric acid. The HF washing provides a larger surface area which helps in the rapid access of the electrolyte into the bulk of the electrode material and enhances the utilization ratio of the active material.. The FESEM image also reveals that AC has a high specific surface area and a shorter diffusion path, which provides the structural foundation for a high specific capacity [29].

7.3.3 Cyclic voltammetry studies

The cyclic voltammetric curves of the LFP-CNT and the AC samples based half-cells with lithium chip as the counter electrode at a scan rate of 0.1 mV/s are shown in figure 5. The CV curve of the LFP-CNT based half-cell, scanned between the electrochemical window of 2.5 V to 4.5 V is shown in figure 5A. During the anodic sweep,the lithium ions are extracted from the $LiFePO_4$

structure. The oxidation peak is located at ~ 3.65V versus Li/Li+. During the scan from 4.5 to 2.5V, the reduction peak is observed at ~3.2V, corresponding to lithium insertion, back into the $LiFePO_4$ structure. The well-defined peaks indicate the higher electrochemical reactivity of the LFP-CNT composite and the related reflection of small polarization, high Li-ion diffusion rate and low inner resistance.The lithium-ion intercalation/deintercalation reactions, accompanied by electron removal, essentially depend on the electronic conducting nature of the electrode material. The addition of the MWCNTs significantly improves the electrical conductivity of the LFP-CNT composite and leads to the active redox reactions. The lithium ions and the electrons are quite active in the redox reactions as a consequence of the formation of the uniformly distributed and nanosized $LiFePO_4$ particles.The diffusion length of the lithium ions in $LiFePO_4$ gets considerably reduced which helps to facilitate reversible electrochemical reactions during the extraction and insertion of the lithium ions [9].

The cyclic voltammogram of the AC sample based lithium half-cell, scanned between 0-3 V is shown in Figure 5(B). During the cathodic and anodic scans, no peaks are observed versus Li/Li+, which can be attributed to the absence of the intercalation of lithium ions into the carbon structure. The absence of the oxidation and reduction peaks indicates that the lithium ion are adsorbed on the surfaces of the activated carbon. . In general, the cathodic and anodic scans remain almost unchanged, confirming good reversibility and cycling stability of the electrochemical process.

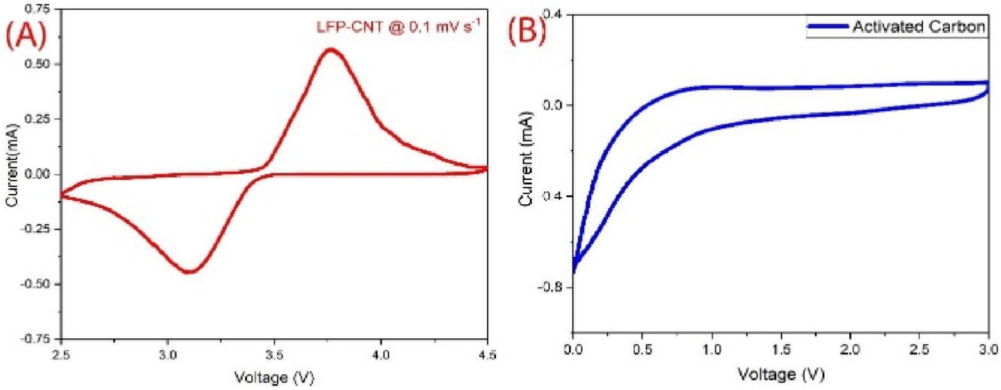

Figure 5: The cyclic voltammetric curves of (A) the LFP-CNT composite and (B) the AC samples based half cells, scanned at 0.1 mV S^{-1}.

7.3.4 Galvanostatic charge discharge studies

The initial charge discharge curves of the LFP-CNT sample based half cell, at different current rates are shown in figure 6A. The voltage plateaus at the range of 3.3V-3.5 V which corresponds to the Fe^{3+}/Fe^{2+} redox couple due to Li extraction, indicate the lithium extraction reactions of $LiFePO_4$ particles from the composite. It is observed that the voltage plateau is flattened for the LFP-CNT composite material, which can be attributed to the higher electrochemical reactivity of the modified $LiFePO_4$ and its excellent kinetics. This result is in accordance with the CV profiles. This composite exhibits higher capacities of 158 mAh g^{-1}, 152 mAh g^{-1} and 126 mAh g^{-1} at C/2 , C and 2C rates respectively .The gap between the charge and the discharge voltage plateau is very small. The high-discharge capacity of the composite is presumed to be associated with the fast reaction and ionic diffusion kinetics of the nanosized particles and good electronic contact facilated by the surface carbon coating.

The initial Charge/discharge curves of the AC sample based half cell at different current densities are shown in figure 6B . The charge / discharge experiment of the cells was performed between 0.2 -3 V at lower rates of 0.1 A g^{-1} and 0.2 A g^{-1} to minimize the SEI layer formation. For higher rates the cycling was performed between 0 to 3V. No plateau is observed for in any current density is due to the adsorption of the lithium ion on the surfaces of activated carbon , which agrees with the CV result. The first discharge and charge specific capacities are 678 mAh g^{-1} and 662 mAh g^{-1} respectively for 0.1A g^{-1} which leads to a small irreversible capacity, because the lower potential is 0.2 V. The specific capacities of the first discharge cycle are 532 mAh g^{-1} and 461 mAh g^{-1} for current densities of 0.5 A g^{-1} and 1 A g^{-1} respectively.

Some researchers have demonstrated that the ability of lithium intercalation and deintercalation in non-graphitic carbonaceous materials depends on their crystalline phase, micro structure and micromorphology. In the present work , using the activated carbon sample the reversible capacity is lower. This is because of its larger surface area which facilitates interfacial/surface Li ion storage. The lithium ion storage in defective locations such as cavities and nanopores could be another reason for the higher capacity of the AC sample.

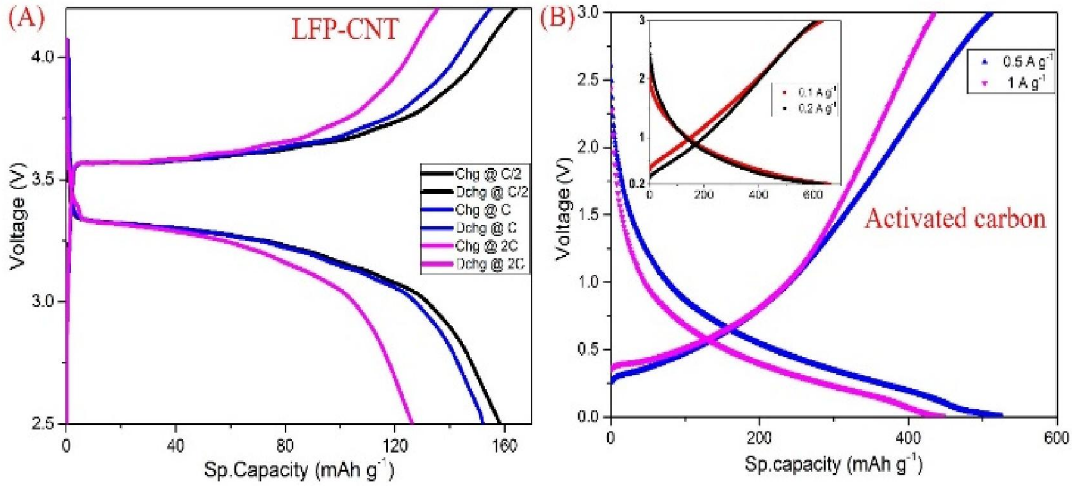

Figure 6: The GCD curves of (A) the LFP-CNT and (B) the AC samples based half cells at different current rates

Comparison of the rate performance of the LFP-CNT composite based cell is shown in figure 7A. After the cells were cycled for 10 cycles at a rate of C/2, the current densities were increased stepwise to 1 C for the next 10 cycles and again the current density was hiked to higher rate at 2 C for the next 30 cycles. The cell exhibits improved electrochemical performance because of the enhanced electrical conductivity due to the presence of the MWCNTs. The capacity of the cell decreases much more slowly with the increasing discharge rate. The cycling performance is comparable to those of the previous reports on $LiFePO_4$/C composites [30,10,31]. The excellent rate performance and the cycling stability of the LFP-CNT composite based cell can be attributed to the presence of the nanosized particles with high surface area and improved electrical conductivity through the MWCNTs.

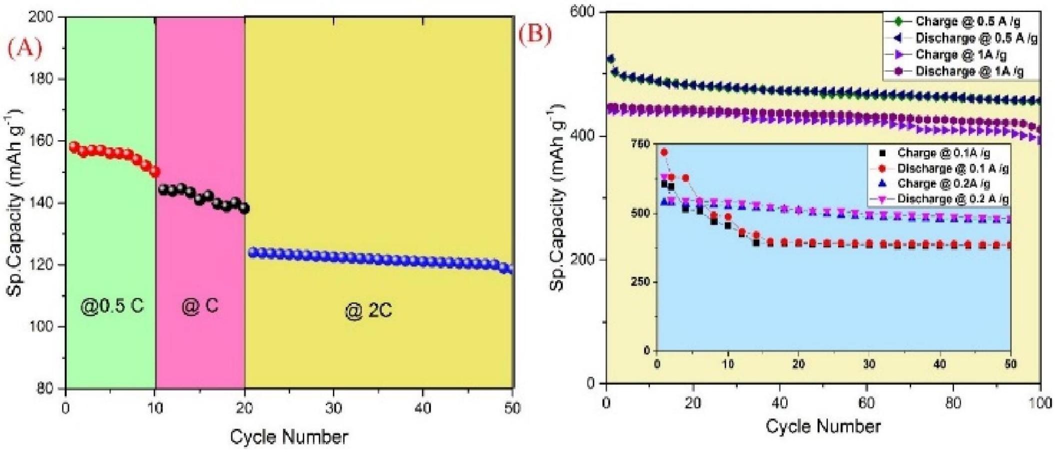

Figure 7: The Rate capability curves of (A)the LFP-CNT and (B) the AC samples based half cells at different current rates

The rate performance of the HF washed activated carbon electrodes based half cell at different current densities for 100 cycles is shown in figure 7B . At a current density of 100 mA g^{-1}, the specific capacity decreases from 749 mAh g^{-1} to 439 mAh g^{-1} at the end of 100 cycles. For a current density of 1000 mA g^{-1}, the decrease is from 445 mAh g^{-1} to 412 mAh g^{-1}. The specific capacity of the AC electrode based cell decreases much slower when tested at 1000 mA g^{-1}. This is because of the large surface area and the porous structure of the AC, which shorten the diffusion path, making diffusion more facile [32].

7.3.5 Full cell characterization

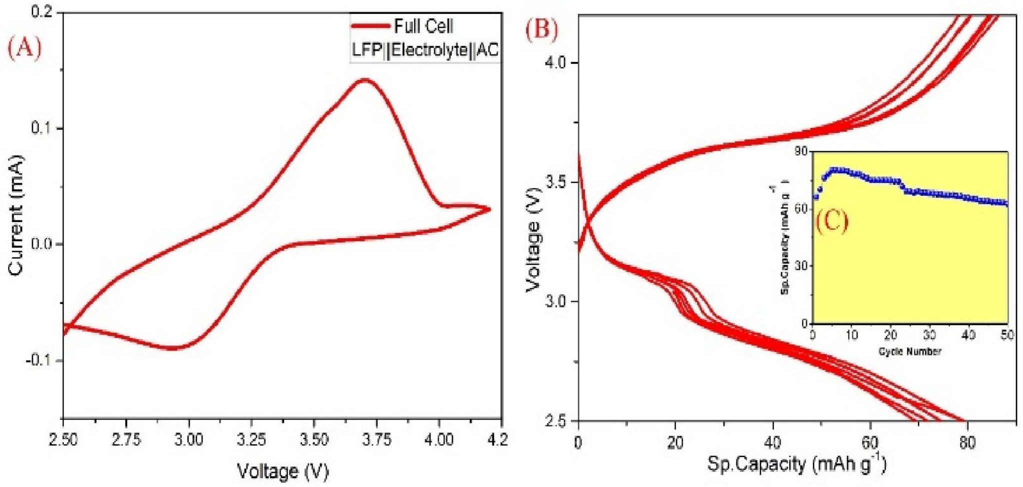

Figure 8 : (A) The Cyclic voltammetric (B) The Charge- discharge and (C)The Cycle life curves of full cell assembled using LFP-CNT as the cathode and pre-lithiated AC as the anode

In designing the full lithium ion cell , it is very important to obatin an optimal balance of the cathode and the anode [33] both in terms of mass and electrochemical activities, as mentioned in the experimental section. The CV curve of the full cell with LFP-CNT as the cathode and AC as the anode is as shown in figure 8(A). It shows a behaviour similar to that of the $LiFePO_4$ based half cell , corresponding to $LiFePO_4$ reduction at ~3.0 V and oxidation at ~3.75 V. The charge-discharge profile of the full cell cycled between 2.5 V to 4.2 V at a rate of 100 mA g^{-1} is shown in figure 8B

The full cell shows a discharge capacity of 80 mAh g^{-1}. The cycling performance of the full device over 50 cycles at a rate of 100 mA g^{-1} is shown in figure 8(C). It is remarkable that one can cycle this device at C/3 rate to obtain the maximum capacity in terms of $LiFePO_4$, taking the therotical capacity as 150 mAh g^{-1} [4]. This is an indication of a faster charge / discharge process for the full cell and the consequent possibility of the performance improvement. Finally, the cycling performance of the full cell shows the stability of the device, over 50 cycles. However, there is a small decay in the capacity of the device. To the best of our knowledge, the lithium storage performance of the LFP-CNT // AC based full cell is much better than most of the reported results[34,35].

7.4 Conclusion

A scalable sol–gel process has been successfully demonstrated for the synthesis of the nano sized $LiFePO_4$ in which MWCNTs are ideally dispersed to make efficient electricaly conducting networks in the composite. A small amount of the MWCNTs (~10 wt%) is quite effective in achieving stable electrochemical performance of the composite. The present work demonstrate for the first time the possible application of the HF washed steam activated coconut shell derived carbon as a prospective negative electrode in lithium ion based energy storage devices. The performance of the full cell has been demonstrated in terms of specific capacity of $LiFePO_4$ .The full cell are found to have good cycling stability over 50 charge discharge cycles. These full cell offers ample application prospects for designing the next generation , the high energy density battery systems.

7.5 References

[1] J. Hassoun, K.-S. Lee, Y.-K. Sun, B. Scrosati, An Advanced Lithium Ion Battery Based on High Performance Electrode Materials, J. Am. Chem. Soc. 133 (2011) 3139–3143. doi:10.1021/ja110522x.

[2] Y. An, H. Fei, J. Feng, L. Ci, S. Xiong, A novel Lithium / Sodium hybrid aqueous electrolyte for hybrid supercapacitors based on LiFePO 4 and activated carbon, Funct. Mater. Lett. 9 (2016) 16–18. doi:10.1142/S179360471642008X.

[3] J. Suk, Y.H. Lee, D.Y. Kim, D.W. Kim, S.Y. Cho, J.M. Kim, Y. Kang, Semi-interpenetrating solid polymer electrolyte based on thiol-ene cross-linker for all-solid-state lithium batteries, J. Power Sources. 334 (2016) 154–161. doi:10.1016/j.jpowsour.2016.10.008.

[4] J. Lang, B. Ding, T. Zhu, H. Su, H. Luo, L. Qi, K. Liu, K. Wang, N. Hussain, C. Zhao, X. Li, H. Gao, H. Wu, Cycling of a Lithium-Ion Battery with a Silicon Anode Drives Large Mechanical Actuation, Adv. Mater. (2016) 1–8. doi:10.1002/adma.201603061.

[5] H.C. Shin, W. Il Cho, H. Jang, Electrochemical properties of carbon-

coated LiFePO4 cathode using graphite, carbon black, and acetylene black, Electrochim. Acta. 52 (2006) 1472–1476. doi:10.1016/j.electacta.2006.01.078.

[6] L. Yao, Facile Synthesis of LiFePO4/C with High Tap-density as Cathode for High Performance Lithium Ion Batteries, Int. J. Electrochem. Sci. 12 (2017) 206–217. doi:10.20964/2017.01.32.

[7] J.L. Dodd, R. Yazami, B. Fultz, Phase Diagram of Li[sub x]FePO[sub 4], Electrochem. Solid-State Lett. 9 (2006) A151. doi:10.1149/1.2164548.

[8] J. Molenda, A. Kulka, A. Milewska, W. Zając, K. Świerczek, Structural, Transport and Electrochemical Properties of LiFePO4 Substituted in Lithium and Iron Sublattices (Al, Zr, W, Mn, Co and Ni), Materials (Basel). 6 (2013) 1656–1687. doi:10.3390/ma6051656.

[9] H. Liu, C. Li, H.P. Zhang, L.J. Fu, Y.P. Wu, H.Q. Wu, Kinetic study on LiFePO4/C nanocomposites synthesized by solid state technique, J. Power Sources. 159 (2006) 717–720. doi:http://dx.doi.org/10.1016/j.jpowsour.2005.10.098.

[10] Y. Shi, S.-L. Chou, J.-Z. Wang, D. Wexler, H.-J. Li, H.-K. Liu, Y. Wu, Graphene wrapped LiFePO4/C composites as cathode materials for Li-ion batteries with enhanced rate capability, J. Mater. Chem. 22 (2012) 16465. doi:10.1039/c2jm32649c.

[11] Y.N. Ko, S. Bin Park, S.H. Choi, Y.C. Kang, One-pot synthesis of manganese oxide-carbon composite microspheres with three dimensional channels for Li-ion batteries, Sci. Rep. 4 (2014) 5751. doi:10.1038/srep05751.

[12] S.-C. Her, C.-Y. Lai, Dynamic Behavior of Nanocomposites Reinforced with Multi-Walled Carbon Nanotubes (MWCNTs), Materials (Basel). 6 (2013) 2274–2284. doi:10.3390/ma6062274.

[13] Yi Youngmi, Study on the degradation of carbon materials for electrocatalytic applications, Genehm. Diss. D (2014).

[14] D. Zhao, Y. Wang, Y. Zhang, High-Performance Li-ion Batteries and Super- capacitors Based on Prospective Nanomaterials, Nano-Micro Lett. 3 (2011) 62–71. doi:10.5101/nml.v3i1.p62-71.

[15] J. Hassoun, G. Derrien, S. Panero, B. Scrosati, A nanostructured Sn-C composite lithium battery electrode with unique stability and high electrochemical performance, Adv. Mater. 20 (2008) 3169–3175. doi:10.1002/adma.200702928.

[16] W.. Li, Y.. Bu, H.. Jin, J.. Wang, W.. Zhang, S.. Wang, J.. Wang, The preparation of hierarchical flowerlike NiO/reduced graphene oxide composites for high performance supercapacitor applications, Energy and Fuels. 27 (2013) 6304–6310. doi:10.1021/ef401190b.

[17] L.-F. Jiao, H.-T. Yuan, Y.-C. Si, Y.-J. Wang, Y.-M. Wang, Synthesis of Cu0.1-doped vanadium oxide nanotubes and their application as cathode materials for rechargeable magnesium batteries, Electrochem. Commun. 8 (2006) 1041–1044. doi:10.1016/j.elecom.2006.03.043.

[18] R. Verrelli, R. Brescia, A. Scarpellini, L. Manna, B. Scrosati, J. Hassoun, A lithium ion battery exploiting a composite Fe2O3 anode and a high voltage Li1.35Ni0.48Fe0.1Mn1.72O4 cathode, RSC Adv. 4 (2014) 61855–61862. doi:10.1039/C4RA12598C.

[19] A. Mirhoseini, F. Koushanfar, HypoEnergy. Hybrid supercapacitor-battery power-supply optimization for Energy efficiency, 2011 Des. Autom. Test Eur. (2011) 1–4. doi:10.1109/DATE.2011.5763298.

[20] H. Xu, B. Cheng, Y. Wang, L. Zheng, X. Duan, L. Wang, J. Yang, Y. Qian, Improved Electrochemical Performance of LiMn2O4/Graphene Composite as Cathode Material for Lithium Ion Battery, Int. J. Electrochem. Sci. 7 (2012) 10627–10632. http://electrochemsci.org/papers/vol7/71110627.pdf (accessed November 12, 2014).

[21] N. Wu, Y. Lyu, R. Xiao, X. Yu, Y. Yin, X. Yang, H. Li, L. Gu, Y. Guo, A highly reversible , low-strain Mg-ion insertion anode material for rechargeable Mg-ion batteries, NPG Asia Mater. 6 (2014) 1–7. doi:10.1038/am.2014.61.

[22] K.-F. Hsu, S.-Y. Tsay, B.-J. Hwang, Synthesis and characterization of nano-sized LiFePO4 cathode materials prepared by a citric acid-based sol?gel route, J. Mater. Chem. 14 (2004) 2690. doi:10.1039/b406774f.

[23] Steven H. Vanderpool, Activated carbon catalysts and preparation of linear polyethylene polyamines therewith, US Pat. US4584405 (1983).

[24] J. Zhang, Z. Shi, C. Wang, Effect of pre-lithiation degrees of mesocarbon microbeads anode on the electrochemical performance of lithium-ion capacitors, Electrochim. Acta. 125 (2014) 22–28. doi:10.1016/j.electacta.2014.01.040.

[25] F. Fathollahi, M. Javanbakht, H. Omidvar, M. Ghaemi, Improved electrochemical properties of LiFePO4/graphene cathode nanocomposite prepared by one-step hydrothermal method, J. Alloys Compd. 627 (2015) 146–152. doi:10.1016/j.jallcom.2014.12.025.

[26] K.S. Sulaiman, A. Mat, A.K. Arof, Activated carbon from coconut leaves for electrical double-layer capacitor, Ionics (Kiel). 22 (2016) 911–918. doi:10.1007/s11581-015-1594-9.

[27] L. Ci, B. Wei, C. Xu, J. Liang, D. Wu, S. Xie, W. Zhou, Y. Li, Z. Liu, D. Tang, Crystallization behavior of the amorphous carbon nanotubes prepared by the CVD method, J. Cryst. Growth. 233 (2001) 823–828. doi:10.1016/S0022-0248(01)01606-2.

[28] G. Qin, Q. Wu, J. Zhao, Q. Ma, C. Wang, C/LiFePO4/multi-walled carbon nanotube cathode material with enhanced electrochemical performance for lithium-ion batteries, J. Power Sources. 248 (2014) 588–595. doi:10.1016/j.jpowsour.2013.06.070.

[29] M.R. SATYABRATA SAHOO, Experimental studies on an indigenous coconut shell based activated carbon suitable for natural gas storage, Sadhana. 41 (2016) 459–468. doi:DOI 10.1007/s12046-016-0483-x.

[30] O. Cech, J.E. Thomas, M. Sedlarikova, A. Fedorkova, J. Vondrak, M.S. Moreno, A. Visintin, Performance improvement on LiFePO4/C composite cathode for lithium-ion batteries, Solid State Sci. 20 (2013) 110–114. doi:10.1016/j.solidstatesciences.2013.03.017.

[31] Z. Xu, L. Xu, Q. Lai, X. Ji, Microemulsion synthesis of LiFePO4/C and its electrochemical properties as cathode materials for lithium-ion cells, Mater. Chem. Phys. 105 (2007) 80–85. doi:10.1016/j.matchemphys.2007.04.039.

[32] C. Chen, R. Agrawal, Y. Hao, C. Wang, Activated Carbon Nanofibers as High Capacity Anodes for Lithium-Ion Batteries, ESC Solid State Sci. Technol. 2 (2013) 3074–3077. doi:10.1149/2.011310jss.

[33] W. Wang, J. Qin, Z. Yin, M. Cao, Achieving Fully Reversible Conversion in MoO $_3$ for Lithium Ion Batteries by Rational Introduction of CoMoO $_4$, ACS Nano. (2016) acsnano.6b05150.

doi:10.1021/acsnano.6b05150.

[34] M.J. Loveridge, M.J. Lain, I.D. Johnson, A. Roberts, S.D. Beattie, R. Dashwood, J.A. Darr, R. Bhagat, Towards High Capacity Li-ion Batteries Based on Silicon- Graphene Composite Anodes and Sub-micron V-doped LiFePO 4 Cathodes, Nat. Publ. Gr. (2016). doi:10.1038/srep37787.

[35] Z. Cabán-Huertas, D.P. Dubal, O. Ayyad, P. Gómez-Romero, Capacitive vs Faradaic Energy Storage in a Hybrid Cell with $LiFePO_4$ /RGO Positive Electrode and Nanocarbon Negative Electrode, J. Electrochem. Soc. 164 (2017) A6140–A6146. doi:10.1149/2.0211701jes.

CHAPTER 8

Summary and Scope for Further Studies

Abstract:

The conclusions drawn from the present investigations are summarized in this chapter. The significant outcome of the present study are highlighted and the prospects for further investigations in this direction are also discussed.

8.1 Summary and conclusions

The entire work presented in the thesis can be portrayed as the pursuit to identify the best category of materials for developing energy storage devices with the anticipated electrochemical behavior to meet the commercial standards. Devices for the efficient storage of the generated energy are mandatory for devising sustainable energy systems. The potential of the clean and the pollution free energy, harvested from the sun and the wind can be fully utilized only when efficient storage systems are also developed simultaneously. The energy storage systems mainly include the primary and secondary batteries, the fuel cells and the supercapacitors. In general, these systems for electrochemical energy storage convert chemical energy into electrical energy.

In the modern era, one can justifiably boast of a rich variety of electrochemical storage devices which include the rechargeable cells, supercapacitors and fuel cells, as mentioned before. Many categories of these types of devices are beset with single or multiple drawbacks and deficiencies. The deficiencies are associated with different parameters like shelf life , cycle life , energy power ratio, low conductivity, low rate capability and so on. With the proper rectification of these issues, the electrochemical devices can assume an elated status in the commercial markets and the daily life of the human society. An unprecedented advancement in this direction is envisaged to be achieved through suitable changes in the selection of materials and alterations in the synthesis procedures employed.

The studies on the realization of, steam activated carbon based supercapacitors, exhibiting electrode double layer capacitance, form the focal theme of the first work on supercapacitors described in the thesis. The steam activated, coconut shell derived carbon (CSC) and its three variants are obtained by washing the CSC in different acids. The PIXE analysis is used to verify the purity of the samples. The structural and the surface studies using Raman spectroscopy and the BET surface analysis technique reveal that, the structural features of the activated carbon samples get improved, after washing with the acids. Out of the three acid washing procedures, washing with hydrofluoric acid (HF) is found to yield activated carbon samples with maximum purity, structural order and surface morphology with the optimum ratio of micropores to mesopores, suitable to facilitate fast electrolyte ion diffusion and transport. The supercapacitor test cells, assembled using the HF washed activated carbon as the electrode material, give a capacitance of 162 F g^{-1} and an energy density of 35.2 Wh kg^{-1} at a current density of 1 A g^{-1}, and a power density of 3967 W kg^{-1} at 10 A g^{-1} along with good cycling stability. It is also observed that 95 % of the initial capacitance is retained after 5000 cycles at a current density of 10 A g^{-1}.

The studies carried out on the nanocomposite material of manganese oxide (Mn_3O_4) and reduced graphene oxide (rGO), obtained by the simple, physical mixing of the components, as a prospective electrode for high power supercapacitor applications, constitute the second type of work on supercapacitors. The Mn_3O_4 nanorods of average diameter 36 nm is synthesized via the hydrothermal method and rGO, by the chemical reduction of graphene oxide, obtained by modified Hummer's method. The structural and the morphological studies conducted using the XRD, Raman spectroscopy, the BET surface analysis, the FESEM and the TEM techniques reveal that, in the nanocomposite, the Mn_3O_4 nanorods are dispersed homogenously within the rGO layers, with the structural characteristics of the component materials, kept intact. The nanocomposite electrode with the component materials taken in 1:1 ratio shows excellent , three electrode electrochemical performance in 1 M Na_2SO_4 electrolyte and a specific capacitance of 228 F g^{-1} at a current density of 5 A g^{-1} has been observed for the nanocomposite electrode. The symmetric supercapacitor test cells assembled, using the Mn_3O_4/rGO nanocomposite as the electrode material, give a capacitance of 94 F g^{-1}, an energy density of 82 Wh kg^{-1} at 1 A g^{-1}, a power density of 7097 W kg^{-1} and good cycling stability with 95 % retention of the initial capacitance after 5000 cycles, at 5 A g^{-1}. The above investigations provide conclusive experimental support to identify the steam activated, HF washed, coconut shell derived carbon and the Mn_3O_4/rGO nanocomposite as suitable electrode materials for assembling high power supercapacitors.

The lithium-sulfur (Li-S) cells are considered to be the potential candidates for the development of next generation energy storage devices owing to the impressive electrochemical properties of sulfur electrodes with high theoretical specific capacity of 1675 mAh g^{-1}.The lack of electronic conductivity of sulfur in the required range, the large volume expansion of sulfur during lithium intake and the formation of soluble polysulfides during the cycling process are the main limitations of this technology. To address these challenges, in the present work, the composite of sulfur with the conducting polymer PEDOT: PSS, obtained using the hydrothermal technique, is tested as the electrode material for Li-S cells. The formation of the layered sulfur/PEDOT: PSS nanocomposite, with the polymer coating formed over the sulfur nanoparticles can be established, based on the XRD, Raman spectroscopy, the FESEM and the TEM studies. The electrochemical studies show that the cells assembled using the sulfur /PEDOT: PSS composite as the electrode, with the component materials taken in the weight ratio of 9:1, give an initial discharge capacity of 1301 mAh g^{-1} at 0.1 C rate. The highlight of the present work is the observation of the discharge capacity of 664 mAh g^{-1} at 1 C rate, at the end of the 200th cycle with the capacity retention of 75 % of the stable discharge capacity. For the emerging Li-S technology, the present results are quite promising, and the higher rate capability offered by the sulfur /PEDOT:PSS electrodes, extend superior application prospects in the ongoing developmental research activities of this technology.

The next phase of the research work deals with the studies on the suitability of the solid polymer electrolyte (SPE) , based on the poly(ethylene oxide) (PEO) - poly(vinyl pyrrolidone) (PVP) blend polymer, complexed with

$Mg(NO_3)_2$, for applications in all solid state magnesium ion cells. On solvating the PEO-PVP blend with different concentrations of $Mg(NO_3)_2$ salt, the PEO-PVP-$Mg(NO_3)_2$ complex electrolyte, termed as the solid polymer electrolyte (SPE) is formed. Flexible, free-standing membranes of this SPE of thickness around 100 μm are obtained by solution casting technique. The ionic conductivity evaluated for this SPE membrane is four orders higher than that of pure PEO and close to that of liquid electrolytes used in Mg ion cells. The highest Mg ion conductivity observed for the SPE membrane, in the present work is 5.8×10^{-4} S cm^{-1} at room temperature, which is higher than the previously reported ionic conductivity for Mg salt complexed solid polymer electrolytes. The cyclic voltammetry (CV) curve of the SPE with stainless steel (SS) blocking electrodes shows a wide electrochemical window of 4 V. The Mg ion cells assembled using this SPE as the electrolyte, without the need for any additional separator, show an open circuit voltage around 1.46 V and are electrochemically active.

The olivine-type, $LiFePO_4$ has been recognized as one of the most promising cathode materials for rechargeable Li ion cells. Its advantages include, high theoretical capacity, high stability, nontoxicity, and low cost. However, $LiFePO_4$ has inherently low electrical conductivity which results in its poor rate capability. The large and inhomogeneous particle size distribution in $LiFePO_4$ can lead to a decrease in its lithium ion diffusion coefficient which further reduces the rate capability. To achieve good rate capability and excellent electrochemical cycling behaviour, it is very important to synthesize $LiFePO_4$ samples with particle size preferably in the nano-dimensional range, and high electrical conductivity. The studies carried out to realize lithium ion full cells using nanostructured $LiFePO_4$ as the cathode active material, pre-lithiated, HF washed coconut shell derived, steam activated carbon as the anode material and 1M $LiPF_6$, dissolved in EC: DMC as the electrolyte, constitute the last part of the work included in the thesis. It is observed that, these cells can be charged and discharged at high C rates without much capacity fading, compared to the commercialized cells, assembled using graphite as the anode.

8.2 Future prospects

The inferences drawn from the present studies extend ample scope for further investigations to establish quite promising approaches for accomplishing commercial standards for the different types of the energy storage devices which are presently in the infant states of development. The next phase of activities can be focused on the following aspects.

1. Development of all solid state lithium and magnesium ion cells with high energy density and excellent cycling performance, compatible with commercial standards, using solid polymer electrolytes.
2. Realization of lithium ion capacitors using the activated carbon, derived from coconut shell through steam activation.

3. Explorations on the commercial designs for the proto type lithium and magnesium based cells and the carbon and transition metal oxides based super capacitors developed in the present study.
4. Pursuit of novel types of cathode and anode materials to enhance the specific capacity and the energy density of the Li and the Mg ion cells, compatible with the energy demands of the next generation portable devices and the hybrid electric vehicles.

Appendix A

BET surface area, pore volume and average pore size of the samples

AC Types	**Surface area $m^2\ g^{-1}$**	**Avg. Pore size A°**	**Total Pore volume $cm^3\ g^{-1}$**	**Micropore Area $m^2\ g^{-1}$**	**% micropore Area**
AC1	2077	17.56	0.912	1211	58
AC2	1882	17.54	0.83	1249	66
AC3	1824	17.83	0.813	767	42
AC4	1864	18.75	0.874	690	37

Appendix B

TGA Curves of PS1, PS2, and PS3 Composite samples.

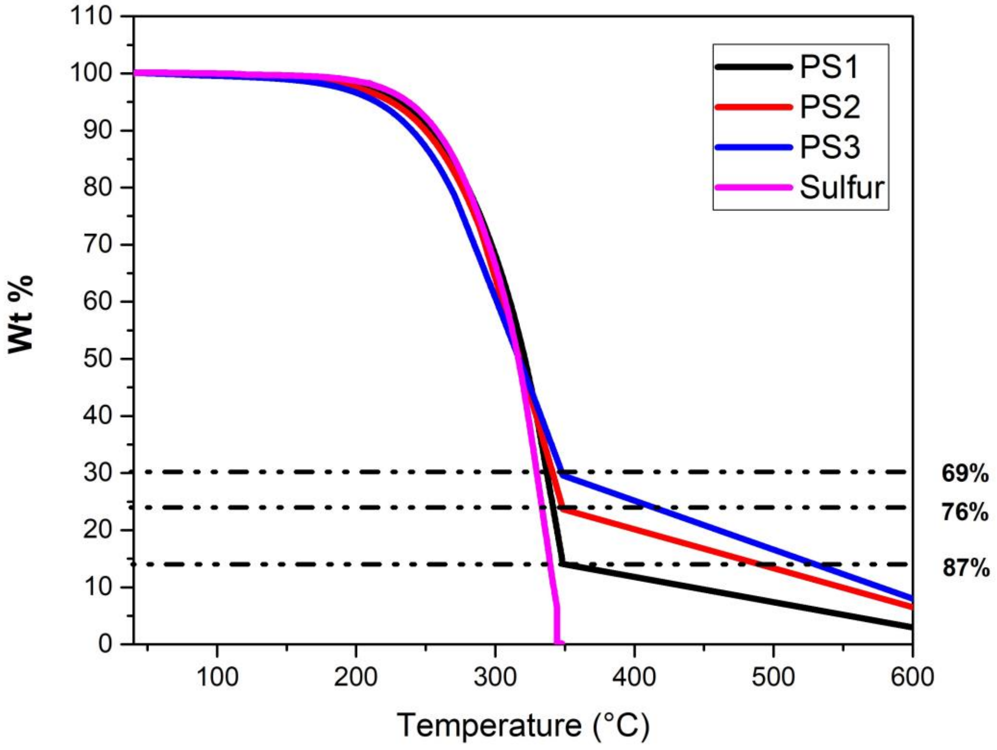

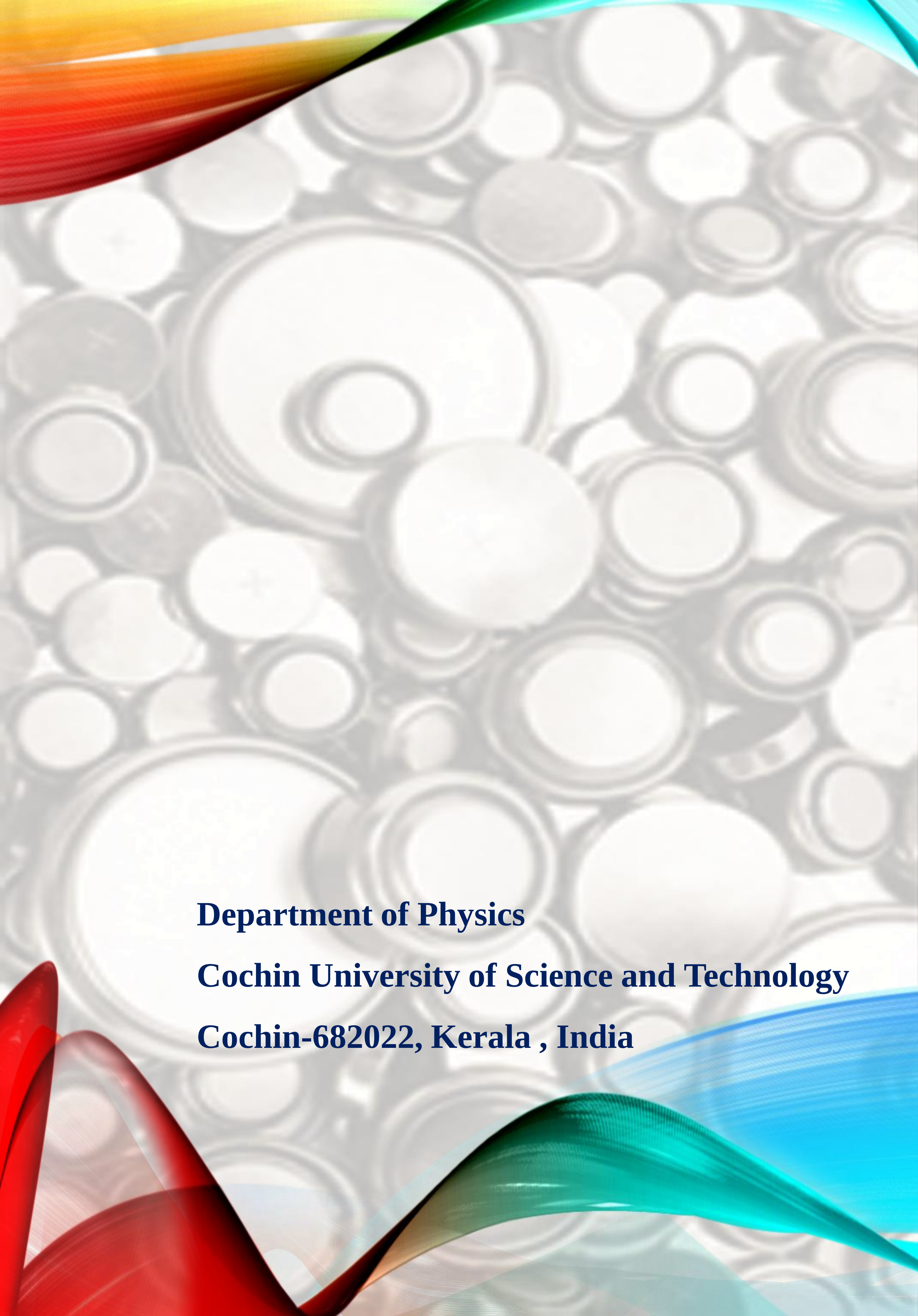

Department of Physics
Cochin University of Science and Technology
Cochin-682022, Kerala , India